

Air Force Institute of Technology

**AFIT Scholar**

---

Theses and Dissertations

Student Graduate Works

---

3-3-2008

## Conceptual Study of Rotary-Wing Microrobotics

Kelson D. Chabak

Follow this and additional works at: <https://scholar.afit.edu/etd>



Part of the [Artificial Intelligence and Robotics Commons](#)

---

### Recommended Citation

Chabak, Kelson D., "Conceptual Study of Rotary-Wing Microrobotics" (2008). *Theses and Dissertations*. 2764.

<https://scholar.afit.edu/etd/2764>

This Thesis is brought to you for free and open access by the Student Graduate Works at AFIT Scholar. It has been accepted for inclusion in Theses and Dissertations by an authorized administrator of AFIT Scholar. For more information, please contact [richard.mansfield@afit.edu](mailto:richard.mansfield@afit.edu).



**CONCEPTUAL STUDY OF ROTARY-WING MICROROBOTICS**

THESIS

Kelson D. Chabak, First Lieutenant, USAF

AFIT/GE/ENG/08-03

**DEPARTMENT OF THE AIR FORCE  
AIR UNIVERSITY**

***AIR FORCE INSTITUTE OF TECHNOLOGY***

---

---

**Wright-Patterson Air Force Base, Ohio**

APPROVED FOR PUBLIC RELEASE; DISTRIBUTION UNLIMITED

The views expressed in this thesis are those of the author and do not reflect the official policy or position of the United States Air Force, Department of Defense, or the U.S. Government.

AFIT/GE/ENG/08-03

**CONCEPTUAL STUDY OF ROTARY-WING MICROROBOTICS**

THESIS

Presented to the Faculty

Department of Electrical and Computer Engineering

Graduate School of Engineering and Management

Air Force Institute of Technology

Air University

Air Education and Training Command

In Partial Fulfillment of the Requirements for the  
Degree of Master of Science in Electrical Engineering

Kelson D. Chabak, BSME

First Lieutenant, USAF

March 2008

APPROVED FOR PUBLIC RELEASE; DISTRIBUTION UNLIMITED




**CONCEPTUAL STUDY OF ROTARY-WING MICROROBOTICS**

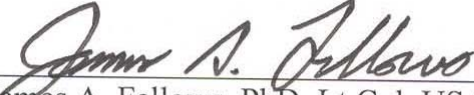
Kelson D. Chabak, BSME

First Lieutenant, USAF

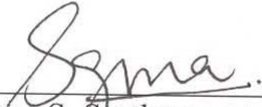
Approved:

  
\_\_\_\_\_  
LaVern A. Starman, PhD, Maj, USAF (Chairman)

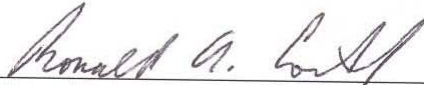
3 Mar 08  
Date

  
\_\_\_\_\_  
James A. Fellows, PhD, Lt Col, USAF (Member)

3 MAR 08  
Date

  
\_\_\_\_\_  
Guna S. Seetharaman, PhD (Member)

3 Mar 08  
Date

  
\_\_\_\_\_  
Ronald A. Coutu Jr., PhD, Maj, USAF (Member)

3 Mar 08  
Date

**Abstract**

This thesis presents a novel rotary-wing micro-electro-mechanical systems (MEMS) robot design. Two MEMS wing designs were designed, fabricated and tested including one that possesses features conducive to insect level aerodynamics. Two methods for fabricating an angled wing were also attempted with photoresist and CrystalBond™ to create an angle of attack. One particular design consisted of the wing designs mounted on a gear which are driven by MEMS actuators. MEMS comb drive actuators were analyzed, simulated and tested as a feasible drive system. The comb drive resonators were also designed orthogonally which successfully rotated a gear without wings. With wings attached to the gear, orthogonal MEMS thermal actuators demonstrated wing rotation with limited success. Multi-disciplinary theoretical expressions were formulated to account for necessary mechanical force, allowable mass for lift, and electrical power requirements. The robot design did not achieve flight, but the small pieces presented in this research with minor modifications are promising for a potential complete robot design under 1 cm<sup>2</sup> wingspan. The complete robot design would work best in a symmetrical quad-rotor configuration for simpler maneuverability and control. The military's method to gather surveillance, reconnaissance and intelligence could be transformed given a MEMS rotary-wing robot's diminutive size and multi-role capabilities.

## **Acknowledgments**

I am in debt to my wife for her resolute support and devotion to my education and career goals. I am thankful for her assiduous lifestyle of working full-time and taking care of all the little things at home. Her personal sacrifices and confidence in me is a constant reminder of her genuine love.

Thanks also to my parents and my mother and father in-laws. The support of my parents is steadfast, and I owe them for their superb guidance throughout my life. I am also grateful to have a great mother and father in-law; I appreciate their countless drives across the Midwest to visit. Special thanks to my father-in-law for his generous time helping me with house projects during this research.

I would like to express my sincere appreciation to my faculty advisor, Maj LaVern Starman, for his guidance and support throughout the course of this thesis effort. The insight and experience was certainly appreciated. I would, also, like to thank my sponsors, Mr. Chris Perry and Mr. Roger Smith, from the Air Force Research Lab for both the support and latitude provided to me in this endeavor.

Kelson D. Chabak

# Table of Contents

	Page
<b>Abstract</b> .....	<b>iv</b>
<b>Acknowledgments</b> .....	<b>v</b>
<b>Table of Contents</b> .....	<b>vi</b>
<b>List of Figures</b> .....	<b>ix</b>
<b>List of Tables</b> .....	<b>xix</b>
<b>List of Acronyms</b> .....	<b>xx</b>
<b>I. Introduction</b> .....	<b>1</b>
1.1 Background.....	2
1.2 Research Objectives .....	3
1.3 Research Focus.....	3
1.4 Methodology.....	3
1.5 Assumptions/Limitations.....	4
1.6 Organization of Thesis .....	4
<b>II. Literature Review</b> .....	<b>5</b>
2.1 Chapter Overview.....	5
2.2 A Brief History of Robots .....	5
2.3 Untethered Land-Based MEMS Robots .....	8
2.4 Miniature Flying Robots.....	10
2.5 Flying MEMS-Based Robots .....	19
2.6 Power MEMS and Photovoltaic Devices .....	27
2.6.1 <i>Power MEMS</i> .....	27
2.6.2 <i>Photovoltaic Devices</i> .....	30
2.7 Chapter Summary .....	33
<b>III. Device Theory</b> .....	<b>34</b>
3.1 Chapter Overview.....	34
3.2 Aerodynamics.....	34
3.2.1 <i>Conventional Aerodynamics</i> .....	34
3.2.2 <i>Low-Reynolds Number Aerodynamics</i> .....	38
3.2.3 <i>Bio-inspired Wing Design</i> .....	43
3.3 PolyMUMPs™ Process.....	45
3.4 Thin-film Residual Stress .....	47
3.5 Drive Actuator .....	52

	Page
3.5.1 <i>Survey of Actuators</i> .....	52
3.5.2 <i>Comb Drive Resonators</i> .....	55
3.6 Statics and Dynamics .....	61
3.7 Electromechanical System Theory .....	63
3.8 Chapter Summary .....	65
<b>IV. Design and Fabrication Methodology</b> .....	<b>67</b>
4.1 Chapter Overview .....	67
4.2 MEMS Surface Micro-Machining Design .....	67
4.2.1 <i>Actuation</i> .....	67
4.2.2 <i>Gear</i> .....	69
4.2.3 <i>Wings</i> .....	70
4.3 Assembling MEMS with Flip Chip Technology .....	76
4.4 Chapter Summary .....	78
<b>V. Modeling and Analysis</b> .....	<b>79</b>
5.1 Chapter Overview .....	79
5.2 Thin-film Residual Stress .....	79
5.2.1 <i>Thin-Film Stress and Deflection</i> .....	79
5.2.2 <i>Wing Deflection</i> .....	81
5.3 Analysis of Drive System .....	84
5.3.1 <i>Analysis of Frequency</i> .....	85
5.3.2 <i>Analysis of Deflection</i> .....	87
5.3.3 <i>Analysis of Actuator Force</i> .....	91
5.4 Aerodynamic Feasibility .....	97
5.5 Power Requirements.....	101
5.6 Chapter Summary .....	103
<b>VI. Experimental Tests and Results</b> .....	<b>104</b>
6.1 Chapter Overview .....	104
6.2 Chip Release .....	104
6.2 Wing Deflection .....	105
6.2.1 <i>Residual Stress Deflection</i> .....	105
6.2.2 <i>Wing Hinge</i> .....	111
6.3 Comb Drive Actuation .....	114
6.3.1 <i>Comb Drive Resonator</i> .....	114
6.3.2 <i>Orthogonal Comb Drives</i> .....	115
6.3.2 <i>Wing Rotation</i> .....	119
6.4 Robot Assembly .....	122
6.5 Chapter Summary .....	123
<b>VII. Conclusions and Recommendations</b> .....	<b>125</b>

	Page
7.1 Chapter Overview.....	125
7.2 Conclusions of Research .....	125
7.3 Significance of Research .....	127
7.4 Recommendations for Future Research.....	128
7.5 Summary.....	130
<b>Appendix A: L-Edit Mask Designs.....</b>	<b>131</b>
<b>Appendix B: Residual Stress Deflection Calculations .....</b>	<b>135</b>
<b>Appendix C: Comb Drive Actuator Calculations .....</b>	<b>137</b>
<b>Appendix D: Photoresist Hinge Mask.....</b>	<b>138</b>
<b>Bibliography .....</b>	<b>139</b>
<b>Vita. ....</b>	<b>147</b>

## List of Figures

	Page
Figure 1: (a) Hollar’s crawling silicon solar-powered robot, (b) Dartmouth’s crawling and steerable polysilicon robot and (c) schematic of Dalhousie University frictional microcrawler.....	9
Figure 2: (a) Lockheed Martin MicroStar with 22 cm wingspan, 110 grams mass and 25 minute continuous runtime. (b) MicroStar’s underwing electronics platform is shown on the right. [24]. .....	10
Figure 3: (a) AeroVironment and CalTech’s Black Widow MAV with 6 inch (15.2 cm) wingspan. Black Widow can fly continuously for 30 min with a 1.8 km range [25, 28], and (b) University of Florida flexible-wing design with a wingspan of 5 in (12.7 cm) and run time of 15 min at 15-25 mph [27]. .....	12
Figure 4: (a) MicroBat ornithopter developed by AeroVironment and Pornsin-Sirarak, <i>et al.</i> The wingspan, mass, and run time are 9 inches, 14 grams and 25 minutes (with two lithium batteries), respectively [15]. (b) The 22:1 gear ratio actuating the wings up to 42 Hz at 1.4 W [29]. .....	13
Figure 5: MEMS fabrication process for wings of MicroBat MAV [29]. .....	14
Figure 6: Initial prototype of Stanford’s Mesicopter designed to hover 30 minutes. The four rotor design is 1.5 cm x 1.5 cm weighing 3g [33]. .....	15
Figure 7: (a) Improved rotor designed with four times more lift than initial prototype, and (b) future 2.5 cm x 2.5 cm prototype employing redesigned rotors [33]. .....	15
Figure 8: (a) Early prototype of the MFI using a stainless steel 4-bar frame, and (b) most recent prototype using a composite carbon frame [34, 37]. .....	16
Figure 9: Three versions of DelFly exist in order of largest to smallest are (a) DelFly I, (b) DelFly II and (c) DelFly Micro [38, 39]. .....	17
Figure 10: MicroGlider which uses tail end control surfaces actuated by piezoelectric actuators. MicroGlider has a 10 cm wingspan and can glide for 10 minutes [40]. .....	18
Figure 11: (a) Simple flapping concept using an elastic film and frame, and (b) flapping concept integrated in a closed-loop system; plane A is actuated in the opposite direction of B and C which actuate the wings [42]. .....	20

Figure 12: MEMS wing fabricated from nickel sandwiched between polyimide layers which is designed to utilize drag forces with a different wing shape on up and down strokes [43].	21
Figure 13: (a) Cross section of layers used to fabricate the MFC wing actuator, and (b) actuation scheme of applied 0 V and 6 V [44].	22
Figure 14: (a) MFC force diagram, (b) close-up of wing geometry and (c) quadrant array which allows the MFC to rotate or fly level [44].	22
Figure 15: (a) Diagram of Miki's micro-rotary wing and (b) the fabricated robot with rotating wings in an alternating magnetic field [49].	24
Figure 16: (a) SEM photographs of various flapping wing MEMS robots and (b) optimal design for achieving MEMS scale flight [20].	25
Figure 17: Vision of a rotary-wing MEMS flying robot as a result of Glauvitz' research. The robot consists of four rotors and several comb drive actuators turning the wings' gears. The open area in the middle could be used for an onboard power source [50].	26
Figure 18: Specific energy of liquid hydrocarbon compared to conventional engine, primary batteries and rechargeable batteries [52].	28
Figure 19: Stanford's "Swiss Roll" burner concept to be used in conjunction with a thermoelectric generator [53].	28
Figure 20: Catalytic process of a PEM and DMFC micro-fuel cell shown above and below the red line, respectively [55].	29
Figure 21: Photovoltaic effect shown in doped silicon material. Photon energies greater than the silicon bandgap are absorbed and generate electron-hole pairs. Lower energies are transparent to silicon.	30
Figure 22: Triple junction GaInP/GaInAs/Ge solar cell. More photons are absorbed using stacked direct bandgap materials with decreasing bandgap energies. Tunnel junctions are implemented as a transition material between sub-cells.	32



Figure 23: Four components of a TPV system are a heat source, an emitter, a filter and a PV array which converts thermal energy to electrical energy. The emitter (combustor) irradiates photons upon the low bandgap PV array. The low-energy photons are recycled back to the emitter which improves the conversion efficiency of the photocell and overall TPV system [54].	33
Figure 24: Primary aerodynamic forces acting on (a) fixed-wing aircraft in horizontal flight and (b) rotary-wing aircraft in vertical flight.	35
Figure 25: Diagram of a conventional airfoil of an aircraft wing.	36
Figure 26: Logarithmic plot of air vehicle gross weight versus Reynolds number. Heavy aircraft operate in high Reynolds number ranges [65].	37
Figure 27: Air speed vs. air vehicle mass showing the approximate division of the two flow regimes [66].	39
Figure 28: Characteristic length of flyer versus Reynolds number defining various ranges of locomotion methods [70].	40
Figure 29: Miki's measurement of the unknown aerodynamic coefficient in order to calculate thrust force [49].	42
Figure 30: (a) The FOM of a rotary-wing blade is maximum for pitch angle range of 15-20°, and (b) the dragonfly cross section mimics Tsuzuki's optimal geometric design guidelines [69, 76].	44
Figure 31: Comprehensive figure showing thin-film deposition layers of the PolyMUMPs® process. Oxide etch features are also shown with resulting conformal topology.	47
Figure 32: Poly-crystalline growth process varies in the vertical direction due to grain boundary and lattice defects [83].	49
Figure 33: Maximum displacement versus maximum force for common MEMS actuators [85]. The black and green lines refer to MEMS and macro-sized actuators, respectively.	53
Figure 34: Maximum displacement versus maximum frequency for common MEMS actuators [85]. The black and green lines refer to MEMS and macro-sized actuators, respectively.	54

Figure 35: Thermal (solid expansion) actuator diagram. The hot arm expands more than the cold arm pushing actuator in the direction of the cold arm as depicted [86].	55
Figure 36: SEM picture of a comb drive showing basic components and electrical configuration.	56
Figure 37: SEM picture of interdigitized comb fingers and the electrical capacitance formed between each pair.	57
Figure 38: Folded spring design diagram for an electrostatic comb drive allowing left-to-right actuation at resonance.	60
Figure 39: Electromechanical equivalent circuit of a comb drive resonator.	63
Figure 40: SEM picture of orthogonal comb drive design showing an SEM close-up picture of the linear rack and master gear.	68
Figure 41: SEM picture showing the Poly1 master gear and Poly 2 hub axis. The gear rotates on the Poly0 ground electrode using dimples.	69
Figure 42: Poly2-Gold rotary wing showing the separation of the ribs from the spar for the photoresist hinge. A cross section of the photoresist hinge is shown in the top right.	71
Figure 43: Wing-T modeled in L-Edit using the MUMPs <sup>®</sup> fabrication process. The corrugation detail was achieved using alternating Poly0 spacer and Via-Dimple trench lines.	72
Figure 44: L-Edit 3-D render of Poly2-Gold wing sections attached to the master gear using Via etches. A close-up SEM of the wing attachment is shown on the right.	73
Figure 45: Shown on the left is the L-Edit top view of the master gear where the Poly2/Gold wing extends beyond the gear teeth. The effects of using a spacer are shown in the lower half. Shown to the right are the associated cross sectional views to conceptualize the desired topology effect using a spacer.	74
Figure 46: SEM picture illustrating the advantage of lowering the rack teeth 0.75 $\mu\text{m}$ using the dimple etch feature. Lowering the teeth increases the mesh alignment to the gear teeth.	75

Figure 47: SEM picture of a shaft collar with thickness of 4.75 $\mu\text{m}$ . The shaft collar, when stacked, forms the shaft to offset the wings above the substrate. ....	77
Figure 48: Flip chip assembly process. The MEMS device and substrate are bonded to the MEMS system using high temperature and/or high pressure. The device substrate floats away leaving behind the assembled MEMS device during an HF oxide release. ....	78
Figure 49: (a) Cantilever beams were measured under a Zygo Interferometric Microscope (IFM) and (b) calibrated in CoventorWare <sup>®</sup> to match the empirical deflections. ....	80
Figure 50: CoventorWare <sup>®</sup> analysis of Wing-G deflection. The maximum deflection occurred at the farthest rib tip at approximately 160 $\mu\text{m}$ out-of-plane. ....	81
Figure 51: CoventorWare <sup>®</sup> analysis of Wing-T deflection. The maximum deflection occurred at the farthest rib tip at approximately 210 $\mu\text{m}$ out-of-plane. ....	82
Figure 52: Simulated and analytical Wing-G deflection versus leading edge length. The simulated wing deflection closely resembles Analytical 1 values for length less than 1- mm ....	83
Figure 53: Simulated and analytical Wing-T deflection versus leading edge length. The simulated wing deflection closely resembles Analytical 2 values within 20%. ....	83
Figure 54: Simulated and analytical chord length results of (a) Wing-G and (b) Wing-T agree within 5%. ....	84
Figure 55: Graph of number of comb fingers versus the comb drive frequency. As shown, the number of comb fingers is best designed at or below 36 for high frequency application. As the number of fingers increase, the frequency trade-off of using Poly 1 or Poly 2 is subtle. ....	86
Figure 56: Simplified CoventorWare <sup>®</sup> FEA model of comb drive. The comb drive has a Manhattan Brick mesh of 25 x 25 x 5 $\mu\text{m}^3$ (x, y, z axes) partitions. ..	87
Figure 57: The effect of changing the flexure thickness is shown with (a) Poly1, (b) Poly2 and (c) Poly1-2 thickness. The flexures are all 200 $\mu\text{m}$ long and 2.5 $\mu\text{m}$ wide, and the applied voltage is 200 V. ....	88

Figure 58: Simulated and calculated peak-to-peak displacement of three types of comb drive actuators as a function of voltage. The effect of changing the material and thickness of the flexures is shown.....	89
Figure 59: The effect of changing the flexure length is shown with (a) 150 $\mu\text{m}$ , (b) 250 $\mu\text{m}$ and (c) 300 $\mu\text{m}$ long Poly1 flexures. Each comb drive is completely Poly1 with stacked comb fingers, and the applied voltage is 200V. The 200 $\mu\text{m}$ long flexures are shown in Figure 57a. ....	90
Figure 60: Peak-to-peak displacement of comb drive actuator as a function of voltage. The flexure length is varied from 150 $\mu\text{m}$ to 300 $\mu\text{m}$ in 50 $\mu\text{m}$ increments. Increasing the spring length is effective because the displacement is significantly increased while only slightly increasing overall mass. ....	91
Figure 61: Comb drive actuator force as a function of number of comb fingers. Approximately 4 $\mu\text{N}$ of force is available per actuator for 36 total comb fingers at 200 V.....	92
Figure 62: L-Edit drawing of outer and inner diameters containing dimples on the master gear. The average diameter (shown in gold) is used for frictional torque analysis. A simple force diagram of the friction force and actuator force is shown on the right.....	93
Figure 63: Net actuator force as a function of wing mass. The effect of increasing voltage allows for a larger wing mass. The x-intercept indicates the maximum wing mass for a particular voltage. Just less than 100 V is required to turn the master gear alone.....	94
Figure 64: Two-linked orthogonal comb drive actuators provide more push force. The pushrods are connected so each shuttle resonates together. ....	95
Figure 65: Net actuator force as a function of voltage for both Wing-G and Wing-T rotor designs. Four-link actuators are required for the Wing-G rotor while only three are necessary for the Wing-T rotor. ....	96
Figure 66: Maximum additional mass versus comb drive frequency in order to obtain suitable lift. Both the Glauvitz and Tsuzuki wings are shown at different Miki aerodynamic coefficients. For the configuration shown, between 7-11 kHz resonating frequency is necessary. ....	98

Figure 67: Additional mass available to produce lift versus required comb drive frequency. Decreasing the master gear size and teeth, increasing comb fingers above 36, and decreasing the spring constant is the optimum comb design. ....	100
Figure 68: Maximum additional mass versus comb drive frequency in order to obtain suitable lift for the quad-rotor design. Both the Glauvitz and Tsuzuki wings are shown at different Miki aerodynamic coefficients. For the configuration shown, up to 3.0 mg and 5.25 mg could be supported using the Tsuzuki and Glauvitz rotors, respectively. ....	101
Figure 69: Average power versus applied voltage for quad-rotor flying robot employing 4, 5 and 6-linked orthogonal comb drive actuators. ....	102
Figure 70: Detailed time versus temperature diagram of the MEMS oxide release process [77]. ....	105
Figure 71: Post-release SEM picture of the Wing-G quad-rotor. The picture clearly shows the vertical wing deflection. ....	106
Figure 72: Post-release SEM picture of the Wing-T 5-wing rotor. The picture clearly shows vertical wing deflection. The capability of the gear and wings to rotate about the gear hub confirms the chip was fully released. ...	106
Figure 73: Zygo IFM scan showing vertical deflection of the Wing-G leading edge (blue line). The leading edge deflected approximately 100 $\mu\text{m}$ . ....	107
Figure 74: Zygo IFM scan showing vertical deflection of the Wing-T leading edge (blue line). The leading edge deflected approximately 100 $\mu\text{m}$ . ....	107
Figure 75: Wing-G empirical data compared to calculated and simulated deflection. The measured data closely resembles the modeled data. ....	108
Figure 76: Wing-T empirical data compared to calculated and simulated deflection. The measured data closely resembles calculated and modeled data up to 0.5 mm. ....	108
Figure 77: SEM picture of Wing-T corrugation. The evaporated gold was likely the cause of the lower deflections compared to calculated and simulated results. ....	109

Figure 78: Screenshot of deflection of the Wing-T chord measured on the Zygo IFM (blue line). The corrugation is shown to the right, and the total deflection was approximately 11.5 $\mu\text{m}$ . .....	110
Figure 79: SEM picture showing the undesired Poly2 which seeped between the Poly1 gear teeth. The deflection was insufficient to lift the wing above the gear.....	110
Figure 80: (a) Photoresist pattern after 120 $\text{mJ}/\text{cm}^2$ dose exposure, 30 sec of 351 developing, and 2 min hot plate bake. (b) The photoresist dissolved after releasing the oxide in HF for 3.5 min and dissolving in DIW and isopropyl alcohol each for 10 min. ....	112
Figure 81: (a) Top view of MUMPs <sup>®</sup> 80 chip with Crystalbond <sup>™</sup> attachments on two Wing-T rotors, and (b) SEM picture of Crystalbond <sup>™</sup> successfully bonding the hinge.....	113
Figure 82: Calculated, simulated and experimental comb drive frequencies versus flexure length for (a) Poly1 and (b) Poly1-2 shuttle. The comb drives have 36 interdigitized fingers with a thickness of 3.5 $\mu\text{m}$ (stacked Poly1-2). .....	114
Figure 83: At 100 V, twice as much deflection was observed by lengthening the flexure lengths from (a) 200 $\mu\text{m}$ to (b) 250 $\mu\text{m}$ as predicted by simulated and analytical models.....	115
Figure 84: Electric signals for the orthogonal comb drive actuation scheme have a 90° phase angle difference. The shaded yellow section corresponds to the time period the teeth are engaged and turning the rotary wings. ....	116
Figure 85: Laboratory test setup to obtain two amplified oscillating signals with a difference in phase angle. ....	116
Figure 86: Screenshot of the lateral deflecting comb drives resulting in rotational actuation of the rack. The comb drives are comprised of a Poly1 shuttle and 52 shuttle teeth which resonated at 7.7 kHz.....	117
Figure 87: The poly1 shuttle becomes attracted to the substrate when a nitride breach occurs. In this case, the substrate is biased to the applied voltage, and the nitride serves as a dielectric between two different voltage potentials forming a capacitor.....	118

Figure 88: (a) An electrical short occurred because the balancing shuttle arm deflected and touched the high voltage wire, and (b) the clutch arm typically breaks from the rack at higher voltages. ....	119
Figure 89: SEM of a 2x5 thermal actuator array with high force output to rotate wings. The array was created as a proof-of-concept rotary actuator because a 6-link orthogonal comb drive actuator was not fabricated. ....	120
Figure 90: (a) At t=0 sec, a 20 Hz, 12 V actuation cycle is applied to the Wing-G rotor, and (b) the rotor rotates approximately 40 deg in one frame segment 66.67 ms. ....	121
Figure 91: (a) At t=0 sec, a 20 Hz, 12 V actuation cycle is applied to the Wing-T rotor, and (b) the rotor rotates approximately 40 deg in two frame segments of 123.33 ms. ....	121
Figure 92: The Poly2 wing interferes with the Poly1 actuator rack. The rack intermittently gets stuck in the Poly2 covered gear teeth as shown in the picture. ....	122
Figure 93: SEM pictures of the MEMS devices in order of assembly. The shaft ring (1) assembles around the hub of the master gear, and it is designed to repeat until sufficient height is achieved. The top of the shaft (2) holds the rotor (3) in place using the notch-lock design. ....	123
Figure 94: Vision of a quad-rotor robot employing multi-linked orthogonal comb drive actuators, biomimetic Wing-T rotors, power scavenging solar cells and CMOS control circuitry beneath the substrate. This model was created using SolidWorks <sup>TM</sup> . ....	129
Figure 95: MUMPs <sup>®</sup> 78 L-Edit mask design with Wing-G rotors, shaft ring assembly parts, and individual and orthogonal comb drives for empirical data. ....	131
Figure 96: MUMPs <sup>®</sup> 79 Chip 1L-Edit mask design with orthogonal actuators, 2-Link orthogonal comb drive actuator, Wing-G rotors, and measureable Wing-T designs. ....	132
Figure 97: MUMPs <sup>®</sup> 79 Chip 2 L-Edit mask design with orthogonal actuators, Wing-T designs, and orthogonal comb drive micro-wings. ....	133
Figure 98: MUMPs <sup>®</sup> 80 L-Edit mask design with orthogonal actuators, Wing-T designs, and orthogonal comb drive micro-wings. ....	134

Figure 99: L-Edit drawing of the photoresist hinge mask. The mask consists of hinge patterns for Wing-G (MUMPs<sup>®</sup> 79) and Wing-T (MUMPs<sup>®</sup> 80). Shown to the right is a close-up of one of the Wing-T reticules. For each wing 5, 7.5, 10 and 12.5  $\mu\text{m}$  hinge width patterns were designed on the mask. .... 138



## List of Tables

	Page
Table 1: Approximate size of common objects relative to MEMS.....	2
Table 2: Timeline of significant MEMS robot research [7-12]. .....	7
Table 3: Summary of representative land-based untethered MEMS robots [16-19]. .....	9
Table 4: Summary of representative miniature and MAV flying robots [15, 24-33, 38-41]......	19
Table 5: Summary of representative MEMS-based flying robots [20, 42-50]. .....	27
Table 6: Rotary-wing design guidelines for increasing FOM [69]. .....	44
Table 7: Typical PolyMUMPs <sup>TM</sup> layer material properties. The symbols C and T denote compressive and tensile residual stress, respectively [78-80]......	48
Table 8: Wing-T design parameters compared to Tsuzuki's recommendations. ....	73
Table 9: Required shaft height and assembly steps for the optimal pitch angle range of 15-20°. .....	77
Table 10: PolyMUMPs <sup>®</sup> foundry internal residual stress and thickness data for MUMPs <sup>®</sup> Runs 78-80. Tensile and compressive stress is denoted T and C, respectively [92]......	80
Table 11: Comparison of simulated and calculated maximum deflection of the MEMS wings. ....	84
Table 12: Calculated and modeled resonance frequency for various numbers of total comb fingers. For each, the shuttle is Poly 1 with 200 μm long and 2.5 μm wide flexures.....	86
Table 13: Summary of key parameters for a feasible rotary-wing MEMS robot design. ....	103
Table 14: Procedure for releasing and CO <sub>2</sub> drying the MEMS chips. ....	105

## List of Acronyms

AFIT	Air Force Institute of Technology
AFRL	Air Force Research Laboratory
CAD	Computer Aided Design
CMOS	Complementary Metal Oxide Semiconductor
CTE	Coefficient of Thermal Expansion
DARPA	Defense Advanced Research Projects Agency
DC	Direct Current
DIW	De-ionized Water
DMFC	Direct Methanol Fuel Cell
DOF	Degrees of Freedom
DRIE	Deep Reactive Ion Etch
FEA	Finite Element Analysis
FEM	Finite Element Modeling
FOM	Figure of Merit
GPS	Global Positioning System/Satellite
HF	Hydrofluoric Acid
IFM	Interferometric Microscope
LE	Leading Edge
LEV	Leading Edge Vortex
LF	Low Frequency
LIGA	Lithographie Galvanoformung Abformung ( <i>German</i> )
LPCVD	Low Pressure Chemical Vapor Deposition
LRC	Inductor-Resistor-Capacitor
MAV	Micro Air Vehicle
MEMS	Micro-Electro-Mechanical Systems
MFC	Micro-Flying Chip
MFI	Micro-Mechanical Flying Insect
MJSC	Multi-Junction Solar Cell
MST	Micro Systems Technology
MUMPS <sup>®</sup>	Multi-User MEMS Processes
NEMS	Nano-Electro-Mechanical Systems
PEM	Proton Exchange Membrane
PolyMUMPS <sup>™</sup>	Polysilicon Multi-User MEMS Processes
PV	Photovoltaic
RIE	Reactive Ion Etch
SEM	Scanning Electron Microscope
SOI	Silicon-Over-Insulator
TE	Trailing Edge
TPV	Thermo-Photovoltaic

# CONCEPTUAL STUDY OF ROTARY-WING MICROROBOTICS

## I. Introduction

Flying micro-robots offer unimaginable military capabilities and a multitude of engineering challenges. Also referred to as a micro-aerial vehicle (MAV), a flying micro-robot could provide our military with advanced methods of surveillance, reconnaissance and nuclear/biological/chemical detection. The most intriguing feature of a MAV is its diminutive size. Using a flying robot under  $1 \text{ cm}^2$ , the aforementioned applications would be hardly detectable. Further, the MAV could perform tasks in areas unthinkable to humans, such as a terrorist safe-haven, at negligible risk.

Of course, such implausible characteristics face great engineering challenges. The optimal MAV should operate both indoors and outdoors or during the day and night raising concerns about power and range limitations. The MAV could exploit a helicopter, airplane or insect design. Also, the flight control system of a MAV on the sub-centimeter scale is a daunting task in itself.

Such a small MAV is only practical using MEMS technology—capable of micrometer dimension geometry. MEMS and nano-electro-mechanical systems (NEMS) technology realize extraordinary devices daily. Complementary metal oxide semiconductor (CMOS) technology currently uses minimum features of 45 nm, and MEMS devices exist at less than the width of a human hair ( $\sim 100 \mu\text{m}$ ). Table 1 compares the size of MEMS and CMOS technology to other common objects.

**Table 1:** Approximate size of common objects relative to MEMS.

<i>Length (m)</i>	<i>Object</i>
$10^2$	Football field
$10^1$	3-story building
$10^0$	Height of child
$10^{-1}$	Computer mouse
$10^{-2}$	House fly
$10^{-3}$	Flea
$10^{-4}$	Width of human hair
$10^{-5}$	Limit of eyesight
$10^{-6}$	Bacteria, <b>MEMS</b>
$10^{-7}$	NEMS/CMOS fabrication
$10^{-8}$	Viruses, Nanotechnology
$10^{-9}$	DNA
$10^{-10}$	Hydrogen atom

Unfortunately, a MAV under  $1 \text{ cm}^2$  has not been successfully fabricated to sustain flight, let alone operate in realistic environments of unsteady state conditions (i.e.: temperature, air flow, moisture). Fortunately, significant research and empirical results exist as pieces to consider for an overall MEMS flying robot design.

## 1.1 Background

The goal of developing a MEMS flying robot at AFIT is in the third phase of research. Daniel Denninghoff was the first to investigate the topic at AFIT under funding support from AFRL/MNAV in 2005. The second phase of research was conducted by Nathan Glauvitz at AFIT in 2006. For each phase (including this thesis research), proof-of-concept MEMS devices were fabricated to support the research. Denninghoff successfully fabricated and demonstrated flapping motion on the MEMS scale, and Glauvitz fabricated rotary blade MEMS robots. However, none have achieved flight.

## **1.2 Research Objectives**

The research arena of developing a MEMS flying robot is open-ended and limited only in creativity. The objectives of this research include the following:

- Progress aerodynamic theory of micro-sized aerial vehicles.
- Define the theoretical limits and requirements of a MEMS flying robot.
- Design and fabricate a wing design based on modern research and experiments.
- Design, fabricate and demonstrate flight concepts at the MEMS scale using MEMS fabrication techniques on external power source.

## **1.3 Research Focus**

The focus of this research is to develop a rotary-wing flying robot—similar to a helicopter. The idea was originated by Miki, *et al* and further developed by Glauvitz whose research identified suitable MEMS actuators while ruling out unfeasible ones. This thesis improves upon MEMS fabrication lessons learned from his research while introducing additional design considerations.

## **1.4 Methodology**

Analytical expressions will be developed using collective research of MEMS actuators and miniature flight aerodynamics. The analytical results will be compared to modeled data using a MEMS Finite Element Analysis (FEA) software package. To validate the analytical and modeled data, MEMS devices will be designed using 2-dimensional computer aided design (CAD) software and fabricated using standard

MEMS techniques. The MEMS chips will be electrically characterized to verify the theoretical and modeled data and demonstrate the actuation scheme.

### **1.5 Assumptions/Limitations**

The MEMS fabrication process used at AFIT is limited to strict design rules and inevitable design features. Also, the MEMS fabrication process typically is a couple months; therefore, due to the 18-month graduate program only three fabrication attempts were feasible for this research. The empirical results were extracted using external power; although, the ultimate goal is to demonstrate wireless power scavenging capability.

### **1.6 Organization of Thesis**

The remainder of this thesis is organized chronologically and by level of technical detail. This document begins with an overview of relevant research towards a MEMS flying robot. Chapter 3 subsequently delves into theory required to design a MEMS flying robot. Chapter 4 discusses the MEMS designs and fabrication. Chapter 5 presents the analytical and modeled data, and Chapter 6 assesses the empirical results. The last chapter summarizes the results and comments on the successes and lessons learned.

## **II. Literature Review**

### **2.1 Chapter Overview**

The purpose of this chapter is to discuss past and present research related to fabricating a flying MEMS robot. Very few attempts exist of a solely MEMS fabricated flying robot; therefore, the following research areas are reviewed: autonomous land-based MEMS robots, miniature flying vehicles, miniature flying robots with integrated MEMS technology, and attempts of a MEMS flying robot. The last section presents the latest technology in micro-power devices capable of supplying untethered power.

### **2.2 A Brief History of Robots**

The thought of developing a flying MEMS robot spawned from the continuous research of ground based mobile robots. The field of general robotics has evolved over several years, without reference to the actual word, “robot”, until the early 20th century [1]. The concept of a robot originated from the human desire to do away with hard and dangerous work and have such jobs done by mechanical means [2]. Not all robots fell into this category, but it happened to describe the birth of American robotics. Although debatable, the first robots were industrial remote micromanipulators for the Atomic Energy Commission in the early 1950s. During this time, the well-known Nobel Prize recipient, Richard Feynman, delivered a historic speech which paved a road for miniaturization of electronics [3].

The 1960s and 1970s saw a spike in robotics manufacturing. Research began in the 1960s through the Defense Advanced Research Projects Agency (DARPA) funding of Artificial Intelligence labs at MIT, Stanford University, and Stanford Research

Institute. Shortly following, robotics became a profitable business after the development of spot-welding and spray painting robots for the automotive industry [4].

Robotics research stalled in the mid-late 1980s. The reason was contributed to the slow development of sensors and software which were pivotal to robotics [4]. Sensors were required to detect movement, touch, and error. Further, software programming was necessary for onboard robots to make sense of the sensor-detected information.

Fortunately, researchers were making progress in the 1980s with micro-systems technology (MST). According to Middelhock, much credit was given to Simon Hiddelock for cultivating the area of MST with extensive research in silicon sensors [5]. The year 1987 was a landmark as the first IEEE Micro Robots and Teleoperators Workshop was held. The results of the workshop led to the famed report, *The Workshop on Micro-electro-mechanical Systems (MEMS) Research* [6]. Thereafter, the workshops met regularly as IEEE/ASME MEMS workshops.

The late 1980s and 1990s saw a significant increase in MEMS research. In 1987, T. Fukuda, *et al* proposed micro-assembly tweezers, one of the first significant MEMS robots, to further micro-assembly technology [7]. By the 1990s, the development of micro-robots utilizing the photolithography process was possible. Simple MEMS building blocks such as the comb drive, cantilever beam, bimorph beam, electrostatic motor, and thermal actuator were demonstrated. The first three-dimensional (3-D) MEMS insect-based robot was proposed in 1992 by K. Suzuki, *et al* [8] which fueled future biomimetic research. In 1994, T. Fukuda, *et al* appeared, again, with experimental results for a novel swimming robot [9]. Eventually, flying MEMS research debuted in



the early 1990s, and the first attempt of a flying MEMS robot was achieved in 1994 by Isao Shimoyama, *et al* [10, 11]. A summary of significant MEMS robot research is summarized below in Table 2.

**Table 2:** Timeline of significant MEMS robot research [7-12].

<i>Year</i>	<i>Research Topic</i>
1987	Master/Slave Tweezers
1989	1 cm <sup>3</sup> inch robot
1991	Magnetostrictive mover in pipe
1992	Insect-based robot
1993	Ciliary-motion conveyor
1994	Pipe inspection robot
1994	Swimming robot
1994	Flying robot

In 1993, the first feasibility study on MAVs was fulfilled by the RAND Corporation [13]. The study suggested that the development of insect-size flying vehicles could give the U.S. military services a significant advantage. In the following two years, a more detailed study was completed at Lincoln Laboratory, resulting in the DARPA MAV research workshop in 1995 [14]. In the fall of 1996, DARPA funded formal MAV research programs under the Small Business Innovation Research (SBIR) program [15].

So far, the term microrobotics has been used loosely. Technically, a microrobot is defined as a robot with its largest dimension (length, width, or depth) less than one millimeter. However, generally it has been acceptable to refer to a robot as “micro-” if it possesses a feature in the micrometer range. More appropriately, the remainder of this thesis will refer to robots greater than one millimeter as a miniature robot.

### 2.3 Untethered Land-Based MEMS Robots

The literature search presented in this section concentrates on untethered land-based miniature MEMS robots. As shown in Table 2, flying robotics is a modern research area. Flying MEMS robots were designed using concepts adapted from untethered land-based MEMS robots such as wireless power and actuation methodology. Therefore, MEMS robotics research is discussed briefly in this section before delving into existing flying robots.

Most land-based MEMS robots mimic the movement of crawling insects. In 2003, Hollar, *et al* fabricated a crawling robot made of polysilicon and powered from solar cells. Hollar's robot was capable of crawling 3 mm using electrostatic-controlled legs and is shown in Figure 1a [16, 17]. A crawling wireless MEMS robot was devised by Dartmouth engineers in 2006 pictured in Figure 1b. The robot was powered with an underlying electric grid, and the robot crawled and steered using capacitive scratch drive actuation and a cantilever beam, respectively [18]. In 2007, Dalhousie University developed a novel microcrawler which uses frictional force to its advantage. The microcrawler employs thermal actuators to travel down power rails [19]. A schematic of the Dalhousie University robot is shown in Figure 1c. A summary of these representative MEMS robots is shown in Table 3. For further examples, refer to Power Scavenging MEMS Robots [20] and Ebefor's survey of conveyor micro-robotics [21].

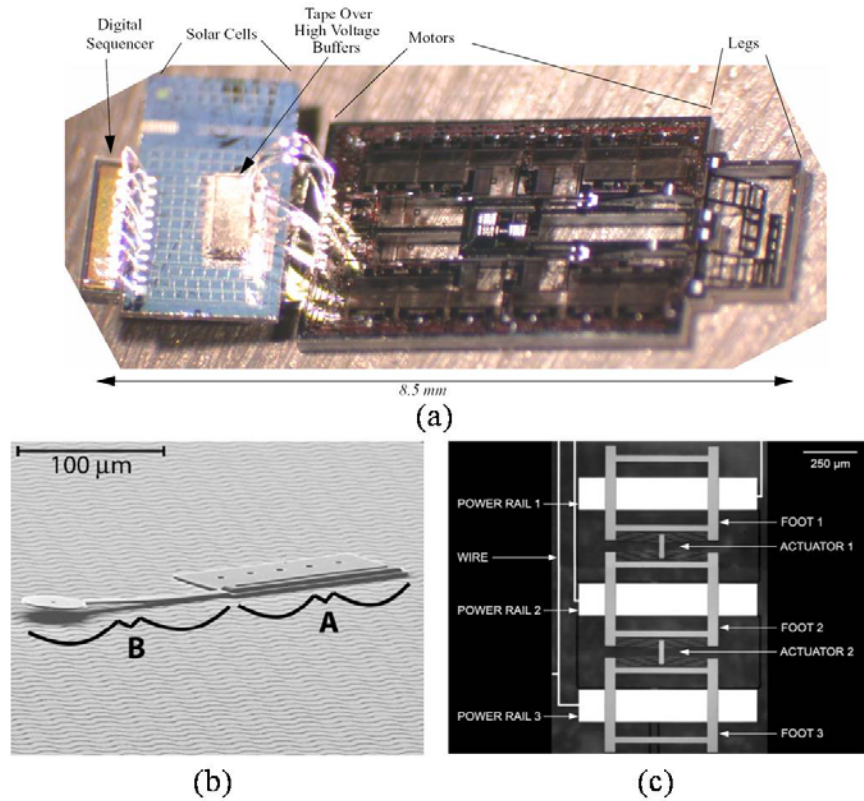


**Figure 1:** (a) Hollar's crawling silicon solar-powered robot, (b) Dartmouth's crawling and steerable polysilicon robot and (c) schematic of Dalhousie University frictional microcrawler.

**Table 3:** Summary of representative land-based untethered MEMS robots [16-19].

<i>Robot</i>	<i>Hollar Robot</i>	<i>Dartmouth Crawler</i>	<i>Dalhousie Crawler</i>
Year	2003	2006	2007
Largest dimension	8.5 mm	250 μm	1.4 mm
Power Source	solar	electric grid	power rail
Actuator	electrostatic	scratch drive	thermal
Speed	12.5 μm/sec	200 μm/sec	700 μm/sec
Other features	shuffles sideways	crawls and steers	friction-based; reversible

## 2.4 Miniature Flying Robots

Undoubtedly, most flying robots are not small enough to require MEMS processing; therefore, they are presented in this section as miniature flying robots. The timeframe of the following background information dates from the start of DARPA's initiative to develop a micro (technically, miniature) aerial vehicle (MAV) with less than a 15 cm wingspan. Several macro-size fixed-wing MAVs exist as a result of DARPA's project. The focus is towards the MEMS scale, but representative miniature robot MAVs are briefly presented here. MAV robots are classified into three groups—flapping, rotary and fixed wing.

The first-ever autonomous MAV flight was achieved by MicroStar at Lockheed Martin. MicroStar has a wingspan of approximately 22.8 cm and weighs 110 grams. The MAV is powered using lithium ion batteries which provide 25 minutes of endurance at a top speed of 25 mph [22, 23]. MicroStar provides real-time imagery from 50-300 ft altitude via datalinks to ground computers [24]. MicroStar is shown in Figure 2a including the underwing electronics platform in Figure 2b.

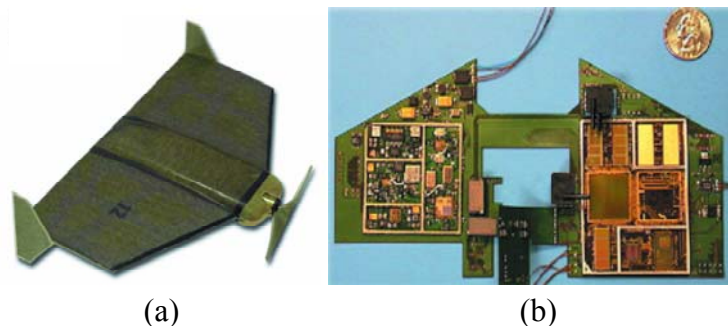


**Figure 2:** (a) Lockheed Martin MicroStar with 22 cm wingspan, 110 grams mass and 25 minute continuous runtime. (b) MicroStar's underwing electronics platform is shown on the right. [24].

In 2001, AeroVironment Inc. created Black Widow, a fully autonomous fixed-wing MAV. Black Widow holds the MAV record (< 100 grams) for longest endurance of 31 minutes (as of 2006) [22]. Black Widow is capable of down-linking a color video feed to the pilot. Black Widow was fabricated of expanded polystyrene foam for a total mass of 80 g. The wingspan, top speed and range of Black Widow are 6 inches, 30 mph and 1.8 km, respectively. The propulsion system of Black Widow is a small propeller motor accounting for 62% of its total mass. The power supply is a modern lithium battery capable of powering the MAV for 30 minutes [25]. The Black Widow is pictured in Figure 3a.

In 2002, a group from the University of Florida took the Black Widow concept one step farther with a flexible-wing design. The flexible-wing assists in low-Reynolds number ranges ( $10^4 - 10^5$ ) [26] by allowing the lifting surface to move and deform for favorable aerodynamics. The Reynolds number is the ratio of inertial to viscous forces used to identify air flow regimes. Unfortunately, the Reynolds number decreases significantly for MAVs because of their small dimensions and slow airspeed [26]. Low-Reynolds number ranges are volatile under wind speed changes—fluctuating up to 30%. The ability of the wings to adapt is attained through extension and twisting of the wing, known as adaptive washout. The shape of the wing changes as a function of the airspeed and angle of attack [27].

The flexible-wing MAV is shown in Figure 3b. The MAV is designed to carry a small camera for reconnaissance or surveillance missions. The novel wing is fabricated from a carbon fiber skeleton and thin latex rubber membrane. The total weight is 52 g,

and the wingspan varies to a minimum of 5 inches, or 12.7 cm. The power supply is a conventional lithium battery giving the MAV a runtime of approximately 15 minutes at 15-25 mph airspeed [27].

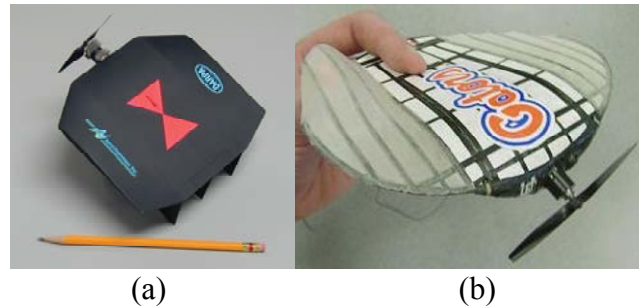


**Figure 3:** (a) AeroVironment and CalTech's Black Widow MAV with 6 inch (15.2 cm) wingspan. Black Widow can fly continuously for 30 min with a 1.8 km range [25, 28], and (b) University of Florida flexible-wing design with a wingspan of 5 in (12.7 cm) and run time of 15 min at 15-25 mph [27].

In 2002, AeroVironment and T.N Pornsin-Sirarak, *et al* from the California Institute of Technology developed MicroBat, a novel flapping MAV, or ornithopter. MicroBat holds two records: (1) the first ever battery-powered, electric motor-controlled flapping MAV and (2) the longest-endurance flapping flight of 25 minutes ( $< 100$  grams) [22]. The flapping motion was realizable using a 22:1 gear ratio transmission capable of 42 Hz flapping frequency at 1.4 W. The mass and wingspan were 14 grams and 9 inches (22.9 cm), respectively. Although initially powered using one NiCd battery, two lithium batteries produced drastically longer runtimes up to 25 minutes. The flapping motion was driven by a 4.5 V DC brush motor which required a power conversion from the battery [15]. Figure 4a shows MicroBat in its final configuration, and the transmission is pictured in Figure 4b.

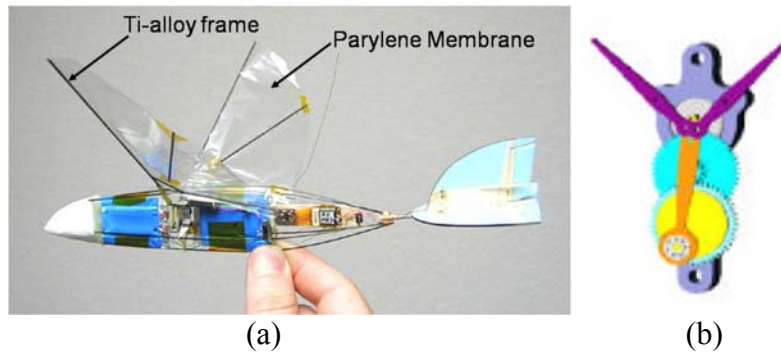


**Figure 4:** (a) MicroBat ornithopter developed by AeroVironment and Pornsin-Sirarak, *et al.* The wingspan, mass, and run time are 9 inches, 14 grams and 25 minutes (with two lithium batteries), respectively [15]. (b) The 22:1 gear ratio actuating the wings up to 42 Hz at 1.4 W [29].

MicroBat required integrated MEMS technology to fabricate the wings. An intensive wing study revealed titanium-alloy metal (88% Ti, 6% Al, 4 % Vanadium, 2% other) and poly-monochloropara-xylylene (parylene-C) as the best wing frame and wing membrane materials, respectively. Titanium is favorable over silicon because it is less fragile, lightweight, ductile and easy to etch. Parylene was chosen as the membrane primarily due to its adhesion properties to titanium [29-31].

MicroBat's wings were fabricated using a 250- $\mu\text{m}$  thick titanium-alloy substrate. A dry resist was patterned above the substrate prior to isotropic etching the wing frame with an  $\text{HF}:\text{HNO}_3:\text{H}_2\text{O}$  (5:2:100) solution for 20 minutes. Potassium Hydroxide (KOH) was used to strip the resist to prepare for the membrane fabrication, and another coat of dry resist was applied and patterned for the parylene deposition. Two coats of parylene were required to strengthen the membrane [29-31]. The fabrication process is shown in Figure 5.

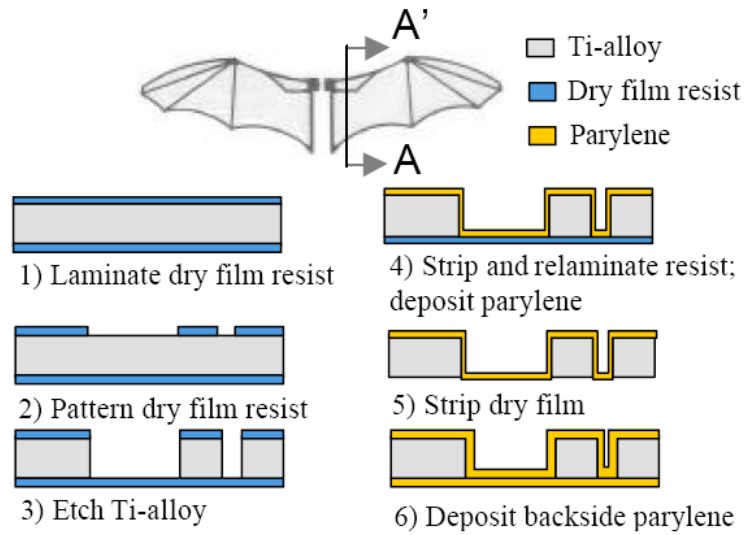


**Figure 5:** MEMS fabrication process for wings of MicroBat MAV [29].

Stanford University, with assistance from SRI and Intel Corporation, are developing a “Mesicopter”. The goal of the design team is to build the world’s smallest flying robot, and their simple theoretical models are feasible for 30 minutes of sustained flight. The Mesicopter is autonomous and designed to gather atmospheric data using onboard sensors. The initial Mesicopter prototype pictured in Figure 6 has a chassis of approximately 1.5 cm x 1.5 cm weighing about 3 grams. The robot employs four rotors each of 1.5 cm diameter and driven by commercially available DC motors. The rotors were fabricated using an additive and subtractive milling process. The power system includes zinc-air battery cells which deliver 50 mA to turn the four rotors. The sensor package is designed to eventually use a MEMS gyro for control and stability and even a small GPS sensor [32, 33].



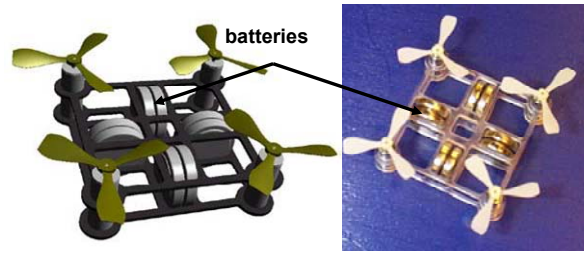


**Figure 6:** Initial prototype of Stanford's Mesicopter designed to hover 30 minutes. The four rotor design is 1.5 cm x 1.5 cm weighing 3g [33].

Future improvements of the Mesicopter are ongoing. The team is looking to use advanced metal stamping and casting for an enhanced rotor design. The motor is under improvements at Stanford's Rapid Prototype Laboratory (RPL) which utilizes tools fabricated in LIGA (*German, Lithographie Galvanoformung Abformung*) and silicon etching processes. Tests showed the experimental motor successfully ran at 10,000 RPM, but more research is required. Likewise, the power source is under development by SRI which is capable of combining the highest level of power and energy densities into one battery package. The latest prototype, shown in Figure 7, is designed slightly larger at 2.5 cm x 2.5 cm with completely redesigned rotors capable of four times the lift of the initial Mesicopter [32, 33].

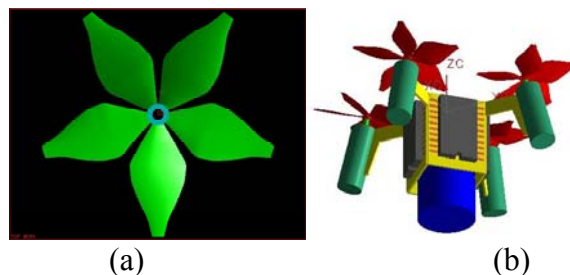


**Figure 7:** (a) Improved rotor designed with four times more lift than initial prototype, and (b) future 2.5 cm x 2.5 cm prototype employing redesigned rotors [33].

The Micromechanical Flying Insect (MFI) project team from the University of California-Berkeley made prodigious findings for flapping-wing flight. Beginning in 1998, Fearing, *et al* created several MFI prototypes [34]. The early MFI design incorporated a 4-bar linkage mechanism which was created from laser cut stainless steel as shown in Figure 8a [35]. The flapping actuation is attained through piezoelectric unimorph beams. The unimorph beams consist of purely elastic and piezoelectric material bonded together. The piezoelectric material is strained longitudinally and transversely when an electric field is applied; thus, causing deformation [36].

In 2003, the MFI team replaced the stainless steel frame with composite carbon fiber. The carbon fiber change dramatically increased stiffness, cut weight and simplified construction. The final configuration was a 26 joint prototype with four degrees of freedom (DOF) as shown in Figure 8b. Initial tests of the modified MFI resulted in 160 Hz flapping frequency compared to the previous model of 133 Hz [37].

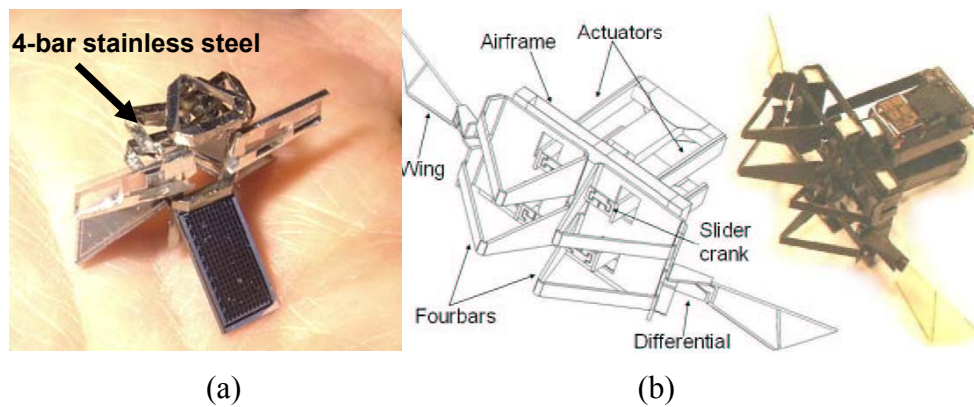


**Figure 8:** (a) Early prototype of the MFI using a stainless steel 4-bar frame, and (b) most recent prototype using a composite carbon frame [34, 37].

Students attending Delft University of Technology developed various flapping MAVs under the name DelFly. The vision of DelFly was to mimic the flight of both birds and insects. DelFly I has a 30 cm wingspan, weighs 16 grams, and has the ability to fly forward, backward and hover at speeds as low as 0.5 m/s. The slow flight speed is advantageous for the onboard camera which communicates via its 35 MHz communication receiver [38]. DelFly I is shown in Figure 9a.

The most successful DelFly configuration, DelFly II, consists of two pairs of wings that flap in a clapping motion. DelFly II, shown in Figure 9b, is capable of 15 minutes of level flight or 8 minutes of hovering. The power source is a lithium ion battery which delivers 130 mA-hr to the camera and DC motor. The motor turns the crankshaft drive system which flaps the wings. Improvements to miniaturize DelFly II to a 5 cm wingspan are under development. The new configuration, DelFly Micro, will strive to be the smallest MAV equipped with an onboard camera [38, 39]. A picture of DelFly Micro is shown in Figure 9c.

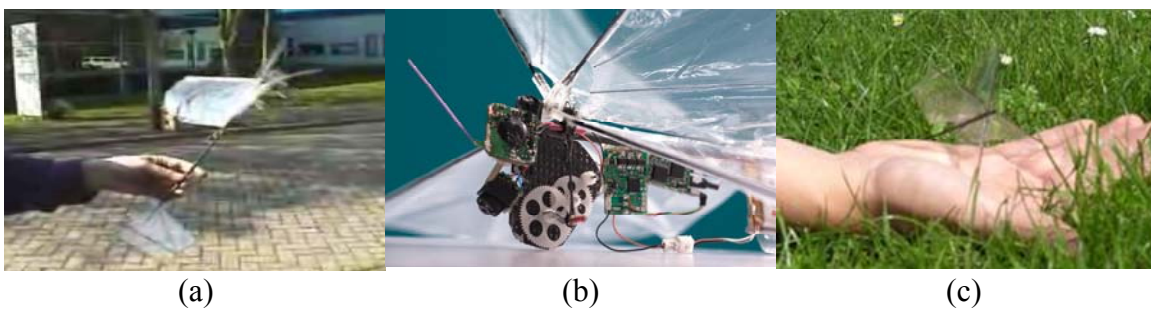


**Figure 9:** Three versions of DelFly exist in order of largest to smallest are (a) DelFly I, (b) DelFly II and (c) DelFly Micro [38, 39].

In 2007, Harvard researcher Wood, *et al* created the MicroGlider. The glider spans 10 cm, weighs 2 grams and is capable of autonomous flight. The wing airfoil was unconventionally designed after research showed an increase in aerodynamic drag force in the range of low Reynolds Numbers ( $\sim 7000$ ). The airfoil and control surfaces were fabricated out of a high Young's Modulus composite material. MicroGlider's navigation controls include 10 mm piezoelectric actuators to create torque on the control surfaces at the tail end of the glider. The actuator power source was located near the middle and was comprised of one 20 mA-hr lithium ion polymer battery. Also included was amplifying circuitry due to the actuators' 200 V input. MicroGlider consumes approximately 400 mW yielding up to 10 minutes of gliding [40]. A diagram of MicroGlider and its design features are shown in Figure 10. Table 4 summarizes all miniature flying robots presented above.

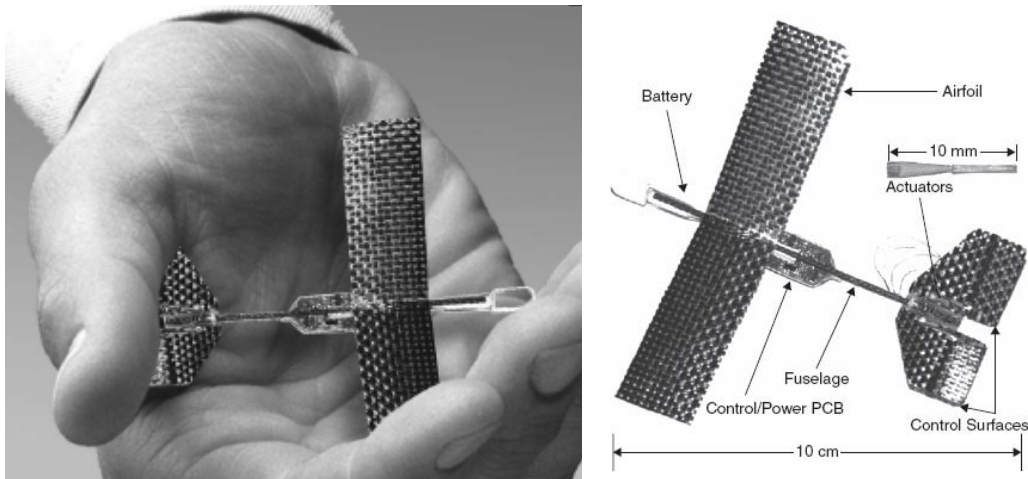


**Figure 10:** MicroGlider which uses tail end control surfaces actuated by piezoelectric actuators. MicroGlider has a 10 cm wingspan and can glide for 10 minutes [40].

**Table 4:** Summary of representative miniature and MAV flying robots [15, 24-33, 38-41].

<i>Robot</i>	<i>Black Widow</i>	<i>UF flex wing</i>	<i>MicroBat</i>	<i>Mesi-copter</i>	<i>MFI</i>	<i>DelFly</i>	<i>Micro-Glider</i>
Year	2001	2002	2002	2000	2003	2007	2007
Type	fixed	fixed	flapping	rotary	flapping	flapping	glider
Largest dimension	15.2 cm	12.7 in	22.9 cm	1.5 cm	2.5 cm	30 cm	10 cm
Mass	80 g	52 g	14 g	3 g	----	16 g	2 g
Power Source	Li-ion battery	Li-ion battery	Li-ion battery	zinc-air battery	solar	Li-ion battery	Li-ion polymer battery
Run time	31 min	15 min	25 min	30 min*	30 min*	15 min	10 min
Speed	13.1 m/s	6.7-11.1 m/s	11.1 m/s	----	----	----	700 $\mu$ m/sec
Achieve flight (Y/N)?	Y	Y	Y	N	N	Y	Y
Notable Features	record MAV endurance	flexible wing design	first ever battery power MAV	integrated sensor package	piezo-electric unimorph actuators	capable of hovering	piezo-electric actuators

\*Theoretical Value Only

## 2.5 Flying MEMS-Based Robots

In 1993, Kubo, *et al* published a study on insect-based flying micro-robots. The research truly opened doors for fabricating a MEMS-scale flying robot. The study recognized the following important low-Reynolds number characteristics: (1) insects make good use of the elasticity of external skeletons to move their wings allowing high frequency flapping, (2) viscous forces (drag) become dominant as size decreases, (3) small insects use drag to their advantage using a rowing motion, and (4) aerodynamic forces are underestimated when using conventional calculations [42, 43].

Simple flapping micro-robot models were created via semiconductor fabrication techniques. Figure 11a shows the basic flapping wing concept using an elastic film surrounded by a frame. On the upstroke, the elastic film separates from the frame

allowing air to flow through the gap and decreasing drag force. Contrary, on the down stroke the film is pressed up against the frame eliminating the gap. The kinematics are shown in Figure 11b where plane A moves in the opposite direction as B and C which actuate the wings [42].

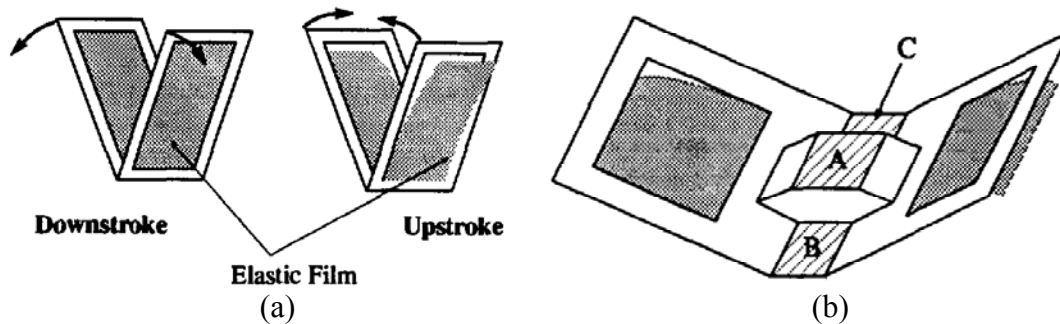


**Figure 11:** (a) Simple flapping concept using an elastic film and frame, and (b) flapping concept integrated in a closed-loop system; plane A is actuated in the opposite direction of B and C which actuate the wings [42].

Kubo, *et al* fabricated sub-millimeter flapping wings as depicted in Figure 12 [42, 43]. The wing was designed to utilize drag force by changing the shape of the wing on the up and down strokes. The wing was made of 0.1- $\mu\text{m}$  thick nickel sandwiched between two 1- $\mu\text{m}$  thick polyimide layers. The wing structure was approximately 400  $\mu\text{m}$  x 800  $\mu\text{m}$  and is applicable to a 1 mm micro-robot. Theoretically, the wing could be actuated by using magnetic resonance equal to the natural frequency of the wing [43].

Chan, *et al* designed a flying MEMS robot in 2004 [44]. The structure was made from silicon using polymer MEMS technology and utilized many of Kubo's concepts. The wings were fabricated as bimorph thermal actuators each with dimensions of 1000  $\mu\text{m}$  x 100  $\mu\text{m}$  x 0.8  $\mu\text{m}$  which match to insects of homoptera classification. Homopteras,

such as an aphid, have masses ranging from 0.1 – 1.0 mg and flapping frequencies between 60–177 Hz; these ranges were the design targets [44].

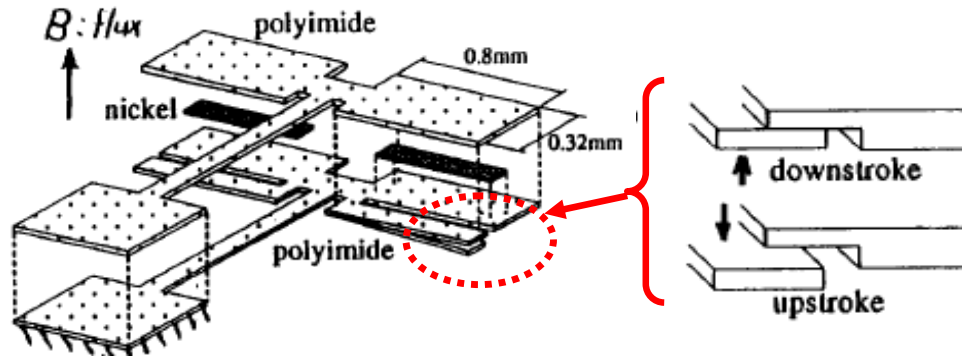


**Figure 12:** MEMS wing fabricated from nickel sandwiched between polyimide layers which is designed to utilize drag forces with a different wing shape on up and down strokes [43].

The wing actuator principle utilized sandwiched layers of material each possessing a different coefficient of thermal expansion (CTE). Platinum was the middle layer, and the top and bottom were comprised of parylene. The fabrication and actuation schemes are shown in Figure 13a. A 6 V on-off pulse was applied between the platinum layers. At 6 V, the layers deflect upward as a result of thermal expansion differences and return to their original position at 0 V. Flapping frequencies up to 200 Hz were demonstrated which is sufficient for a micro-flying chip (MFC) the size of an aphid. The actuation scheme is described in Figure 13b.

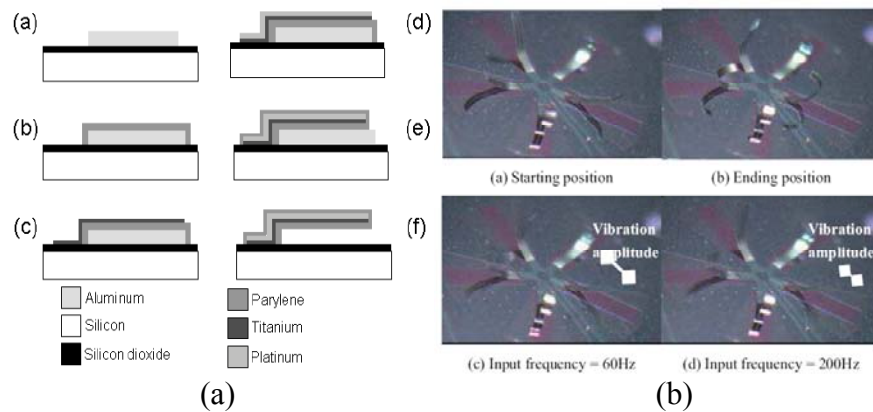


**Figure 13:** (a) Cross section of layers used to fabricate the MFC wing actuator, and (b) actuation scheme of applied 0 V and 6 V [44].

A conceptual design which integrates Kubo's ideas is shown in Figure 14. In this case, the elastic film is parylene, and the frame is platinum. The platinum heater is designed as a grid structure to prevent the parylene from deforming [44]. Further, the actuators can be fabricated as different lengths to add a rotational DOF. By using a symmetrical quadrant design, rotation is possible by actuating particular quadrants of wings. Normal flight is possible because the rotational quadrants cancel each other when all four are actuated simultaneously. Aside from the wing fabrication, the integrated MFC project was not completed most likely due to power constraints.

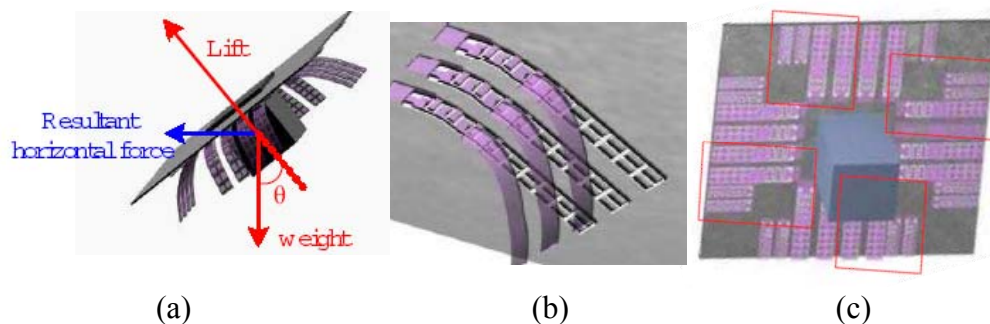


**Figure 14:** (a) MFC force diagram, (b) close-up of wing geometry and (c) quadrant array which allows the MFC to rotate or fly level [44].



A MEMS-scale rotary flight micro-robot was developed by Miki, *et al* in 2001. The novel feature of the micro-rotating wing robot was wireless actuation via a magnetic field. The most successful prototype was comprised of 900- $\mu\text{m}$  long nickel-iron (NiFe) magnetic wings weighing 165  $\mu\text{g}$  shown in Figure 15a. Successful demonstration of autonomous flight was achieved at 570 Hz rotation in the presence of an 8 kA/m external magnetic field [45-49]. Wing rotation was achieved using an alternating magnetic field. The wing's magnetization changed as the wings rotate, and a torque was created under a magnetic field. For rotation angles between 0-90°, torque opposed the direction of rotation, but aided rotation for angles between 90-180°. This anisotropic magnetization behavior was a direct result of the two thin film magnetizing strips shown in Figure 15b [49].

The layer structure of the MEMS wings consisted of 10 nm chromium for adhesion, 100 nm seed layer of nickel, and 10  $\mu\text{m}$  electroplated NiFe. A hydrofluoric acid (HF) solution was used to etch away the sacrificial silicon dioxide. The wing flaps were bent at a 45° angle to create additional lift. A sharpened glass rod, acting as the axis of rotation, was glued to the center of the wings. A hollow, glass tube shaft was used to support the rotation axis. When the lift of the wings equaled the mass of the robot, a disk pressed against the body, lifting the robot in the air [48].

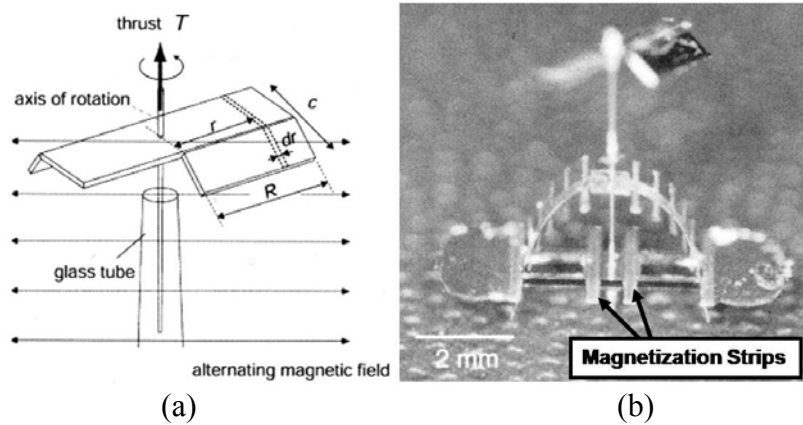


**Figure 15:** (a) Diagram of Miki's micro-rotary wing and (b) the fabricated robot with rotating wings in an alternating magnetic field [49].

In 2006, Daniel Denninghoff designed novel flapping-wing MEMS robots. The wings were comprised of a bilayer stack of polysilicon and gold fabricated in the PolyMUMPs<sup>®</sup>, or MUMPs<sup>®</sup>, process. After a post-fabrication release of the sacrificial silicon dioxide, the bilayer wing relieved its tensile residual stress. Tensile stress relief resulted in upward vertical deformation, or the upstroke of the wing. Denninghoff also pointed out a downward vertical deformation was possible because the thermal expansion coefficients of polysilicon and gold vary considerably. The top layer of gold expanded more than polysilicon which made the bilayer deflect downward, or the downstroke of the wing. The thermal load was produced by an external 660 nm wavelength diode laser, and 175 mW energy from the laser was absorbed optothermally which conducted throughout the bilayer wing [20].

Figure 16a presents representative micro-robots designed by Denninghoff. Results showed the best robot configuration used one pair of flapping wings similar to an insect with a wingspan of 500  $\mu\text{m}$ . Unfortunately, the aerodynamic lift force was

dominated by the robot's mass. A solution for future research was to implement an additional wing frame made of polysilicon. The frame would support a very thin and lightweight material thus increasing the wingspan and lift force, but only slightly increasing overall mass. The optimal design is shown in Figure 16b.

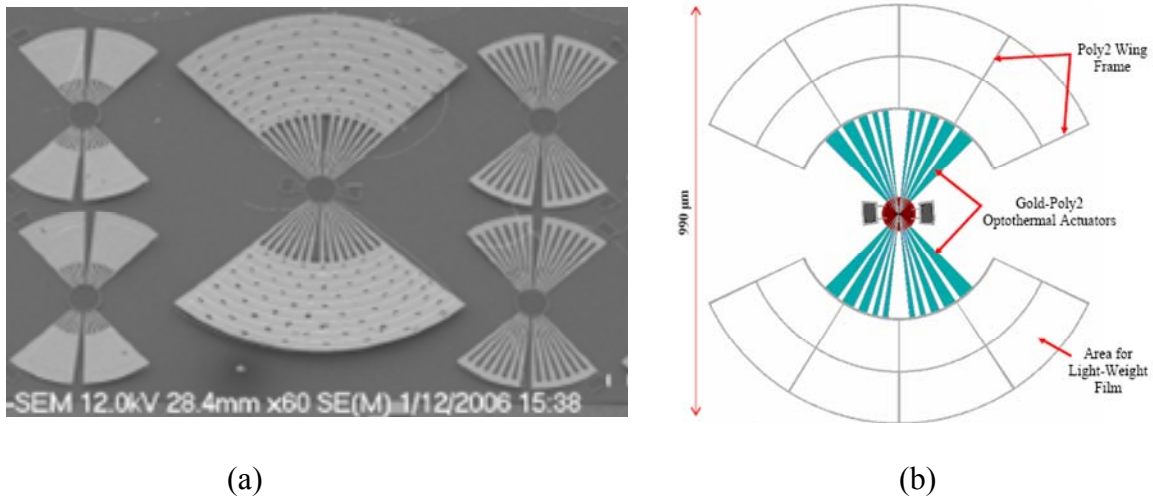


**Figure 16:** (a) SEM photographs of various flapping wing MEMS robots and (b) optimal design for achieving MEMS scale flight [20].

Further research towards a flying MEMS robot at AFIT was conducted by Nathan Glauvitz in 2007. Instead of insect-based flapping flight, Glauvitz focused his attention on achieving flight using rotary wings. Glauvitz' approach was to use two orthogonal MEMS comb drive actuators to drive a gear with attached wings. The orthogonal actuators were designed to operate using identical voltage waveforms with a  $90^\circ$  phase difference. The wings were custom-designed to utilize a flexible photoresist hinge to achieve the desired angle of wing deflection [50].

The comb drive actuation scheme and hinged wing are shown in Figure 17. The comb drives were designed to operate at approximately 11.3 kHz and turn the wing's

gear at 754 Hz—theoretically sufficient for flight. However, experimental results were not provided due to shortcomings of the fabrication process. Experimental results from the photoresist-hinged wing confirmed using only the top layer of polysilicon in the MUMPs<sup>®</sup> process was necessary [50]. Figure 17 shows a theoretical diagram of a feasible rotary wing flying robot employing four rotors; similar to the Mesicopter concept [32, 33]. Several comb drives are combined beneath the wings to increase the force to turn the gear and rotor. The center of the robot is open for a possible onboard power source for autonomous capability. A summary of representative MEMS-based flying robots is shown in Table 5.

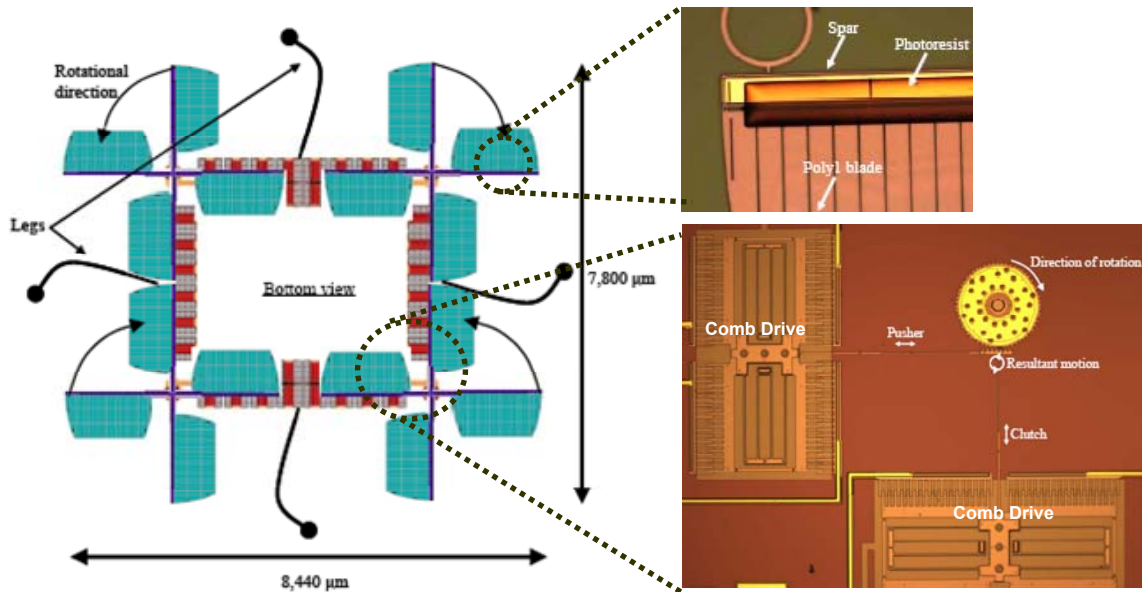


**Figure 17:** Vision of a rotary-wing MEMS flying robot as a result of Glauvitz’ research. The robot consists of four rotors and several comb drive actuators turning the wings’ gears. The open area in the middle could be used for an onboard power source [50].

**Table 5:** Summary of representative MEMS-based flying robots [20, 42-50].

<i>Robot</i>	<i>Kubo</i>	<i>Miki</i>	<i>Chan</i>	<i>Denninghoff</i>	<i>Glauvitz</i>
Year	1993	2001	2003	2006	2007
Type	flapping	rotary	flapping	flapping	rotary
Largest dimension	1 mm	2 mm	2 mm	0.99 mm	8.4 mm
Actuation method	magnetic resonance	alternating magnetic field	thermal expansion differences	optothermal expansion	electrostatic comb drive resonator
Achieve flight (Y/N)?	N	Y	N	N	N
Notable Features	first MEMS flying robot concept	570 Hz wing rotation	200 Hz flapping	powered by 660 nm diode laser	designed to use solar power

## 2.6 Power MEMS and Photovoltaic Devices

Integrating an onboard power source is considered one of the most challenging aspects of developing a MEMS flying robot. Power requirements include small device area, lightweight, efficient, environmentally friendly and the capability of producing a high operating voltage and power in the micro- to milli-Watt range. This section presents the latest technology in power MEMS and photovoltaic devices.

### 2.6.1 Power MEMS

Power MEMS were first studied by Epstein and Senturia at MIT and refer to micro-devices which generate power or pump heat [51]. Power MEMS utilize hydrocarbon liquid which possesses a high specific energy compared to conventional sources as shown in Figure 18. Power MEMS encompasses various technologies such as thermoelectrics, fuel cells and thermo-photovoltaics (TPV).

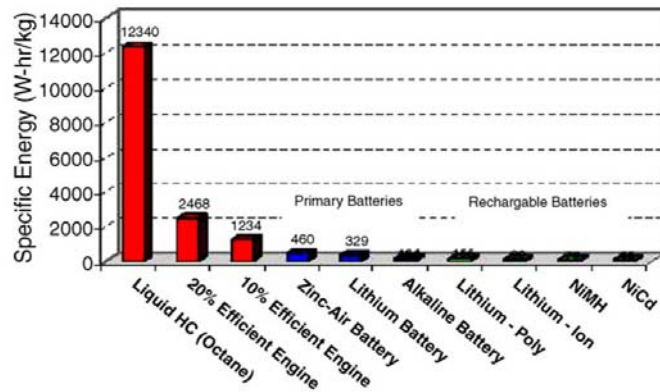


**Figure 18:** Specific energy of liquid hydrocarbon compared to conventional engine, primary batteries and rechargeable batteries [52].

One sector of power MEMS is thermoelectric generation. Thermoelectric generation was proposed by Sitzki, *et al* of University of Southern California to eliminate small moving parts found in micro-engines; thus, increasing reliability. Sitzki developed a novel “swiss roll” burner to work in conjunction with a thermoelectric generator. The burner, shown in Figure 19, is an efficient heat exchanger which produces higher enthalpy reactants conducive for combustion. Theoretically, the system is capable of 0.1 W with a device size of  $0.04 \text{ cm}^3$  [53, 54]; however, only larger physical models exist to support the theoretical limits.



**Figure 19:** Stanford’s “Swiss Roll” burner concept to be used in conjunction with a thermoelectric generator [53].

Micro-fuel cells utilizing hydrocarbon fuels are gaining popularity. A micro-fuel cell is portable and converts chemical energy (fuel) into usable electrical energy in a catalytic process. The catalytic process occurs at each electrode; ions are generated and conducted via an electrolyte medium while creating free electrons available to drive an external load [55].

Micro-fuel cells are classified into two groups—Proton Exchange Membrane (PEM) and Direct Methanol Fuel Cells (DMFC). The major differences of each type’s catalytic process are shown in Figure 20. Conventionally, micro-fuel cells are stacked vertically to increase the open-circuit voltage rating. In 2002, Lee, *et al* developed “flip-flop” interconnects at Stanford University where fuel cells can be fabricated side-by-side in series [56]. The best power-producing cell was fabricated in 2005 by Yu, *et al*. The PEM silicon-based cell utilized hydrogen fuel and was reported to achieve  $195 \text{ mW/cm}^2$  with a device area of  $5 \text{ cm}^2$  [55, 57]. Despite the sufficient power of micro-fuel cells, one major setback is fuel cell storage on a MEMS flying robot.

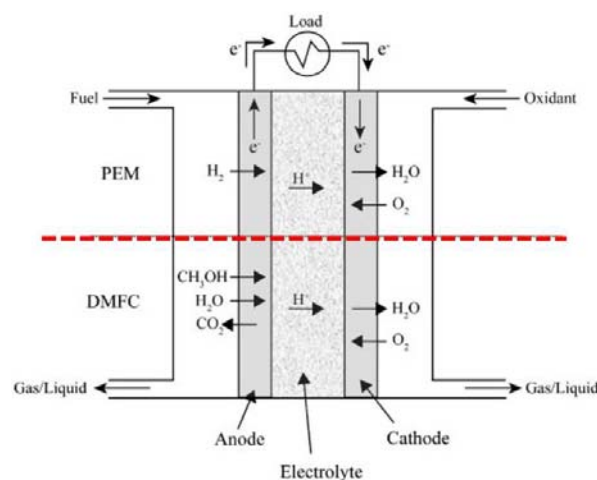


**Figure 20:** Catalytic process of a PEM and DMFC micro-fuel cell shown above and below the red line, respectively [55].

### 2.6.2 Photovoltaic Devices

Photovoltaic (PV) technology is the most promising candidate for power scavenging. PV devices convert solar energy to electrical energy and do not require fuel. The sun is the source of solar energy, and the energy is radiated as photons of light. The photons are electromagnetic particles emitted with various energies and corresponding wavelengths. A breakthrough study in 1954 revealed that silicon p-n junctions absorbed photon energy to create current flow [58]. The photons' energy was higher than the electronic bandgap of silicon, and the absorbed energy generated an electron-hole pair in the doped silicon p-n junction. Electrons travel through the p-type silicon to the contact as a minority carrier, and holes travel in the n-type silicon. The current transportation method is primarily drift (electric field driven) and diffusion (concentration gradient driven). However, the photons' excess energy beyond that of silicon's bandgap energy is wasted as shown in Figure 21.

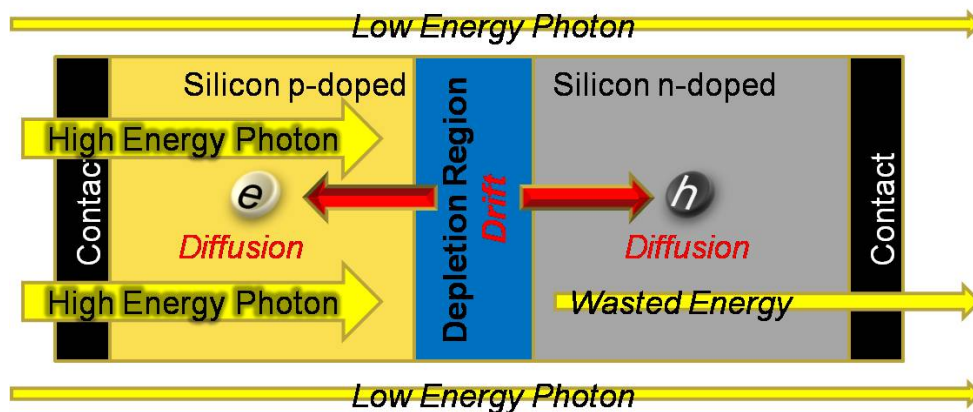


**Figure 21:** Photovoltaic effect shown in doped silicon material. Photon energies greater than the silicon bandgap are absorbed and generate electron-hole pairs. Lower energies are transparent to silicon.



Notable PV cell applications have appeared in recent research. In 1995, Takahisa, *et al* demonstrated 207 V open-circuit voltage using 295 horizontal and vertical stacked cells connected in series. The PV array was 1 cm<sup>2</sup>, and each unit cell was comprised of amorphous silicon [59]. In 2003, Hollar, *et al* demonstrated 90 silicon solar cells connected in series to produce an open-circuit voltage of 50 V, and each cell occupied 150 x 150 μm<sup>2</sup> [16].

Multi-junction solar cells (MJSC) were fabricated for the purpose of collecting more photons and wasting less photon energy. The concept is achieved by stacking direct bandgap materials with varying bandgap energy which decrease top to bottom. Direct bandgap materials are suitable because they possess higher absorption coefficients due to their distinct conduction and valence band structure. In a triple MJSC design shown in Figure 22, the lower two sub-cells absorb photons which are wasted or transparent to the top layer; thus, MJSC designs are more efficient than single layer solar cells. In 2007, Spectrolab fabricated the most efficient MJSC; 40.7% efficiency was achieved using metamorphic GaInP/GaInAs/Ge as the three sub-cells with an open circuit voltage of ~0.4 V [60]. Further, theoretical models predict 50%+ efficiencies with 4-6 sub-cells comprised of nitrogen quaternary compounds such as GaInNAs [61]. Also, the National Renewable Energy Laboratory (NREL) recently demonstrated replacing Ge with GaAs in the GaInP/GaInAs/Ge MJSC increased the open circuit voltage to over 2.95 V (although decreasing to 33.8% efficiency) [62].

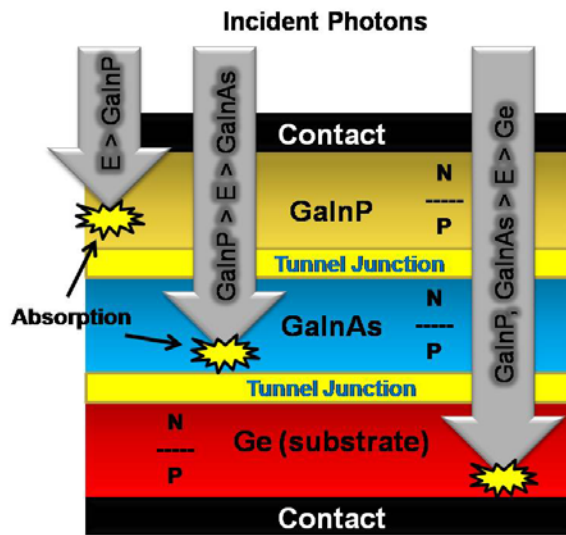


**Figure 22:** Triple junction GaInP/GaInAs/Ge solar cell. More photons are absorbed using stacked direct bandgap materials with decreasing bandgap energies. Tunnel junctions are implemented as a transition material between sub-cells.

An MJSC is the core component of a TPV device. Four components typically form a TPV system—a heat source, an emitter (combustor), a filter and a PV array shown in Figure 23. Heat is generated in a micro-combustor or an emitter by solar radiation, nuclear decay, or onboard fuel such as hydrogen. The emitter, typically made of SiC or similar materials, is suitable for the resultant high temperatures. The broadband emitter irradiates photons on the PV or MJSC array. The PV device absorbs photons greater than the bandgap of the PV array. The low-energy photons are absorbed as wasted thermal energy; thus, increasing device temperature and decreasing quantum efficiency. The filter is integrated to reflect and absorb low energy photons resulting in higher conversion and quantum efficiency. The National University of Singapore reported a hydrogen fueled and filtered GaSb TPV with 2.92 V open circuit voltage, 0.92 W and device area of  $0.113 \text{ cm}^2$  [63]. The University of Queensland Australia reported theoretical TPV

systems comprised of a Co/Ni-doped MgO emitter and GaSb PV array occupying  $2.62 \text{ cm}^2$  with 3.08% efficiency compared to 2.64% efficiency of the PV array alone [54].

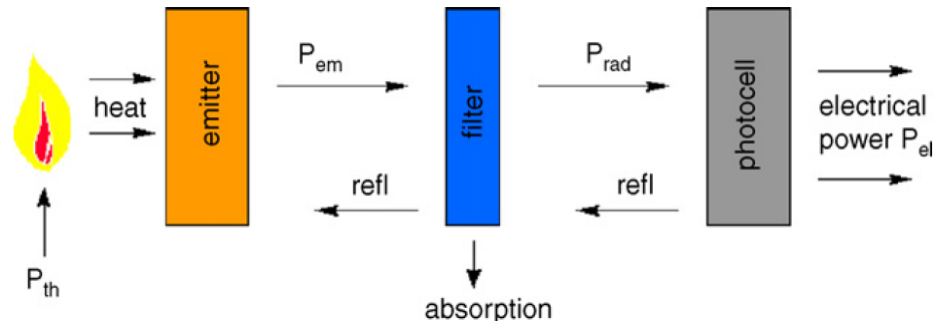


**Figure 23:** Four components of a TPV system are a heat source, an emitter, a filter and a PV array which converts thermal energy to electrical energy. The emitter (combustor) irradiates photons upon the low bandgap PV array. The low-energy photons are recycled back to the emitter which improves the conversion efficiency of the photocell and overall TPV system [54].

## 2.7 Chapter Summary

This chapter presented an overview of miniature and MEMS flying robots including various land-based MEMS robots. Micro-power devices applicable to a wireless flying robot were also discussed. The research of Glauvitz' revealed many successes using comb drive actuators to achieve rotary flight. The addition of a solar cell array capable of 200 V open circuit voltage and area of less than  $1 \text{ cm}^2$  is the most promising candidate for scavenging power. The next chapter explains the necessary theory to analyze the aerodynamics and electro-mechanical aspects of a flying MEMS robot.

## III. Device Theory

### 3.1 Chapter Overview

The purpose of this chapter is to create analytical expressions resulting from the small scaling effects of MEMS devices. Specifically, this chapter delves into low-Reynolds number aerodynamics, general MEMS device theory, scaling effects of friction and electro-mechanical power requirements.

### 3.2 Aerodynamics

An aerodynamics analysis is required to fabricate a MEMS flying robot. Conventional aerodynamics theory is used to predict an object's behavior in a fluidic medium possessing a Reynolds number greater than  $10^5$  [12]. However, as the object size decreases to the insect regime, the aerodynamics relationships break down. This section presents basic aerodynamic theory and current low Reynolds number research to characterize MEMS scale objects.

#### 3.2.1 *Conventional Aerodynamics*

Four primary aerodynamic forces are noteworthy—lift, drag, thrust, and weight. The lift force always counteracts the weight force and acts perpendicular to the aircraft's orientation; when the two forces are equal the aircraft is capable of level flight. The thrust force acts in the direction of flight and is created from the propulsion source. Thrust is generally what differentiates the aerodynamics of fixed-wing versus rotary-wing aircraft which are shown in Figure 24a and Figure 24b, respectively. Each of the four forces is dependent on associated dimensionless coefficients to account for size, shape, and speed factors.

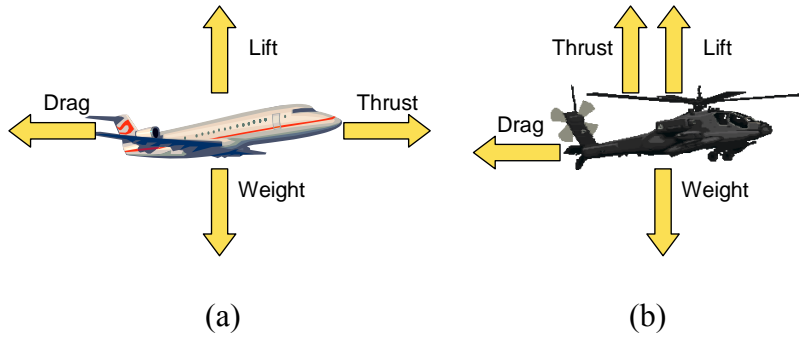


**Figure 24:** Primary aerodynamic forces acting on (a) fixed-wing aircraft in horizontal flight and (b) rotary-wing aircraft in vertical flight.

The aerodynamic lift and drag forces,  $F_L$  and  $F_D$ , are expressed as

$$F_L = \frac{1}{2} C_L \rho U_F^2 S \quad (\text{N}) \quad (1)$$

and

$$F_D = \frac{1}{2} C_D \rho U_F^2 S \quad (\text{N}) \quad (2)$$

where  $C_L$ ,  $C_D$ ,  $\rho$ ,  $U_F$  and  $S$  are the lift coefficient (ratio), drag coefficient (ratio), air density ( $\text{kg/m}^3$ ), flight speed (m/s), and lift surface area ( $\text{m}^2$ ), respectively. Therefore, both forces are extremely small as a flying MEMS robot is beset by its diminutive size and air speed.

An object is capable of sustained level flight if the aerodynamic lift force is equal to its weight. The lift force is obtained using wings with an airfoil cross section. A proper airfoil cross section has a rounded leading edge and a sharp trailing edge. In a simple deflection analysis, the rounded edge deflects the fluid (air) downward, and the force required to do so is equal to lift. In order to achieve lift, the angle the airfoil makes

with the direction of fluid flow must be positive (neglecting camber) referred to as angle of attack. Camber is defined as the bow, or curvature, of the airfoil which typically enhances the lift force. The chord is defined as the length of the airfoil from leading to trailing edge. Figure 25 shows these well-known aerodynamic features.

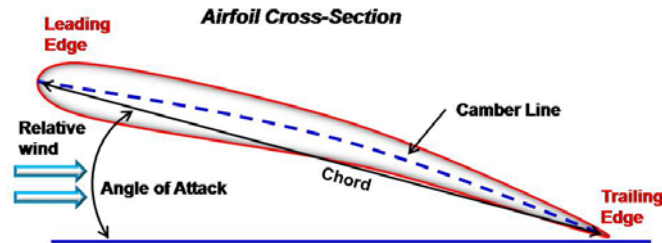


**Figure 25:** Diagram of a conventional airfoil of an aircraft wing.

Bernoulli's principle also characterizes the lift force. The principle states that a pressure differential is created as the oncoming fluid separates above and below the leading edge of the wing. Bernoulli's principle is similar to the ideal gas law with the exception of velocity changes. Because the upper and lower surfaces of the airfoil are not identical, neither is the air velocity above and below the surfaces. Bernoulli showed that a pressure differential is inversely related to velocity [64].

The Reynolds number is used to characterize the flow behavior of a fluid medium. Reynolds number is a dimensionless number which is a ratio of the inertial forces to viscous forces expressed as

$$\text{Re} = \frac{UL_C}{\nu} \quad (3)$$

where  $U$  is the air velocity (m/s),  $L_C$  is the length of the chord (m) and  $\nu$  is the kinematic viscosity of air ( $\text{m}^2/\text{s}$ ).

The Reynolds number classifies a fluid as either laminar or turbulent. For a typical airfoil, laminar flow occurs for Reynolds numbers up to approximately  $10^5$  where the transition to turbulent occurs. Laminar flow is dominated by viscous forces where the flow is smooth and constant. Turbulence transpires when the inertial forces dominate resulting in small, random leading edge vortices (LEV) and chaotic flow motion. LEVs are low-pressure rotations of the fluid velocity which are more pronounced and controlled in laminar flow. In the case of high turbulence (or high Reynolds number), the inertial forces dissipate the vortices; therefore, the LEVs are commonly assumed negligible.

Most flight vehicles operate in high Reynolds numbers because of their considerable size and air speed. According to Figure 26, the Reynolds number varies linearly with air vehicle weight on a logarithmic scale. Figure 26 verifies large aircraft rely on dominating inertial forces to obtain sustainable lift. The opposite is true for MAVs and insects which operate primarily in laminar air flow where drag forces dominate.

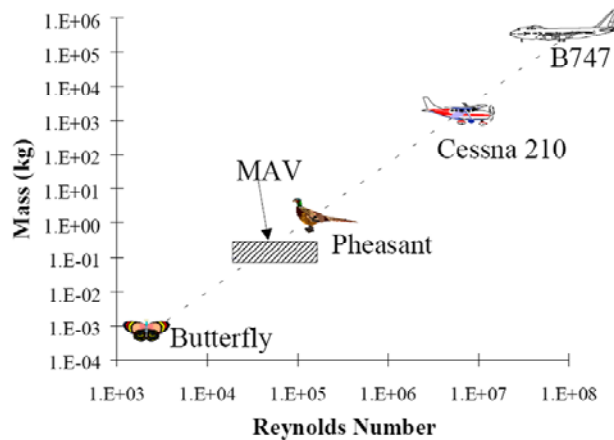


**Figure 26:** Logarithmic plot of air vehicle gross weight versus Reynolds number. Heavy aircraft operate in high Reynolds number ranges [65].

### 3.2.2 *Low-Reynolds Number Aerodynamics*

From the scale of MAVs down to flying MEMS robots, the Reynolds number drastically decreases. Unfortunately, no concrete research exists to explicitly define aerodynamic behavior of insect-size flying robots. Fortunately, enough empirical data and models exist to formulate hypotheses on micro-flight dynamics.

#### 3.2.2.1 *Flapping-Wing Low-Reynolds Number Theory*

A key parameter for macro-scale lift is quasi-steady state flow aerodynamics. Quasi-steady state flow is characteristic of soaring birds and fixed wing aircraft where flapping speed is minimal. The other extreme, unsteady state air flow, is observed mainly with flapping objects. Generally, the transition between the two regimes occurs when the wing flapping speed surpasses the flight speed. MAVs and flying robots operate in the unsteady flow regime because of their low flight speed relative to wing tip speed [66]. The degree of unsteady flow,  $k$ , is dependent on the inverse of flight speed,

$$k \propto \frac{1}{U_F} \quad (4).$$

Clearly, the degree of unsteady flow is higher for a MEMS flying robot and is presented in Figure 27.

Small birds and insects have been closely studied to determine other contributions to their superior aerodynamic efficiency in unsteady state flow regimes. Theory suggests unsteady LEVs have a significant effect on lift. The unsteady LEVs are assumed negligible for large aircraft and some have theorized LEVs are quickly dissipate on small birds and insects [66]. Later, Liu, *et al* confirmed LEVs were prevalent on a MAV wing



using 3-D computational fluid dynamic (CFD) analyses [67]. The study pointed out LEVs were preserved by spanwise flow, or flow in the dimension of the wing's length [66, 67]. In steady state flow, the LEV is quickly shed along the length of the wing; hence, the reason for simpler 2-D models. However, in unsteady state conditions, spanwise flow conserves the low-pressure LEV above the wing accounting for the pressure-gradient lift phenomena [68].

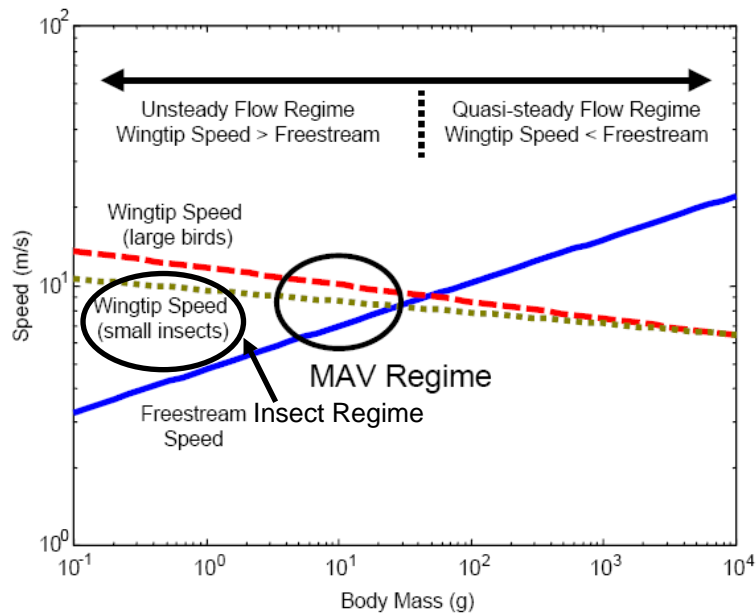


**Figure 27:** Air speed vs. air vehicle mass showing the approximate division of the two flow regimes [66].

Insect flight studies have identified the influences of various forces at low Reynolds numbers. Quasi-steady state flow flyers use lift to their advantage. However, when  $Re < 1000$ , insects (and a flying MEMS robot) experience larger drag forces in unsteady state flow, and the lift forces are negligible [42, 43, 69]. Kawachi, *et al* defined

appropriate locomotion methods for various Reynolds Number ranges as depicted in Figure 28.

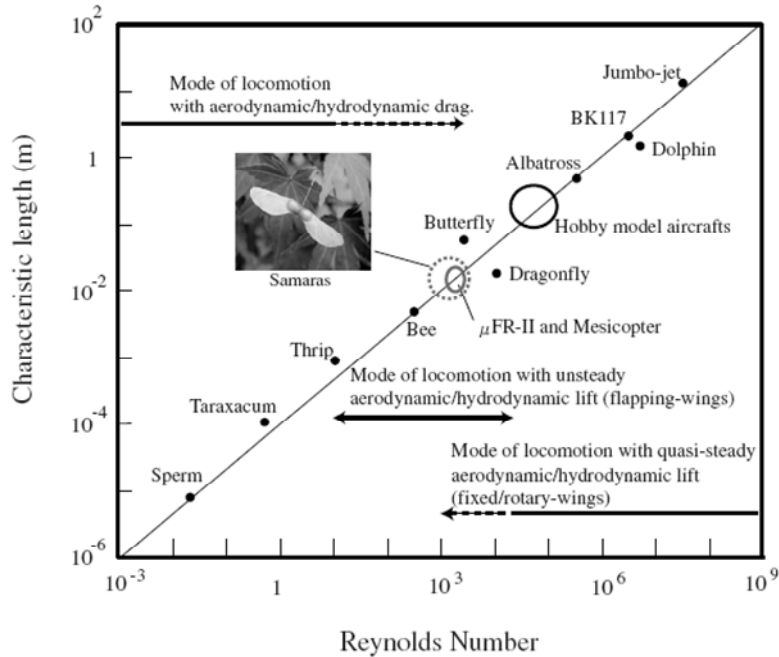


**Figure 28:** Characteristic length of flyer versus Reynolds number defining various ranges of locomotion methods [70].

Figure 28 shows devices operating with  $Re < 1000$  are suited for flapping flyers, and the lower limit for a rotary-wing flyer was  $Re = 1000$  relying on lift [70]. The research of Tsuzuki, *et al* pointed out a rotary-wing device is feasible in the range of  $Re = 1000$  after observing that maple tree “seed helicopters” rotate as they fall from limbs in this range [69, 71]. The Reynolds number of a rotary-wing MEMS robot falls in the range of  $10^1$ - $10^2$ . However, further research and experiments are required to validate that a rotary-wing MEMS robot is possible.

### 3.2.2.1 Rotary-Wing Theory

Rotary wings create lift identically to that of fixed wings. The major difference is the thrust force is vertical as opposed to horizontal for fixed wing (for level flight) as shown in Figure 24. The phenomenon of a LEV exists to enhance rotary-wing lift capabilities since the lift principle is the same. The LEV boost is thought to increase the allowable weight than that calculated using conventional aerodynamics [69]. To compare rotor performances, the figure of merit (FOM) as described by Tsuzuki, *et al* is expressed as

$$FOM_{rotor} = \frac{C_T}{C_Q} \sqrt{\frac{C_T}{2}} \quad (5)$$

where  $C_T$  and  $C_Q$  are the thrust (lift) and torque coefficients (ratios), respectively. Analyzing Equation 5, it is clear an increase in thrust coefficient improves rotor performance. The torque coefficient is not covered here in detail, but it increases linearly with the thrust coefficient; therefore the  $C_T / C_Q$  term remains fairly constant.

Additional aerodynamic analysis for rotary wings was conducted by Miki, *et al*. In particular, Miki developed an equation to calculate thrust force based on lift and drag coefficients. The thrust force,  $F_T$ , is given as

$$F_T = \frac{2}{3} \pi^2 \rho b L_c \Omega^2 R^3 (C_L + \varphi C_D) \quad (\text{N}) \quad (6)$$

where  $b$  is the number of rotor blades,  $\Omega$  is the frequency of rotation (Hz),  $R$  is the wing radius (m),  $\varphi$  is the induced angle (rad) and  $C_D$  is the drag coefficient (ratio) [45-49]. The unknown parameter of Equation 6 is  $(C_L + \varphi C_D)$ , or  $C_{rw}$ . This parameter was measured for

wing lengths 1.5 mm – 8 mm and increased as the length decreased to 2.5 mm; thereafter, the parameter showed instability. The instability was most likely attributed to vibration sensitivity or from a higher degree of unsteady air flow. The measurements were also lower when the wings were attached to the rotor shaft, especially for shorter wing lengths. For example, a 2.5 mm wing coefficient was measured at 2 but dropped to 0.74 after attachment. According to Figure 29, a MEMS flying robot with wings 1-2 mm long is presumed to have a coefficient of 2, but could vary as low as 0.5-1.0 accounting for the experimental vibration in Miki's setup. The discontinuity shown in Figure 29 at R=3 mm could also be a sign of the transition to unsteady-state aerodynamics.

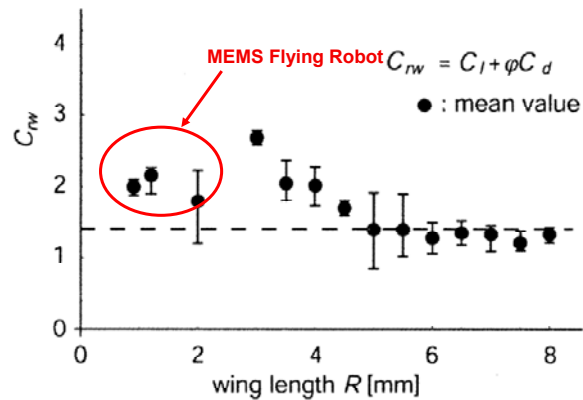


**Figure 29:** Miki's measurement of the unknown aerodynamic coefficient in order to calculate thrust force [49].

In order to achieve lift, the sum of the lift and thrust force must be greater than the weight force of the MEMS robot. Literature suggests the drag forces dominate, and the lift force due to LEVs is much smaller than the thrust force; therefore, lift force can be assumed negligible at Reynolds Numbers below 1000 as verified in Figure 28 [11, 69]. With this assumption, the required thrust force for flight is expressed as

$$F_T \geq mg \quad (7)$$

where  $m$  and  $g$  are the mass of the robot and acceleration due to gravity ( $9.81 \text{ m/s}^2$ ). Inserting Miki's expression for thrust force into Equation 7 and solving for rotor frequency, the rotor frequency required for lift,  $\Omega_L$ , can be expressed as

$$\Omega_L \geq \sqrt{\frac{mg}{\frac{2}{3}\pi^2 \rho b L_C R^3 C_{rw}}} \quad (\text{Hz}) \quad (8).$$

### 3.2.3 Bio-inspired Wing Design

A flying MEMS robot should mimic the wing of small, flying insects. Over a million different species of insects and 10,000 types of birds and bats exist which utilize their wings for locomotion [72]. Conventionally, the Blade Element Theory (BET) is used when designing a wing when the flow regime is steady-state (high Reynolds number). Because the flow is unsteady, the BET technique is inaccurate and frequently underestimates the thrust force in rotary blades [73, 74]. Again, the reason is due to the unsteady LEVs which provide additional thrust and lift unaccounted for using conventional aerodynamics. Thus, any guidelines for accurate wing design are based purely from empirical data.

Tsuzuki, *et al* presents excellent guidelines for designing a rotary-wing blade on the premise of increasing the rotary wing figure of merit ( $FOM_{rotor}$ ). Experiments showed the optimum pitch angle, the angle of wing deflection, is  $15\text{-}20^\circ$  for unsteady flow of  $Re = 4000$  compared to Miki's  $45^\circ$  flap. The aspect ratio (AR), the ratio of wing's length to chord, was optimum for 5.5 shown in Figure 30a. The surface

roughness (corrugation) was found to make the wing rigid against bending and torsional deformations [73, 75]. Additional optimal geometric findings from Tsuzuki's research are summarized in Table 6. For all findings, a wing cross section of a flat plate increased the rotary  $FOM_{rotor}$ . To corroborate these results, a cross section of an actual dragonfly wing is shown in Figure 30b producing these experimental results [69, 76].

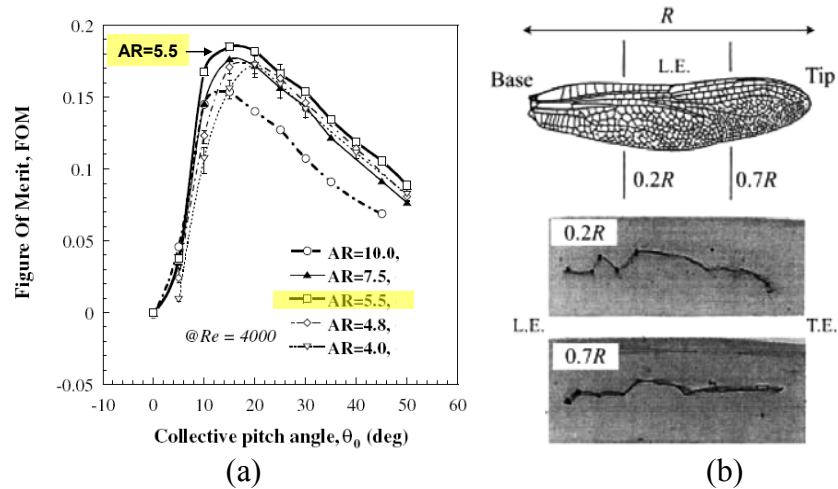


**Figure 30:** (a) The FOM of a rotary-wing blade is maximum for pitch angle range of 15-20°, and (b) the dragonfly cross section mimics Tsuzuki's optimal geometric design guidelines [69, 76].

**Table 6:** Rotary-wing design guidelines for increasing FOM [69].

1. Flat-plate overall wing shape
2. Pitch angle of 15-20°
3. Aspect ratio of 5.5
4. Thickness-to-chord ratio of 2%
5. Leading edge cut of 45°
6. Camber-to-chord ratio of 10%
7. Max camber occurring at chord midpoint
8. Gentle leading edge corrugation of 15°
9. Small projection offset approx 15% from leading edge
10. Surface roughness across trailing edge

### 3.3 PolyMUMPs™ Process

The Polysilicon Multi-User MEMS Processes™ (PolyMUMPs™ or MUMPs®) is utilized by AFIT to fabricate conceptual MEMS devices. The MUMPs® process is a three layer polysilicon surface micromachining process. Surface micromachining is an additive process; beginning with the substrate, thin films are deposited on top of the substrate and lithographically patterned and etched to form features. Structural layers are separated by sacrificial layers which are removed at the end of the fabrication process to enable device movement [77]. In the MUMPs® process, the structural layer is polysilicon, and the sacrificial layer is silicon dioxide, or oxide. An important feature of the MUMPs® process is each layer's topology is conformal with respect to the underlying layer. For example, a recessed feature in one polysilicon layer will be duplicated in the layer above it—similar to how a blanket conforms to the topology of the surface that is covered.

The MUMPs® process begins with a phosphorus-doped silicon dioxide (PSG) layer to dope the silicon substrate of <100> crystal orientation. A 0.6 μm silicon nitride layer is deposited in a low-pressure chemical vapor deposition process (LPCVD). The nitride layer serves as an excellent dielectric and electrical isolation layer. A 0.5 μm layer of polysilicon (Poly0) is deposited next using LPCVD. The Poly0 layer is patterned and etched via a Reactive Ion Etch (RIE) according to the Poly0 mask level drawn in L-Edit software.

Continuing, a 2 μm PSG layer (Oxide1) is deposited via LPCVD to define the first sacrificial layer. Dimples are implemented next to prevent stiction—the act of

MEMS devices unexpectedly bonding together. Dimples are small protrusions which are used to reduce the amount of contact surface area. The dimples are created via a timed RIE.

The first structural layer, Poly1, is 2  $\mu\text{m}$  thick and LPCVD-deposited above the remaining Oxide1. Poly1 is not deposited completely flat; rather, the Poly1 follows the topology of the Poly0, dimple and Oxide1 features. An additional PSG layer is deposited onto Poly1 and annealed at 1050° C to dope the layer which reduces its internal stress and increases its conductivity [78]. The process is repeated for Poly2 and Oxide2 with an option of joining the two polysilicon layers using a Via etch.

Gold is deposited directly to the Poly2 topology in a metal evaporation process. Metal evaporation is conducive for patterning the gold layer because it produces no side walls on recessed features. Without side walls, the unwanted gold is removed using metal-lift off. Metal lift-off is performed in the MUMPs<sup>®</sup> process by rinsing the wafer in acetone. Figure 31 shows a comprehensive diagram integrating all MUMPs<sup>®</sup> design features.

The last step of the MUMPs<sup>®</sup> process is releasing the sacrificial oxide. The chips are submerged in 48% Hydrofluoric Acid (HF) to etch away the two sacrificial oxide layers. Figure 31 shows an unreleased device; however, a released version would simply have oxide layers removed. For more information, refer to the *PolyMUMPs<sup>TM</sup> Design Handbook* [78].



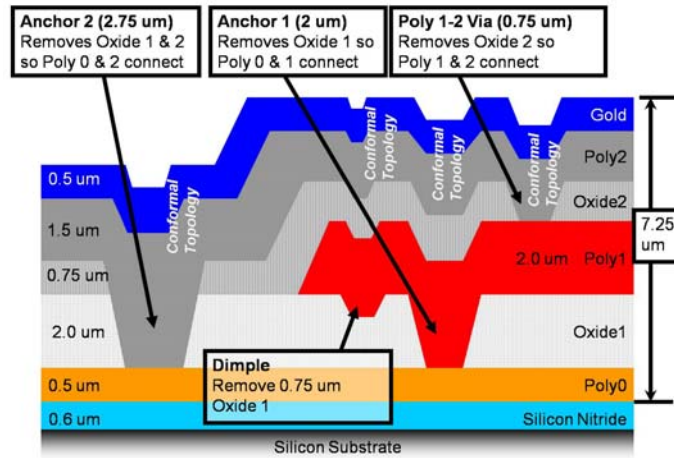


**Figure 31:** Comprehensive figure showing thin-film deposition layers of the PolyMUMPs<sup>®</sup> process. Oxide etch features are also shown with resulting conformal topology.

### 3.4 Thin-film Residual Stress

Residual stress is a byproduct of the MUMPs<sup>®</sup> process often resulting in material deformation. Residual stress can be advantageous in applications such as an actuation method, self-assembly—or in this case, wing deflection. Residual stress obtained from MUMPs<sup>®</sup> is a direct result of different thermal depositions and internal dopant gradients within the materials. MUMPs<sup>®</sup> is a defined process which deposits two releasable layers of structural polysilicon and one layer of gold. The material properties of the three layers are given in Table 7.

After each of the polysilicon layers are deposited, a very thin 200 nm layer of PSG is applied. The phosphorus atoms of the PSG layer diffuse into the polysilicon during a 1050° C annealing process [78]. During this process the undoped polysilicon becomes n-

type doped, or donor type, due to the increase of electrons “donated” to the conduction band. The dopant reduces its electrical resistance,  $R_E$ , expressed as

$$R_E = \frac{\rho_E L_E}{A_E} \quad (\Omega) \quad (9)$$

where  $\rho_E$ ,  $L_E$  and  $A_E$  are the electrical resistivity ( $\Omega\cdot\text{m}$ ), electrical path length (m) and electrical path cross section ( $\text{m}^2$ ) of the doped polysilicon, respectively.

**Table 7:** Typical PolyMUMPs™ layer material properties. The symbols C and T denote compressive and tensile residual stress, respectively [78-80].

<i>Variable</i>	<i>Poly1</i>	<i>Poly2</i>	<i>Gold</i>
Young’s Modulus (GPa)	131	162	78
Poisson’s Ratio	0.22	0.22	0.44
Coefficient of Thermal Expansion ( $\text{K}^{-1}$ )	2.3 E-06	2.3 E-06	14.3 E-06
Layer Thickness ( $\mu\text{m}$ )	2	1.5	0.5
Typical Residual Stress (MPa)	5 C	7 C	13 T

Residual stress gradients are classified as either tensile or compressive and vary in the axis perpendicular to the substrate. Polysilicon is typically compressive due to the techniques used to grow its crystalline structure. Contrary to pure silicon’s repeated crystal lattice structure, polysilicon is a repeated lattice structure contained within varying grain boundaries. The grain boundaries during the initial 200 nm of growth are under significant compressive stress; thereafter, the stress decreases. Therefore, thinner layers of polysilicon are prone to increased levels of residual stress. Notable causes of residual stress are a result of interstitial dopant or oxygen atoms at the layer interface [81]. Figure 32 shows how the grain boundary formations vary vertically during poly-crystalline growth.

The phosphorus atoms diffuse from the top surface into the material leaving behind a non-uniform dopant distribution. Each dopant atom disrupts the crystalline polysilicon lattice creating internal stress. The amount of internal stress decreases in the vertical direction for each polysilicon layer yielding a stress gradient. Studies have shown phosphorus dopant in polysilicon shifts the internal residual stress more compressive. However, depending on the temperature of deposition and annealing, phosphorus can enhance the stress relief during the anneal [82].

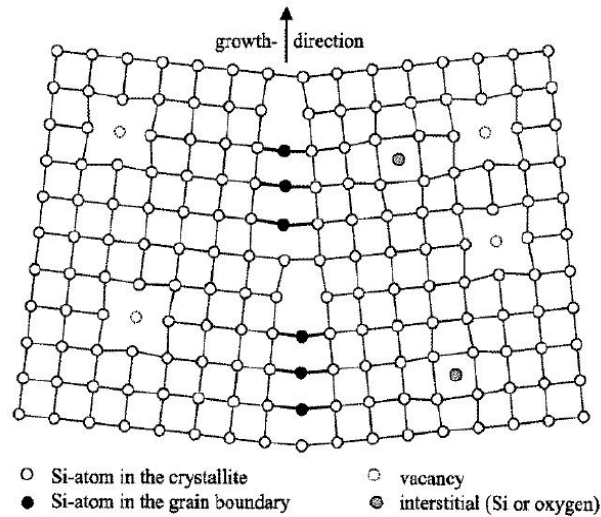


**Figure 32:** Poly-crystalline growth process varies in the vertical direction due to grain boundary and lattice defects [83].

The annealing process is another integral element of residual stress. As part of the dopant diffusion step, the material is heated several times to 1050°C in the MUMPs<sup>®</sup> process. The anneal serves to reduce residual stress, dope the polysilicon layer, allow the dopant and polysilicon atoms to rearrange themselves, and reduce crystal defects [84]. However, the annealing is a source of thermal stress, a component of overall residual stress. Thermal stress is a result of a temperature gradient formed during the deposition

of the material layers which cools to room temperature after the deposition and annealing is complete.

Thermal residual stress is critical when two dissimilar materials are stacked; in the MUMPs<sup>®</sup> process, polysilicon and gold. The two materials have drastically different coefficients of thermal expansion (CTE). Table 7 shows gold has a higher CTE than polysilicon, and following the gold deposition, the layers are cooled to room temperature where tensile stresses develop in the gold layer from the expansion difference. When the device is released in HF, the stress in the gold is relieved by curling the Poly2/Gold layer upward out-of-plane.

Two components of thin-film stress were discussed—internal residual stress and thermal stress. These two components when added together form the total residual stress of a single layer,  $\sigma_{layer}$ , which is expressed as

$$\sigma_{layer} = \frac{E'_p t_p}{2R_{layer}} \quad (\text{Pa}) \quad (10)$$

where  $E'_p$ ,  $t_p$  and  $R_{layer}$  are the biaxial modulus of elasticity for polysilicon (Pa), polysilicon layer thickness (m) and radius of curvature (m), respectively. The biaxial modulus of elasticity and radius of curvature are defined as

$$E'_p = \frac{E_p}{1-\nu_p} \quad (\text{Pa}) \quad (11)$$

and

$$R_{layer} = \frac{E_p I_x}{M} \quad (\text{m}) \quad (12)$$

where  $E_P$ ,  $\nu_P$ ,  $I_x$  and  $M$  are Young's Modulus (GPa) of polysilicon, Poisson's Ratio of polysilicon, x-axis area moment of inertia ( $m^4$ ) and bending moment (N-m) of the layer. For a bilayer structure of polysilicon and gold, the stress components add distinctly as

$$\sigma_{bilayer} = \sigma_{internal} + \sigma_{thermal} \quad (\text{Pa}) \quad (13)$$

where  $\sigma_{thermal}$  is given as

$$\sigma_{thermal} = E'_G (\alpha_G - \alpha_P) (T - T_0) \quad (\text{Pa}) \quad (14)$$

where  $\alpha_{G,P}$  is the CTE of gold and polysilicon ( $K^{-1}$ ),  $E'_G$  is the biaxial modulus of elasticity of gold,  $T$  is the fabrication temperature (K) and  $T_0$  is the post-process temperature (K). Values of  $\sigma_{internal}$  are typically found on the MUMPs<sup>®</sup> website and are published for every run. In a similar manner as Equation 10 was written, residual stress of a Poly2-Gold cantilever,  $\sigma_{bilayer}$ , is expressed as

$$\sigma_{bilayer} = \frac{E'_P t_P^2}{6 t_G R_{bilayer}} \quad (\text{Pa}) \quad (15)$$

where  $t_G$  is the thicknesses (m) of gold, and  $R_{bilayer}$  is the radius of curvature of a bilayer Poly2-Gold cantilever (m) given as [20]

$$R_{bilayer} = \frac{E'_G (t_P + t_G)^2}{6 t_P t_G \sigma_{thermal}} \quad (\text{m}) \quad (16).$$

Equation 15 is known as Stoney's equation which relates deflection and residual stress components. The overall vertical deflection for a thin beam of polysilicon and a bilayer Poly2-Gold beam is

$$v_{layer} = \frac{\sigma_{layer} L^2}{E_p t_p} \quad (m) \quad (17)$$

and

$$v_{bilayer} = \frac{\sigma_{bilayer} 3t_G L^2}{E_p t_p^2} \quad (m) \quad (18)$$

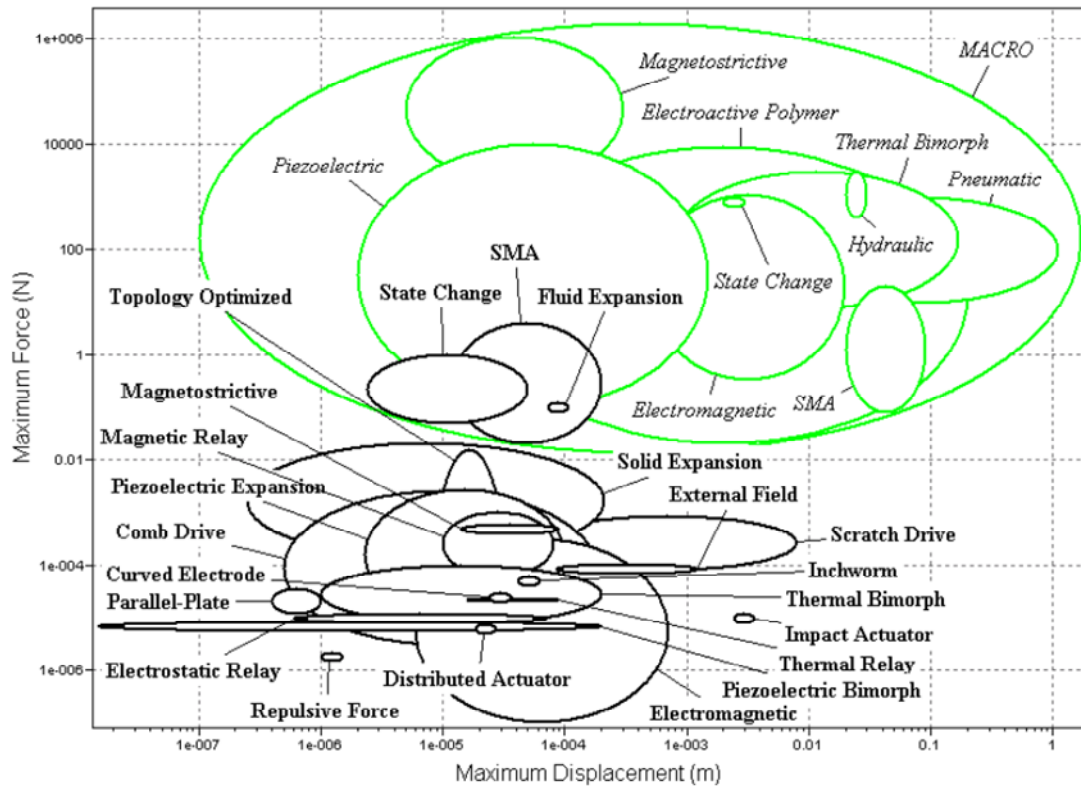
where  $v$  and  $L$  are the deflection and length (m) of the beam, respectively.

### 3.5 Drive Actuator

An actuation method is required to drive a MEMS robot's wings at a frequency capable of a thrust force at least equal to the robot's weight. Because the robot will employ rotary style wings, the actuation method must also be capable of rotary actuation. Other requirements include increasing the force, displacement and frequency of the actuator. In reality, all three of these requirements have engineering trade-offs as discussed below.

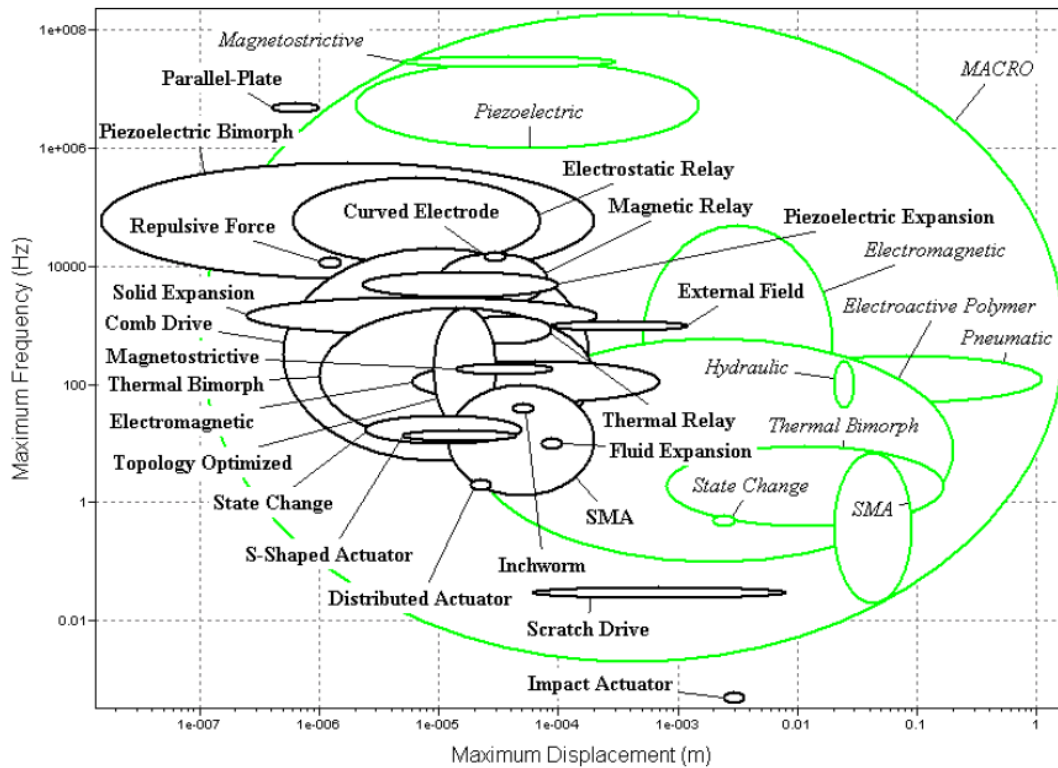
#### 3.5.1 Survey of Actuators

Figure 33 shows available MEMS actuators and their respective force versus displacement limitations. The bold, black lines represent MEMS-scale actuators. From Figure 33 it is clear the comb drive and solid expansion (including thermal actuators), both capable of MUMPs<sup>®</sup> fabrication, possess similar displacements. However, the comb drive is limited by an order of magnitude lower force ( $\sim 0.1$  mN) than solid expansion ( $\sim 1$  mN).



**Figure 33:** Maximum displacement versus maximum force for common MEMS actuators [85]. The black and green lines refer to MEMS and macro-sized actuators, respectively.

Figure 34 shows available MEMS actuators and their respective frequency versus displacement limitations. Again, the bold, black lines represent MEMS scale actuators. Figure 34 shows the comb drive actuator can be designed for a wide variety of frequencies from 10 Hz to 50 kHz; whereas, the solid (thermal) expansion operates under a narrow band of frequencies of about 500 Hz to 5 kHz. These results verify that electrostatics trade off force for increased frequency performance.



**Figure 34:** Maximum displacement versus maximum frequency for common MEMS actuators [85]. The black and green lines refer to MEMS and macro-sized actuators, respectively.

Figure 35 shows an example of a solid expansion actuator utilizing thermal expansion. A current source is applied across the anchors which cause the arms to expand via Joule heating. The hot arm generates more heat than the cold arm because the cross sectional area is smaller. As a result, the hot arm expands farther with the resulting deflection toward the cold arm. The frequency response is limited to how quickly the hot arm cools between pulses. Hickey, *et al* researched MUMPs<sup>®</sup> fabricated thermal actuators, and their empirical data shows a cutoff frequency range of 1–2.6 kHz in the configuration shown in Figure 35 [86]. This frequency range could be useful if large



gear ratios were used, but to minimize mass and parts thermal actuators are ruled out for application of a flying MEMS robot.

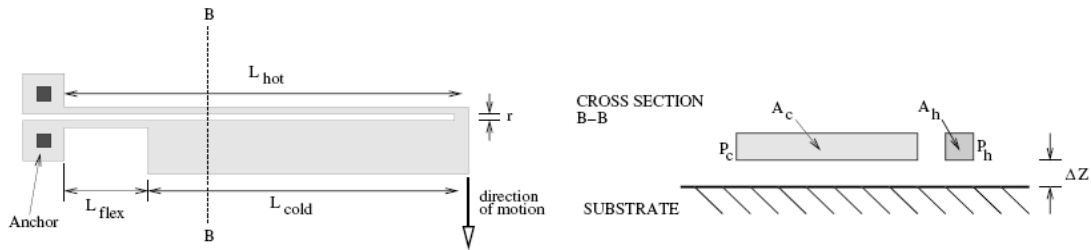


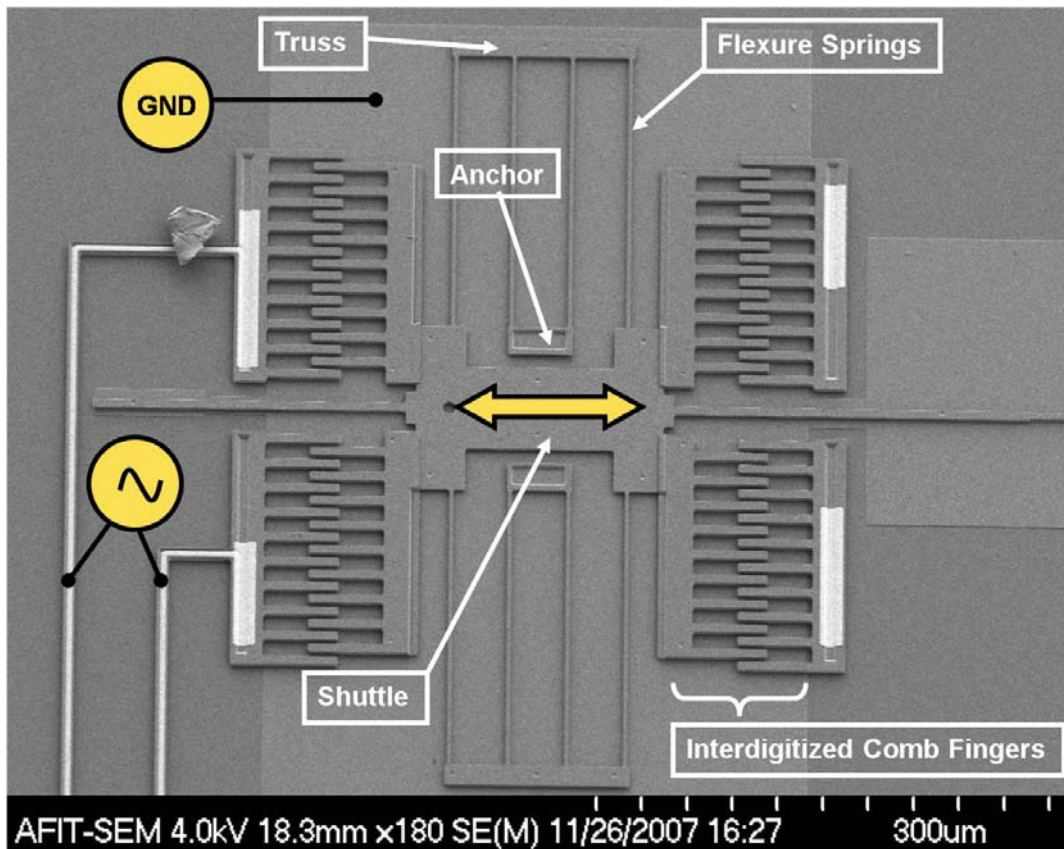
**Figure 35:** Thermal (solid expansion) actuator diagram. The hot arm expands more than the cold arm pushing actuator in the direction of the cold arm as depicted [86].

### 3.5.2 Comb Drive Resonators

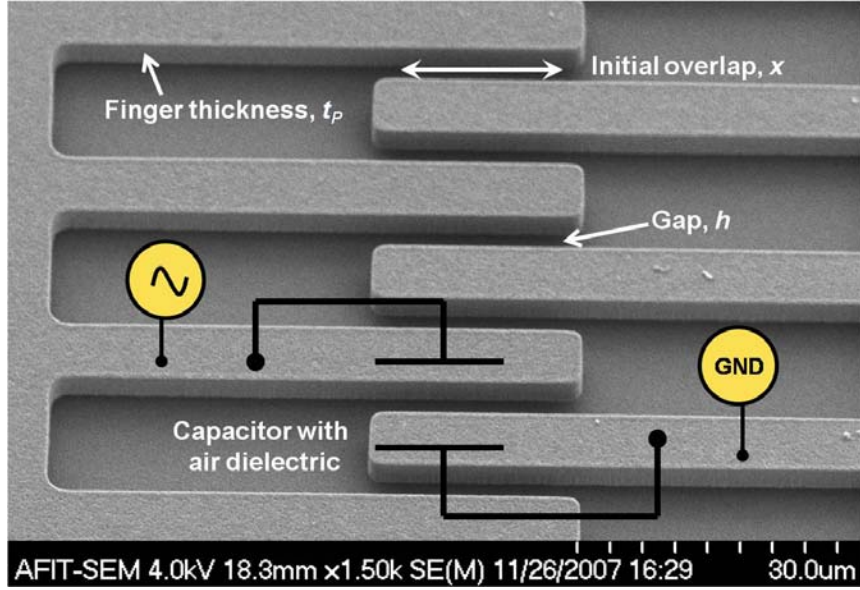
Comb drive resonators offer several advantages over thermal actuators such that numerous aspects of the resonator are easily controlled. First, the capacitive nature of electrostatic MEMS scales down very well. For example, the small gap formed between the comb fingers (few micrometers) is on the order of the mean free path of air molecules. The small gap increases the breakdown electric field, and the MEMS comb drive is capable of handling high voltage (although a disadvantage from a power-scavenging view) [87]. Another advantage is the designer has a multitude of geometric considerations for various applications as shown by the large circle in Figure 34.

Figure 36 shows a scanning electron microscope (SEM) picture of the basic components of a comb drive. The outer comb fingers are fixed to the substrate with either end at an applied voltage potential. The inner fingers are attached to a shuttle-truss system which is connected to ground potential. The upper and lower trusses both contain two sets of folded spring flexures. The folded springs largely suppress the residual stress

inherent in the MUMPs<sup>®</sup> process [88]. The shuttle is free to move laterally forming a spring-mass-damper system. Therefore, the inner comb fingers move in a back-and-forth motion when the system is in resonance. The resonance frequency occurs when the applied voltage sine wave matches the natural frequency of the spring and mass mechanical system. The interdigitized fingers remain parallel to one another forming a parallel-plate capacitance with air as the dielectric medium as shown in Figure 37.



**Figure 36:** SEM picture of a comb drive showing basic components and electrical configuration.



**Figure 37:** SEM picture of interdigitized comb fingers and the electrical capacitance formed between each pair.

The actuation cycle begins when the outer comb fingers have an applied voltage potential at the system's resonance frequency. The interdigitized comb fingers are oppositely charged forming capacitors on either side of the inner comb fingers. The capacitors store energy on each side of the finger (one side is illustrated in Figure 37), and the total stored electrical energy,  $W_E$ , is expressed as

$$W_E = n(W_{E1} + W_{E2}) \quad (\text{J}) \quad (19)$$

where  $W_{E1}$  and  $W_{E2}$  are the stored energies to the left and right of each finger (J), and  $n$  is the number of comb finger pairs. The expression for electrical energy (J) is expressed as

$$W_{E1} = W_{E2} = \frac{CV^2}{2} \quad (\text{J}) \quad (20)$$

where  $C$  and  $V$  are the electrical capacitance (F) and applied voltage (V) for each finger pair, respectively. Each capacitor is modeled as a conventional parallel plate device with air as the dielectric. The electrical capacitance,  $C$ , is expressed as

$$C = \frac{\varepsilon_0 \varepsilon_{air} t_p x}{h} \quad (\text{F}) \quad (21)$$

where  $\varepsilon_0$ ,  $\varepsilon_{air}$ ,  $t_p$ ,  $x$  and  $h$  are the permittivity of free space (F/m), permittivity of air (unitless), thickness of comb finger (m), finger overlap (m) and gap between fingers (m), respectively. Substituting Equation 20 and 21 into Equation 19, the stored energy is rewritten as

$$W_E = n \left( \frac{CV^2}{2} + \frac{CV^2}{2} \right) = n \left( \frac{\varepsilon_0 \varepsilon_{air} t_p x}{h} \right) V^2 \quad (\text{J}) \quad (22)$$

The potential difference induces an electrostatic force,  $F_E$ , calculated by taking the first derivative of the energy stored in the capacitor,  $W_E$ , with respect to  $x$ , is given as

$$F_E = \frac{dW_E}{dx} = n \left( \frac{\varepsilon_0 \varepsilon_{air} t_p}{h} \right) V^2 \quad (\text{N}) \quad (23).$$

The electrostatic force pushes the shuttle and inner comb fingers away from the voltage source. The flexures attached to the shuttle absorb the electrical energy from the capacitor and store it as mechanical energy. The mechanical spring energy,  $W_S$ , and spring force,  $F_S$ , are defined according to Hooke's Law as

$$W_S = \frac{k_S d_x^2}{2} \quad (\text{J}) \quad (24)$$

$$F_S = \frac{dW_S}{dd_x} = k_S d_x \quad (\text{N}) \quad (25)$$

where  $k_S$  and  $d_x$  are the system spring constant (N/m) and lateral spring displacement (m), respectively.

The spring design of the comb drive was discussed as a top and bottom truss each with two sets of folded springs. Each folded spring is modeled in Figure 38, and the spring constant (N/m) for one set of folded springs,  $k_{fold}$  is given as

$$k_{fold} = \frac{6E_P I_Z}{L_S^3} \quad (\text{N/m}) \quad (26)$$

where  $I_Z$  and  $L_S$  are the z-axis area moment of inertia ( $\text{m}^4$ ) and spring length (m), respectively. Spring constants combine exactly as electronic capacitors; parallel springs are simply added. The comb drive's four sets of folded springs act in parallel, and the total system spring constant is given as

$$k_S = \frac{24E_P I_Z}{L_S^3} \quad (\text{N/m}) \quad (27)$$

where

$$I_Z = \frac{w^3 t}{12} \quad (\text{m}^4) \quad (28)$$

and  $w$  (m) and  $t$  (m) are the width and thickness of the spring, respectively.

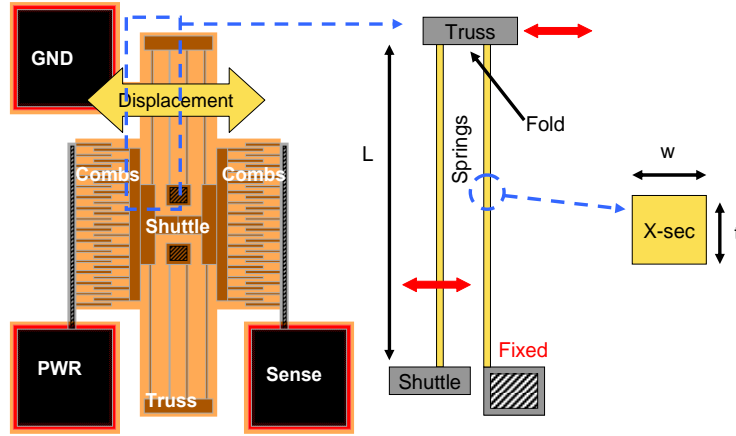


**Figure 38:** Folded spring design diagram for an electrostatic comb drive allowing left-to-right actuation at resonance.

There exists a balance of energy between the electrical capacitors and mechanical springs. Assuming no energy loss, the electrostatic and spring forces are equal at the midpoint of oscillation. Given this, the displacement of the shuttle in each direction,  $d_x$ , can be solved for in terms of applied voltage and given material properties. Setting Equations 22 and 24 equal to each other and solving for  $d_x$ , we arrive at

$$d_x = n \left( \frac{\epsilon_0 \epsilon_{air} t_P}{h} \right) V^2 \left( \frac{1}{k_S} \right) = n \left( \frac{\epsilon_0 \epsilon_{air} t_P L_S^3}{24 h E_p I_Z} \right) V^2 \quad (m) \quad (29).$$

Equation 29 defines the distance of the shuttle from the center to either end. However, it should be noted that twice this distance is available for actuation, or

$$d_{pp} = n \left( \frac{\epsilon_0 \epsilon_{air} t_P L_S^3}{12 h E_p I_Z} \right) V^2 \quad (m) \quad (30).$$

Actuation is deficient unless the applied voltage sine wave and the mechanical comb drive frequencies are in resonance. The frequency of the sine wave is easily

adjusted using an electronic waveform generator. The natural frequency of the comb drive is calculated by modeling the system as an oscillating mass and spring—the spring being the long flexures attached to the trusses and the mass incorporating the truss, shuttle (and inner combs) and flexures. In general, the natural frequency,  $f$  (Hz), of any mechanical oscillator is shown as

$$f = \frac{1}{2\pi} \sqrt{\frac{k^*}{m^*}} \quad (\text{Hz}) \quad (31),$$

and  $k^*$  and  $m^*$  are the spring constant and mass of the oscillating system, respectively. The system spring constant of the comb drive was calculated in Equation 27, and the mass is the sum of the shuttle and fingers,  $m_S$  (kg), the flexures,  $m_F$  (kg), and folded trusses,  $m_T$  (kg). In 1989, Tang, *et al* formulated an expression for the mass term based on empirical data [88]. Incorporating Tang’s findings, the expression for the natural frequency of the comb drive,  $f_{comb}$ , is given as

$$f_{comb} = \frac{1}{2\pi} \sqrt{\frac{k_S}{m_S + \frac{1}{4}m_T + \frac{12}{35}m_F}} \quad (\text{Hz}) \quad (32).$$

### 3.6 Statics and Dynamics

A circular actuation scheme is required to turn a set of rotary-wing blades. Gears, a fundamental MEMS component, are ideal to spin rotary-wings at the required lift frequency. Two gears of different sizes, a master and pinion, are related by gear ratios assuming intermeshing gear teeth. The pinion gear is the MEMS actuating system, and the master gear is the larger gear attached to the rotary wings. Assuming the master gear

is rotating at a sufficient lift frequency,  $\Omega_L$ , the required pinion gear drive frequency,  $f_P$ , is expressed using the gear ratio,

$$G = \frac{f_P}{\Omega_L} = \frac{N_P}{N_M} \Rightarrow f_P = G\Omega_L \quad (\text{Hz}) \quad (33),$$

where  $G$ ,  $N_P$  and  $N_M$  are the gear ratio, pinion gear number of teeth and master gear number of teeth, respectively.

As the comb drive actuates, friction forces due to polysilicon-to-polysilicon surface rubbing of the actuator and gear occur. In macro-size devices, the force of friction is independent of surface area. However, due to the MEMS scaling effect, the surface area-to-volume ratio significantly increases. At the MEMS regime, surface roughness and surface area play a major role in determining the friction force [89]. The conventional expression for friction force,  $F_F$ , is

$$F_F = \mu_S mg \quad (\text{N}) \quad (34)$$

and  $\mu_S$  is the dimensionless coefficient of static friction. This force expression represents the force required to move an object from rest. Technically, once the device is in motion, the frictional force is decreased because the static friction coefficient is replaced with the kinetic friction coefficient which is typically less. However, due to the micro-scaling uncertainty and to remain conservative, the static friction force will be used throughout.

Lumbantobing, *et al* researched the friction force of polysilicon-to-polysilicon using MUMPs<sup>®</sup> fabricated comb resonators [89]. The frictional force was a result of polysilicon MUMPs<sup>®</sup> dimple features rubbing against the polysilicon electrode. Dimples



are small protrusions allowing for minimal surface area contact. Lumbantobing's empirical results modified Equation 33 as

$$F_F = K \left( \frac{mg}{A_C} \right)^{B-1} mg \quad (\text{N}) \quad (35)$$

where  $K$  and  $B$  were found to be 134.1 and 0.610, respectively, and  $A_C$  is the contact area of the dimples ( $\text{m}^2$ ) [89]. The empirical results were recorded using ten dimples varying 25-100  $\mu\text{m}^2$ . Although these findings were associated with a comb drive, the same analysis will be applied for friction forces of the gear-substrate interface as well.

### 3.7 Electromechanical System Theory

The comb drive actuator is a transducer which converts electrical energy to mechanical energy; hence, a coupled electromechanical resonating system. The electromechanical system can be simplified into an inductor-resistor-capacitor (LRC) circuit with electromechanical couplings as shown in Figure 39. The LRC components represent the spring-mass-damper, and the transformer represents the coupling from the electrical capacitance to mechanical resonance.

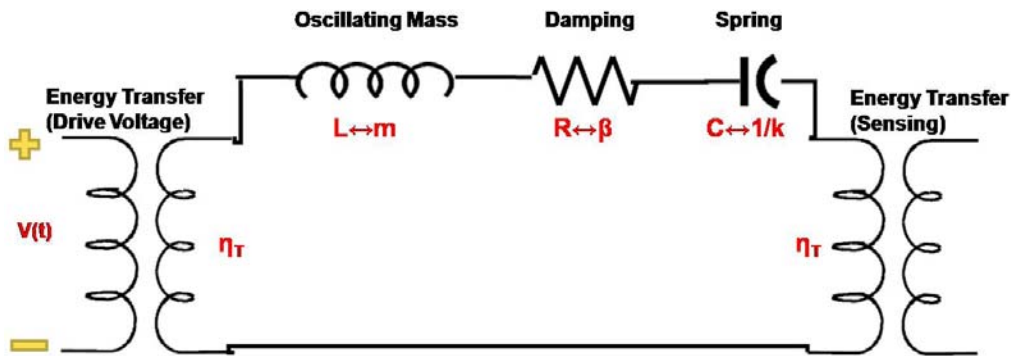


**Figure 39:** Electromechanical equivalent circuit of a comb drive resonator.

Second-order differential equations are used to express mechanical and electrical resonance expressed as

$$F(t) = m \frac{d^2}{dt^2} x(t) + \beta \frac{d}{dt} x(t) + kx(t) \quad (\text{N}) \quad (36)$$

and

$$v(t) = L \frac{d^2}{dt^2} q(t) + R \frac{d}{dt} q(t) + \frac{1}{C} q(t) \quad (\text{V}) \quad (37)$$

where  $F$ ,  $m$ ,  $\beta$ ,  $k$ ,  $x$  and  $t$  are force (N), oscillating mass (kg), damping coefficient (kg/s), spring constant (N/m), position (m) and time (s). For Equation 37,  $L$ ,  $q$ ,  $R$  and  $C$  are the inductance (H), charge (C), resistance ( $\Omega$ ) and capacitance (F). Mechanical-electrical translations can be drawn after noting the similarities of Equations 36 and 37. The inductor, resistance and capacitance can be modeled as the oscillating mass, damping coefficient, and inverse spring constant shown in Figure 39 accounting for mechanical resonance.

The transformer coupling relates the electrical and mechanical domains of Figure 39 as described by Yalcinkaya [90]. The transformer has a conversion ratio of  $1:\eta_T$ , and

$$\eta_T = n \left( V \frac{d}{dx} C \right) \quad (\text{C/m}) \quad (38)$$

where  $\eta_T$ ,  $n$ ,  $V$  and  $C$  are the transformer coupling, number of capacitive comb finger pairs, applied voltage (V) and comb finger capacitance (F) [90].

When the electrical and mechanical sections of Figure 39 are oscillating at the resonance frequency, the inductor and capacitor reactance cancel each other. In other

words, the magnitude of the resonating comb drive shuttle is defined solely by damping (resistor). The value of the mechanical resistor in Figure 39 is given as

$$R = \frac{\beta}{\eta_T^2} = \frac{\sqrt{k_S m^*}}{Q \eta_T^2} \quad (\Omega) \quad (39)$$

where  $Q$  is the quality factor of the comb drive actuator and  $m^*$  is the oscillating mass (g) [90]. Equation 39 is divided by the square of the transformer coupling to normalize the resistance. The quality factor is a dimensionless parameter defining the energy loss of the comb drive. Schmidt, *et al* [88, 91] researched energy loss of MUMPs<sup>®</sup> comb drives and approximated  $Q$  as

$$Q = z \frac{\sqrt{(m_T + m_F) k_S}}{\mu A_S} \quad (40)$$

where  $z$ ,  $\mu$ , and  $A_S$  are the distance between the shuttle and substrate (m), absolute viscosity of air (N-s/m<sup>2</sup>) and area of the shuttle plate (m<sup>2</sup>). Given Equation 39, the average sinusoidal power required to operate a comb drive,  $P_{comb}$ , is expressed as

$$P_{comb} = \frac{V^2}{2R} \quad (\text{W}) \quad (41)$$

### 3.8 Chapter Summary

Several aspects of engineering were discussed from low-Reynolds number aerodynamics to electro-mechanical system power requirements for a rotary blade MEMS robot. MEMS actuators were surveyed, and the comb drive's exceptional frequency response is ideal for high spin rates. The analytical expressions developed for

actuator force, resonance frequency and power will be utilized to develop a conceptual model for the robot.

## **IV. Design and Fabrication Methodology**

### **4.1 Chapter Overview**

This chapter presents the flying MEMS robot design. The design of MEMS comb drive rotary actuators and three wing designs are presented. The following sections describe how the MEMS devices assemble to form the actuating system. The chapter concludes with other design considerations and assembly using flip chip/bond technology.

### **4.2 MEMS Surface Micro-Machining Design**

#### ***4.2.1 Actuation***

Section 3.5.1 ruled out most actuators excluding comb drive resonators for turning rotary wings. Comb drive resonators offer exceptional frequency for high spin rates. Comb drives provide lateral deflection, but when two are connected orthogonally they are capable of circular actuation. The circular actuation corresponds to the pinion gear concept discussed in Section 3.6.

As shown in Figure 40, the orthogonal comb drives are physically attached at the ends of their push rods. At this joint, the pinion gear teeth are positioned linearly—similar to a rack gear, but the rotary motion is modeled as a circular pinion gear. The comb drive electrostatic force is used to position the linear rack, but the restoring force of the flexures is utilized to turn the master gear and wings. The number of teeth that engage the master gear per cycle of the comb drive is the “net” number of teeth for the modeled pinion gear. The interdigitized comb fingers are designed of stacked Poly1-2 to

increase the electrostatic force as evident in Equation 23. The shuttle and springs are designed of Poly1 for frequency and force optimization (details in Section 5.3).

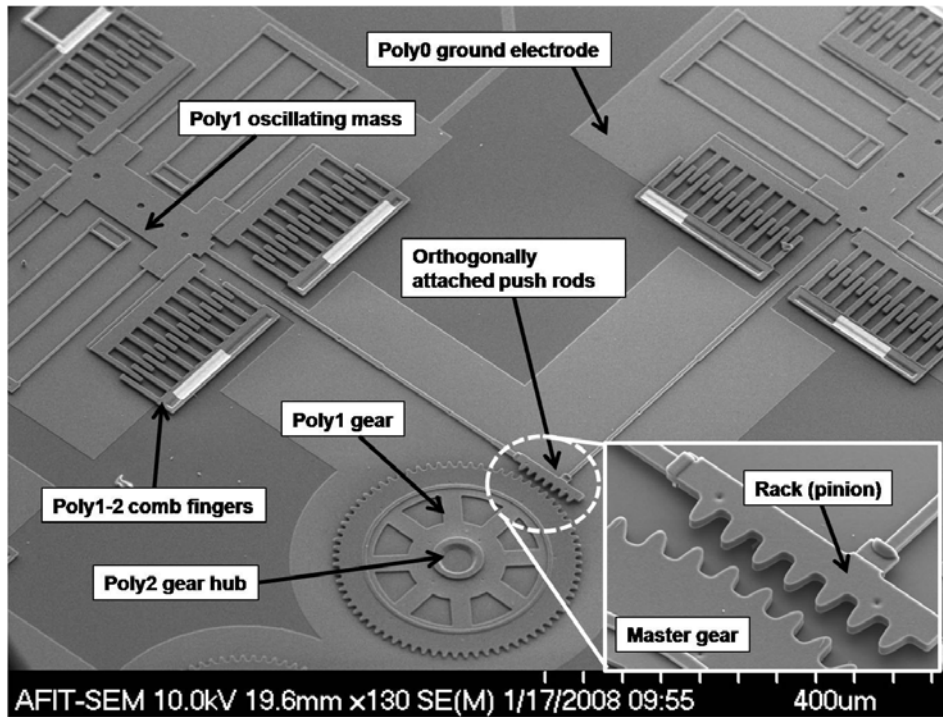


**Figure 40:** SEM picture of orthogonal comb drive design showing an SEM close-up picture of the linear rack and master gear.

The orthogonal comb drives are designed so the peak-to-peak displacement,  $d_{pp}$ , of the rack is not longer than the length of the rack. Exceeding this distance is wasteful as the number of teeth meshing with the master gear remains the same per cycle. This relationship is expressed as

$$d_{pp} = \frac{\epsilon_0 \epsilon_{air} n t_p L_S^3}{12 h E_p I_z} V^2 \leq L_{rack} \quad (m) \quad (42)$$

where  $L_{rack}$  is the length of the rack (m).

#### 4.2.2 Gear

The master gear is the turning mechanism for the rotary wings. The rack gear rotates like a pinion gear which engages the master gear. The dynamics of the master gear are determined by a gear ratio and are dependent on the design of the orthogonal comb drive system. The gear is made of Poly1 to reduce total weight and to possibly fabricate the wings pre-attached which requires Poly2 (since only two structural polysilicon layers are available with the MUMPs<sup>®</sup> process). The gear utilizes dimples to reduce stiction and friction. The gear rotates on Poly0 to ensure a common electronic ground between the comb drive rack and gear. Without Poly0, the isolating nitride layer could break down at the high voltages required for actuating comb drives [50]. The stationary hub axis is made of Poly2 and holds the gear in place. The gear is not anchored; so, when the sacrificial oxide layers are released, the gear slides down the hub 1.25  $\mu\text{m}$  (Oxide1-Dimple) to rest on the Poly0. Figure 41 shows a diagram of the gear and hub.

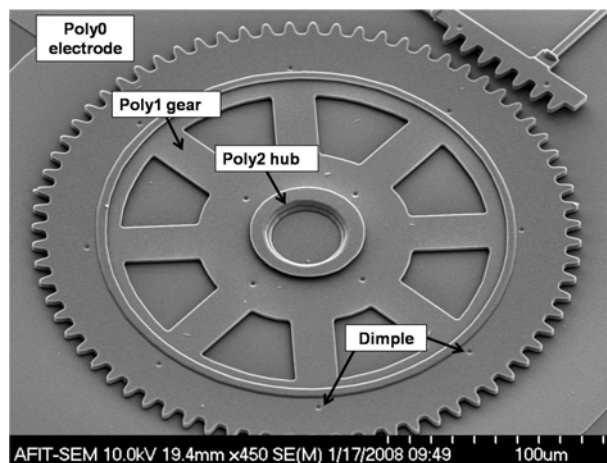


**Figure 41:** SEM picture showing the Poly1 master gear and Poly 2 hub axis. The gear rotates on the Poly0 ground electrode using dimples.

### 4.2.3 Wings

Three rotary wing designs were implemented using the MUMPs<sup>®</sup> fabrication process. The first wing design was slightly modified from Glauvitz' version [50]. The second design followed design guidelines put forth by Tsuzuki, *et al.* These two designs were fabricated separately in an attempt to assemble the wing to the master gear using flip bond technology. The last design attempted to fabricate wings without assembly. The following paragraphs describe each in more detail.

#### 4.2.3.1 Glauvitz Wing (Wing-G)

The first wing design existed prior to conducting this research, and was only slightly modified. Glauvitz' research found fabricating wings were best designed using Poly2 and Gold. The thin-film stress of the two materials created a small pitch angle required for thrust, but the angle was small ( $\sim 5^\circ$ ) relative to the required 15-20° shown by Tsuzuki [69].

The pitch angle solution was to create a hinge using photoresist. For the Glauvitz wing (Wing-G), the wing ribs were separated 2-3  $\mu\text{m}$  from the main spar. Glauvitz attempted the hinge on Poly1 wings, but the overlying Oxide2 layer above Poly1 created challenges for the HF oxide release. Similar wings were designed of Poly2 and Gold (eliminating Poly1) in this research to fabricate a wing with a 15-20° pitch angle as shown in Figure 42.

The dimensions of the wing in Figure 42 are 1270  $\mu\text{m}$  radius x 540  $\mu\text{m}$  chord length. Due to the large chord segment, it is difficult to position more than four wings



adjacent to each other. Therefore, the best designed rotor is a four wing rotor, or quad-rotor.

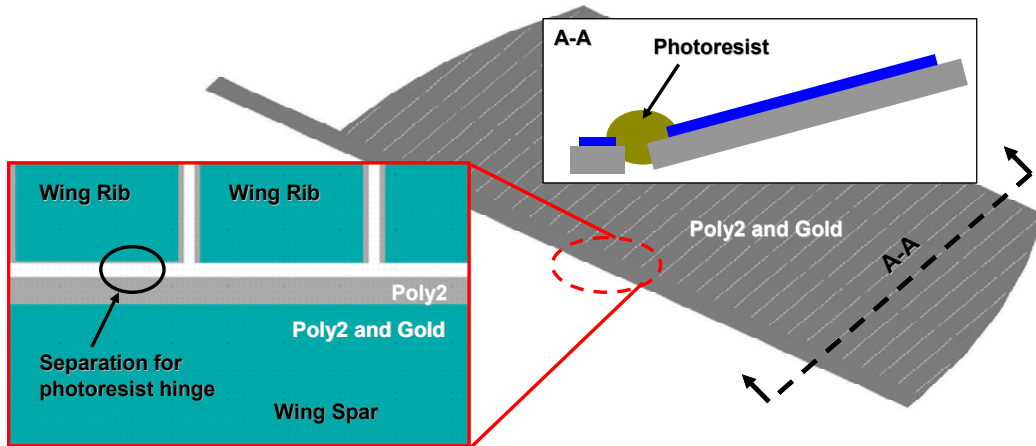


**Figure 42:** Poly2-Gold rotary wing showing the separation of the ribs from the spar for the photoresist hinge. A cross section of the photoresist hinge is shown in the top right.

#### 4.2.3.2 Tsuzuki Wing (Wing-T)

The second wing was modeled after following Tsuzuki’s design guidelines described in Section 3.2.3. The research pointed out the overall wing geometry benefits most from a flat rectangular shape, which is ideal for the planar MUMPs<sup>®</sup> process; but, for the same reasons a few guidelines were challenging to include in the design. The implemented design ideas were overall dimensions, corrugation, camber, and associated ratios between them. Figure 43 shows the Tsuzuki wing (Wing-T) designed in L-Edit and imaged with an SEM.

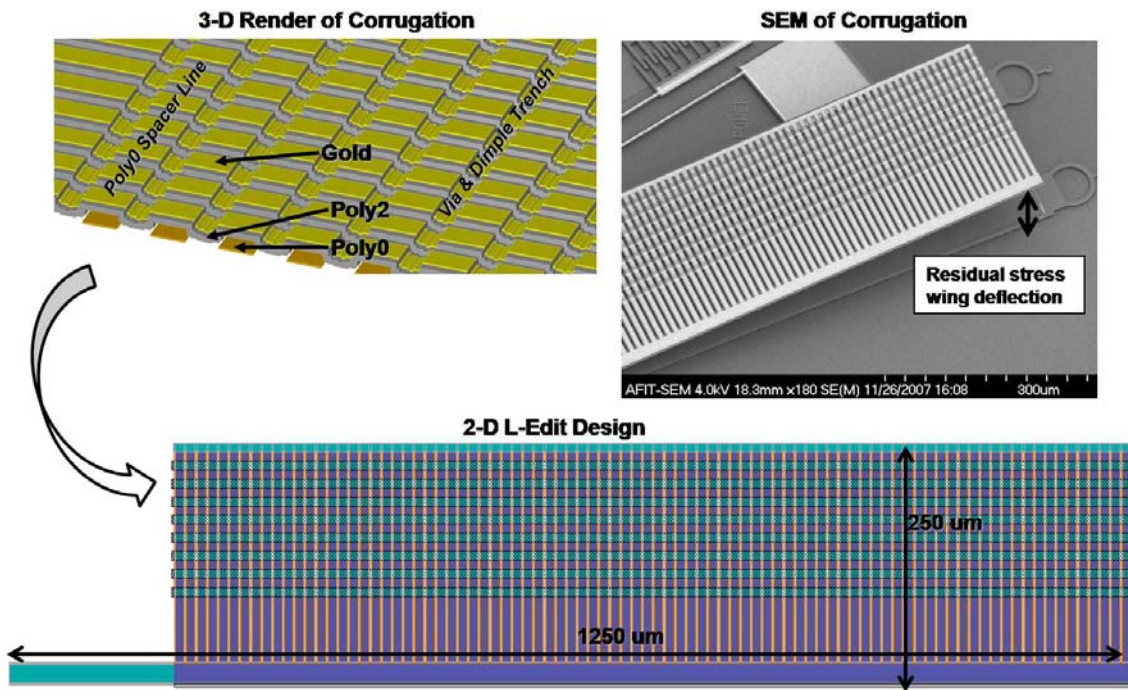


**Figure 43:** Wing-T modeled in L-Edit using the MUMPs<sup>®</sup> fabrication process. The corrugation detail was achieved using alternating Poly0 spacer and Via-Dimple trench lines.

The overall dimensions of the wing are approximately 1250  $\mu\text{m}$  radius x 250  $\mu\text{m}$  chord. The aspect ratio, the ratio of radius to chord, results in 5.0. The thickness of the wing is simply a Poly2 and Gold stack, or 2  $\mu\text{m}$ . Therefore, the thickness-to-chord ratio is approximately 0.8 %. Each corrugation of the trailing edge is roughly 8  $\mu\text{m}$  wide and 2  $\mu\text{m}$  deep. The depth of the corrugation was achieved using alternating lines of Poly0 as a spacer and Via/Dimple trenches. The Poly0 raised the surface 0.5  $\mu\text{m}$  and the Via/dimple trench lowered the surface 1.5  $\mu\text{m}$  for a total 2  $\mu\text{m}$  deep corrugation. The resulting corrugation width-to-depth ratio is 4. The addition of a Poly 1 spacer combined with Poly0 lines can decrease the ratio to approximately 2. Up to five wings are available per

rotor since the chord length is shorter than Wing-G. Table 8 summarizes the wing design parameters compared to Tsuzuki’s recommendations.

**Table 8:** Wing-T design parameters compared to Tsuzuki’s recommendations.

<i>Parameter</i>	<i>MUMPs® Design</i>	<i>Tsuzuki Design</i>
Wing Geometry	Flat Plate	Flat Plate
Aspect Ratio	5.0	5.5
Thickness:Chord Ratio	0.8	2
Corrugation Width:Depth	4.0 (2.0)*	1.87

\*using a Poly0 and Poly1 spacer

#### 4.2.3.3 Pre-Attached Wings

The third type of wing is not necessarily a new design; instead, the same two wings as described above are fabricated pre-attached to the master gear. This methodology would not require flip bond assembly technology. The wings are attached to the master gear using the Via etch by removing Oxide2 above the gear where the Poly2 wings adhere to the Poly1. Figure 44 shows the Via wing attachments.

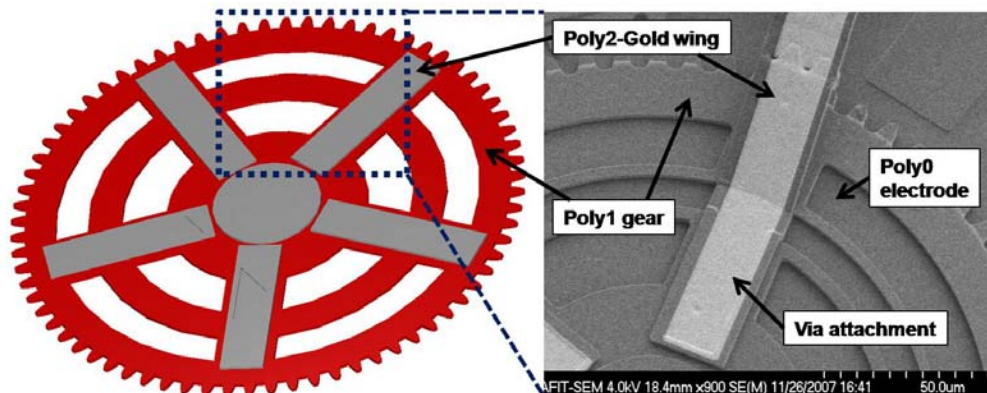


**Figure 44:** L-Edit 3-D render of Poly2-Gold wing sections attached to the master gear using Via etches. A close-up SEM of the wing attachment is shown on the right.

#### 4.2.3.4 Conformal Topology

The MUMPs<sup>®</sup> process is conformal meaning the topology of underlying layers is reproduced in the layers above them. For designing wings pre-attached to the master gear, the underlying topology will yield a peculiar shaped wing. The solution is to add a spacer layer underneath the wings to mitigate unnecessary corrugation.

The wings are attached near the center of the gear and extend far beyond the gear. As the wing extends beyond the gear teeth, an imprint of the gear teeth and a drop off resulting from the outer edge of the Poly1 gear will result in a bent wing. But, if a layer of Poly1 is fabricated below the wing (unattached), the drop off topology is mitigated. Creating a spacer with meshing teeth below the wing will further reduce the topology effects on the wing. The same concept applies Figure 45 shows a diagram of the effects of including a Poly1 wing spacer.

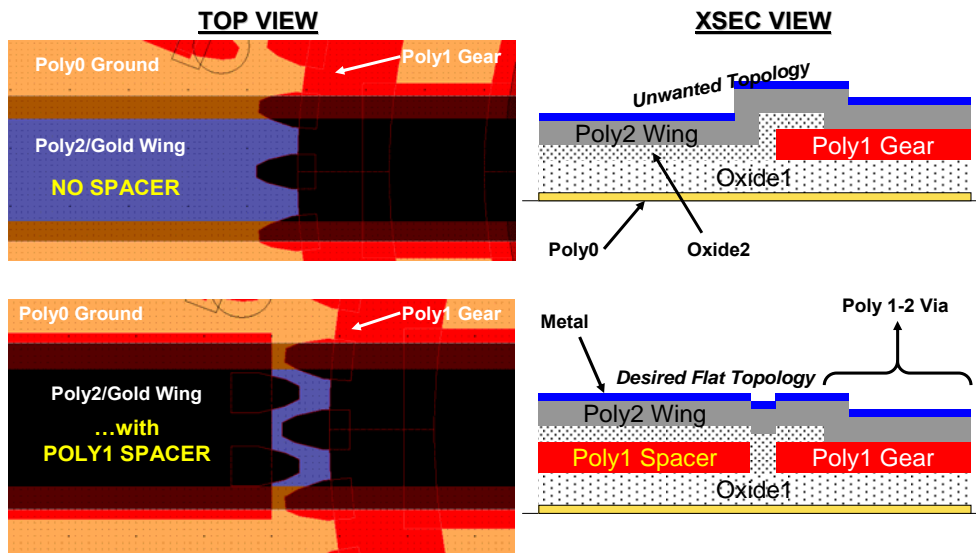


**Figure 45:** Shown on the left is the L-Edit top view of the master gear where the Poly2/Gold wing extends beyond the gear teeth. The effects of using a spacer are shown in the lower half. Shown to the right are the associated cross sectional views to conceptualize the desired topology effect using a spacer.

The same concept can be used in other ways underneath the wing. The Poly1 spacer can be patterned identically as the Poly0 corrugation lines discussed in the previous section. This additional 2  $\mu\text{m}$  height decreases the corrugation width-to-depth ratio to roughly 2.0—close to Tsuzuki’s guideline of 1.87 (refer to Table 6). Spacers were also included near the push rods. However, using residual stress theory presented in Section 3.3, the Poly2/Gold wings will deflect upward; most likely sufficient to avoid contact with the comb resonator actuators parts beneath.

Perhaps most important of all is ensuring the gear teeth mesh with the comb drive rack teeth. The issue is exigent because the master gear will drop 1.25  $\mu\text{m}$  after the oxide layers are released in HF (post-release height range of 0.75-2.75  $\mu\text{m}$ ). Without compensation, the meshing teeth (post-release height range of 2-4  $\mu\text{m}$ ) will overlap just 0.75  $\mu\text{m}$  posing the risk of the rack teeth sliding above the gear. The solution is to use a dimple etch over the comb drive rack teeth lowering it 0.75  $\mu\text{m}$ . Using the dimple etch, the teeth will have 1.50  $\mu\text{m}$  of overlap. Figure 46 shows the dimple feature on the rack.

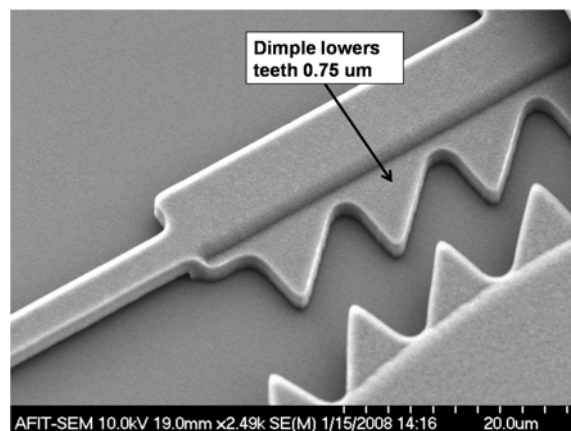


**Figure 46:** SEM picture illustrating the advantage of lowering the rack teeth 0.75  $\mu\text{m}$  using the dimple etch feature. Lowering the teeth increases the mesh alignment to the gear teeth.

### 4.3 Assembling MEMS with Flip Chip Technology

The wings were primarily designed for the purpose of assembling them to form a MEMS system. Assembling is achieved using flip chip, or flip bond, technology. Flip bonding requires two separate chips—one containing the MEMS system and the other a MEMS part. Typically, flip bond machines use vacuum force to hold the respective chips. The top and bottom chips are faced toward each other. Using sophisticated aligning techniques, the chips are brought into contact, and a combination of high pressure (40-60 psi) and high temperature (400-650° C) gas is applied to the chips to create the bond.

Several MEMS devices were fabricated for assembly—the actuating system, wings, and shaft collars. The shaft collars are shaped like an O-ring and are placed around the gear hub so they rotate at the gear's frequency. The shaft collars serve to add height to the wings to: (1) increase the airflow beneath the wing for suitable thrust force and (2) prevent the wings from contacting the substrate resulting from the downward 15-20° pitch angle (wing trailing edge points down after assembly). Each shaft collar is 4.75 μm thick—the maximum structural thickness available in the MUMPs® process layers. Unfortunately, the larger the wing's chord length, the more collars are required to offset the wings' vertical deflection. Figure 47 shows an SEM image of one shaft collar, and Table 9 shows the minimum number of shaft collars required for each wing design based on the optimum angle of attack.

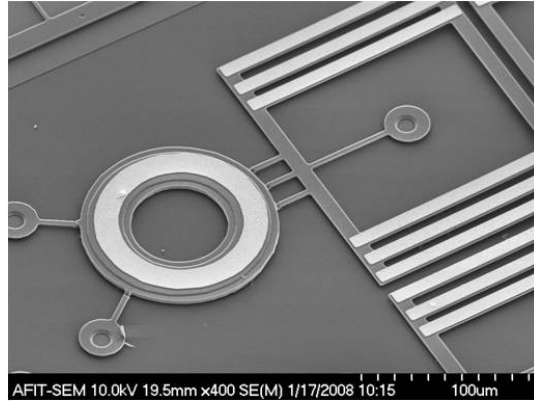


**Figure 47:** SEM picture of a shaft collar with thickness of 4.75  $\mu\text{m}$ . The shaft collar, when stacked, forms the shaft to offset the wings above the substrate.

**Table 9:** Required shaft height and assembly steps for the optimal pitch angle range of 15-20°.

<i>Parameter</i>	<i>Wing-G</i>		<i>Wing-T</i>	
	<i>15°</i>	<i>20°</i>	<i>15°</i>	<i>20°</i>
Chord length ( $\mu\text{m}$ )	540	540	250	250
Vertical offset ( $\mu\text{m}$ )	139.8	184.7	64.7	85.5
Required shaft collars*	29	39	13	18

\* Includes the offset of the Poly1 master gear and dimples

When using the flip bonder, the two chips are joined together before releasing the oxides. After establishing a sufficient bond, the two chips form a “sandwich” with oxide in the middle. The joined chips are submerged in HF together to release the oxide between the chips. The chip with the MEMS part will separate from its parent chip while attached to the MEMS system chip. Small anchors tethering the MEMS device to the parent chip are broken beforehand to ensure the MEMS device separates. This process is repeated as necessary to build the shaft to sufficient height and attach the rotary wings. A diagram of the flip chip process is shown in Figure 48.

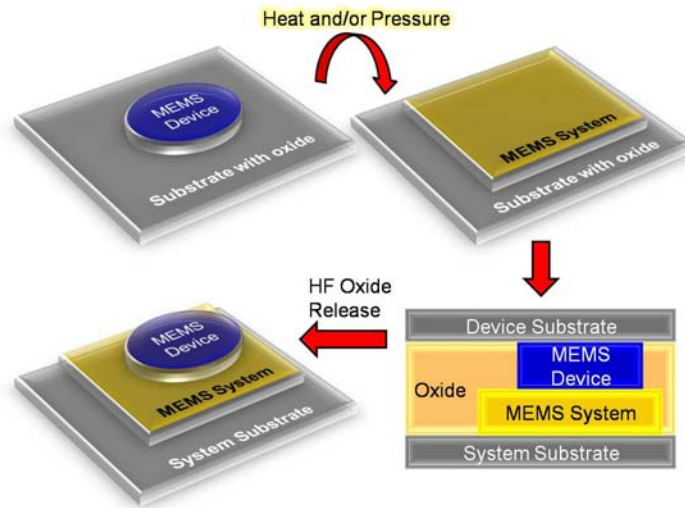


**Figure 48:** Flip chip assembly process. The MEMS device and substrate are bonded to the MEMS system using high temperature and/or high pressure. The device substrate floats away leaving behind the assembled MEMS device during an HF oxide release.

#### 4.4 Chapter Summary

This chapter presented MEMS designs to enable rotary-wing actuation. The rotary actuation system consisted of two orthogonally attached comb drive actuators. Two wing designs were shown including one with features conducive to low-Reynolds number flow regimes. The building blocks of the design—the master gear, rotating pinion rack and wing attachments were discussed in detail. The concept of using spacers was also introduced as a method to overcome undesirable topology effects. Finally, the details of building a shaft of collars for attaching the rotor via flip bond technology were explained. For further design details refer to the L-Edit 2-D CAD drawings in Appendix A. Next, Chapter 5 combines the theory of Chapter 3 and designs of this chapter to analyze and model the components of a rotary-wing flying MEMS robot.



## V. Modeling and Analysis

### 5.1 Chapter Overview

This chapter presents the modeling and analytical results for predicting the performance of the flying MEMS robot presented in Chapter 4. Modeling was achieved using CoventorWare<sup>®</sup> MEMS finite element analysis (FEA) software. Simulations were conducted to compare beam and wing deflection, comb frequency and displacement to the theoretical expressions given in Chapter 3. Analytical expressions were also formulated to define the required actuation force, mass limitations, and total power required for flight.

### 5.2 Thin-film Residual Stress

Thin-film stress is sensitive to the ambient environment (temp, humidity, etc) and the release process. Therefore, it is imperative to determine the residual stress for each die received from the MUMPs<sup>®</sup> fabrication foundry as they differ chip to chip. Residual stress values are commonly extracted from simple MUMPs<sup>®</sup> cantilever beams using the theoretical relationships developed in Section 3.4.

#### 5.2.1 *Thin-Film Stress and Deflection*

Thermal and internal thin-film stress values are required for input into CoventorWare<sup>®</sup>. An accepted method for approximating modeled thin-film stress is to iteratively match, or calibrate, modeled cantilever beam deflection to experimental cantilever beam deflection results [20, 50]. First, the Poly2 layer cantilever beams are

calibrated followed by fine-tuning the gold stress of a Poly2/Gold bilayer to match the empirical results.

Three MUMPs<sup>®</sup> dies were fabricated during this thesis research, and the internal residual stresses for each run are shown in Table 10. The beams were calibrated for MUMPs<sup>®</sup> Run 79 after measuring them under a Zygo interferometric microscope (IFM) as shown in Figure 49. The total FEA-calibrated thin-film stress of Poly2 and Gold was -12 MPa (compressive) and 95 MPa (tensile), respectively; these values were used throughout to standardize the models.

**Table 10:** PolyMUMPs<sup>®</sup> foundry internal residual stress and thickness data for MUMPs<sup>®</sup> Runs 78-80. Tensile and compressive stress is denoted T and C, respectively [92].

Layer	Run 78		Run 79		Run 80	
	Thickness (μm)	Stress (MPa)	Thickness (μm)	Stress (MPa)	Thickness (μm)	Stress (MPa)
Nitride	0.608	150 T	0.585	62.5 T	0.601	79 T
Poly0	4.919	25.3 C	0.4944	26.7 C	0.497	32 C
Oxide1	1.909	---	1.983	---	1.922	---
Poly1	1.999	7.7 C	1.998	8.3 C	2.002	7.3 C
Oxide2	0.731	---	0.756	---	0.743	---
Poly2	1.512	8.7 C	1.509	4.3 C	1.509	8.3 C
Metal (Au)	0.484	13.2 T	0.515	10.3 T	0.4933	13.2 T

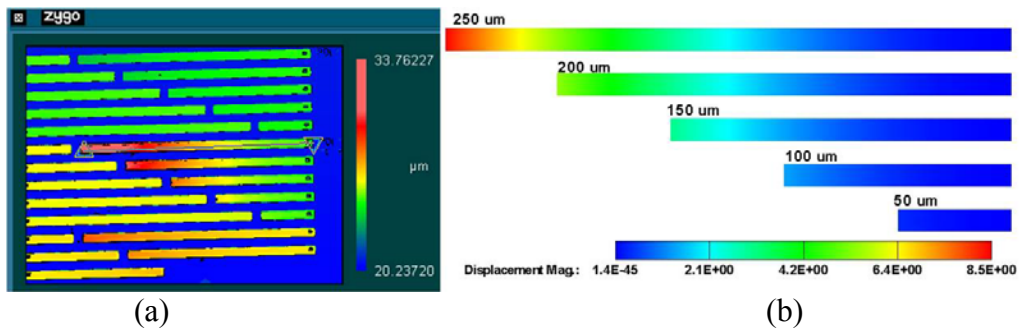


**Figure 49:** (a) Cantilever beams were measured under a Zygo Interferometric Microscope (IFM) and (b) calibrated in CoventorWare<sup>®</sup> to match the empirical deflections.

### 5.2.2 Wing Deflection

The stress results of Section 5.2.1 were used to predict the deflection of the rotary wings. The deflection of the wing occurs in two sections—the leading edge (LE) and the rib arrays (chord). The deflection of the LE is different than a simple cantilever beam due to the increased mass in the chord dimension and variable cross sectional area along the LE. However, the rib arrays can be modeled as one wide cantilever beam with uniform deflection. The rib arrays are attached to the spar; therefore, the point of maximum wing deflection occurs at the tip of the farthest rib.

Each wing design was imported into CoventorWare<sup>®</sup> to model the stress-related deflection. Wing-T was modified to include less corrugation because CoventorWare<sup>®</sup> was limited in simulation memory. For similar reasons, the Wing-G used a tapered design to eliminate rounded features. Figure 50 and Figure 51 show the simulated results. The left ends of each model are fixed since they will be attached to the master gear at this point.

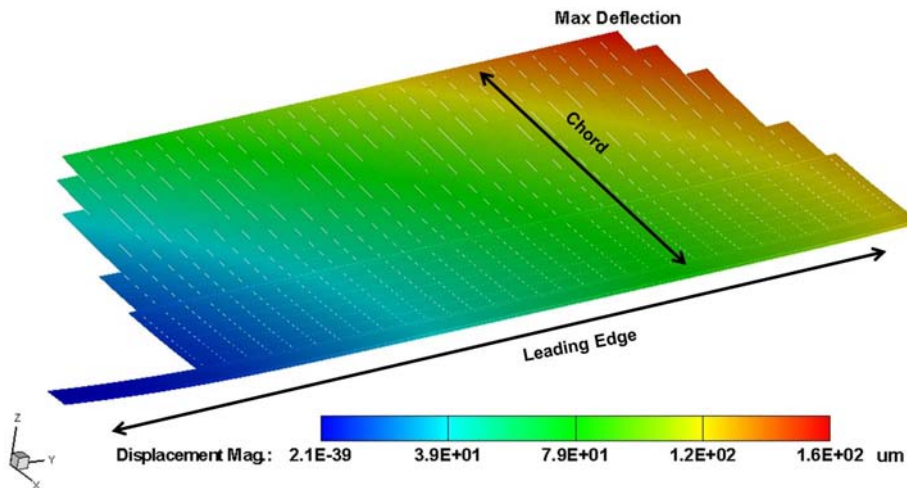


**Figure 50:** CoventorWare<sup>®</sup> analysis of Wing-G deflection. The maximum deflection occurred at the farthest rib tip at approximately 160  $\mu\text{m}$  out-of-plane.

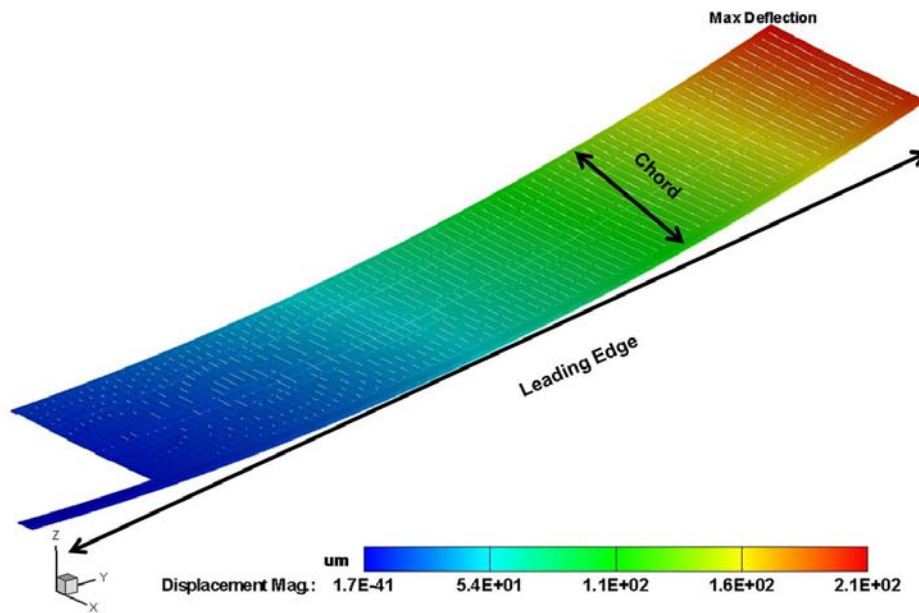


**Figure 51:** CoventorWare<sup>®</sup> analysis of Wing-T deflection. The maximum deflection occurred at the farthest rib tip at approximately 210  $\mu\text{m}$  out-of-plane.

Data points were extracted from the leading edge of each wing and compared to calculated deflection in Figure 52 and Figure 53. For ease, the analytical values were computed using simple cantilever beam expressions. Two methods were used for analytical deflection calculations—(Analytical 1) using Equations 13 and 18 independent of  $R_{bilayer}$  and (Analytical 2) using Equations 15 and 18 dependent on  $R_{bilayer}$ . Wing-G matched closely with Analytical 1 for lengths less than 1 mm, and Wing-T followed Analytical 2 results within 20%. In general, the simulated and calculated values agree very well for wing lengths less than 0.6 mm. The discrepancy of the analytical values at larger distances is attributed to neglecting the variable area moment of inertia and chord mass of the wing; so, the simulated results are the most accurate. The shorter chord of Wing-T allowed the spar to deflect more parabolic as opposed to the near-linear deflection of the heavy Wing-G.

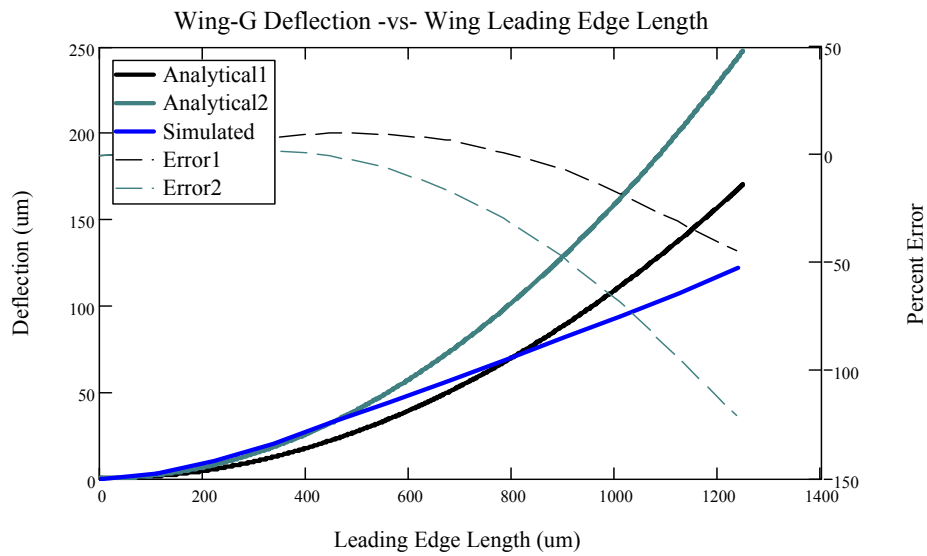


**Figure 52:** Simulated and analytical Wing-G deflection versus leading edge length. The simulated wing deflection closely resembles Analytical 1 values for length less than 1-mm

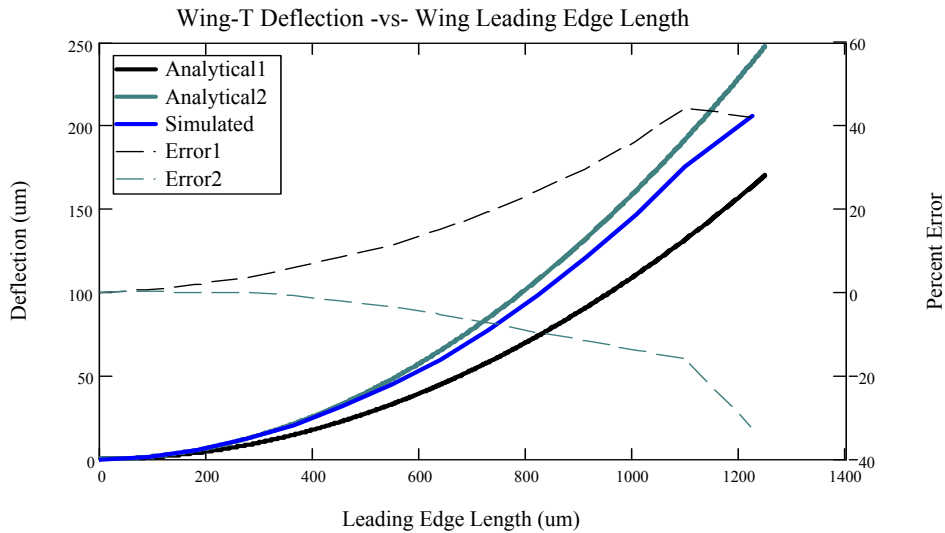


**Figure 53:** Simulated and analytical Wing-T deflection versus leading edge length. The simulated wing deflection closely resembles Analytical 2 values within 20%.

The simulated and calculated deflection of each wing's chord is shown in Figure 54. Only Analytical 1 was included because the chord segments are simple cantilevers

beams. The calculated deflection was within 5% of the simulated data. Deflection calculations are shown in Appendix B.

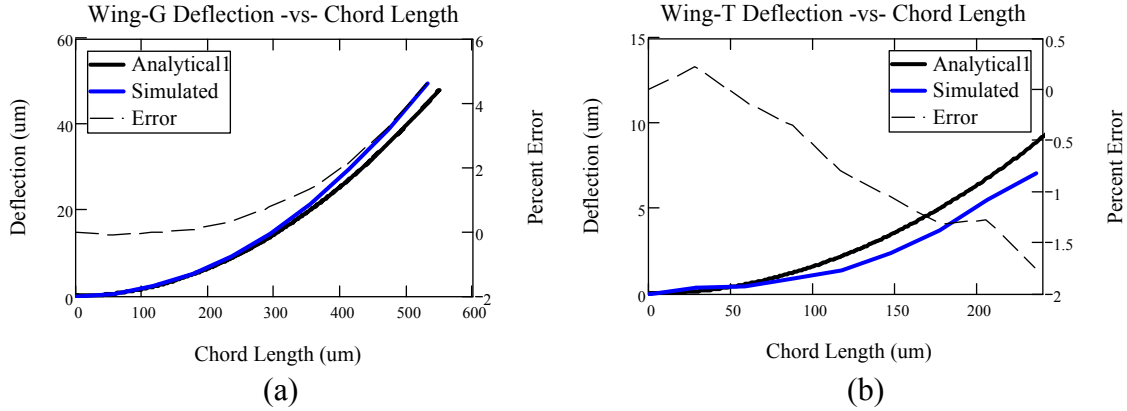


**Figure 54:** Simulated and analytical chord length results of (a) Wing-G and (b) Wing-T agree within 5%.

The simulated and calculated maximum wing deflection values are given in Table 11. Wing-G has a large mass and an unaccounted area moment of inertia in the analytical calculations which explains the large error. But, Wing-T has less than half of the mass on the chord; so, the modeled data closely matches the analytical values.

**Table 11:** Comparison of simulated and calculated maximum deflection of the MEMS wings.

	<i>Modeled</i> ( $\mu m$ )	<i>Analytical1</i> ( $\mu m$ )	<i>Analytical2</i> ( $\mu m$ )	<i>Percent Difference</i>	
				$(Mod - A1) \frac{100}{Mod}$	$(Mod - A2) \frac{100}{Mod}$
Wing-G	172.1	214.3	290.7	-24.5	-68.9
Wing-T	212.8	173.0	247.2	<b>18.7</b>	<b>16.1</b>

### 5.3 Analysis of Drive System

The comb drive actuator presents many engineering aspects worth analyzing. The comb drive includes a myriad of geometric design considerations to optimize frequency,

deflection and force. Such comb drive geometric parameters include the number of comb finger pairs, the thickness of the comb fingers, the stiffness of the flexures, length of flexures and the mass of the shuttle—all of which have engineering trade-offs.

### 5.3.1 Analysis of Frequency

Optimizing frequency is priority since obtaining a suitable thrust force is solely dependent on how quickly the rotor turns. According to Equation 31,

$$f_{comb} \propto \left( \frac{k_S}{m^*} \right)^{0.5} \quad (\text{Hz}) \quad (43)$$

which focuses attention towards a balance between increasing flexure stiffness and decreasing the mass of the shuttle, flexures, and truss. However, the flexures and truss typically account for less than a quarter of the total mass; so, decreasing the shuttle mass is essential.

Most of the shuttle's mass is found in the comb fingers. Figure 55 shows the effect of increasing the shuttle's total number of comb fingers on the comb drive's operating frequency. The frequency rapidly increases as the number of comb fingers decreases less than 36. The trade-off between the two polysilicon layers is subtle for 36 or more comb fingers. When  $n < 36$ , the decrease in mass using Poly2 outweighs the increase of the Poly1 spring constant; thus, slightly improving the frequency performance. The highest frequencies are obtained using a stiffer Poly1-2 stacked layer, but the overall mass of the comb drive is almost doubled. Utilizing Poly2 exhibits superior frequency performance for comb fingers less than 36, and for  $n=36$  the material choice is insignificant.

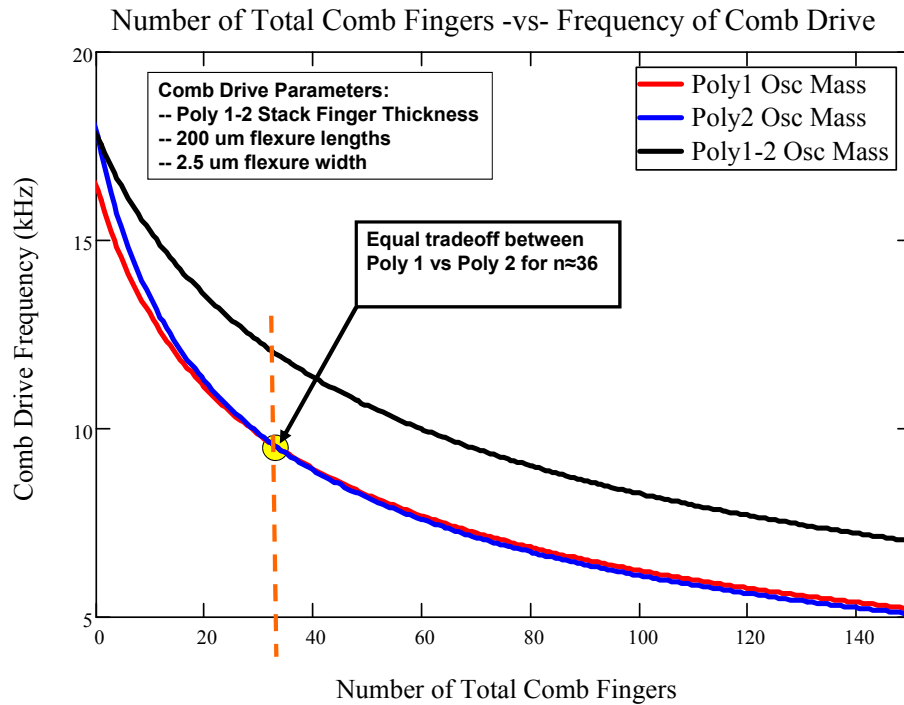


**Figure 55:** Graph of number of comb fingers versus the comb drive frequency. As shown, the number of comb fingers is best designed at or below 36 for high frequency application. As the number of fingers increase, the frequency trade-off of using Poly 1 or Poly 2 is subtle.

CoventorWare<sup>®</sup> finite element models (FEM) were created with varying number of comb fingers. The finite element analysis (FEA) was strictly mechanical which found the particular frequency mode of the lateral shuttle displacement. Table 12 compares the calculated and FEA results for a Poly1 device which is in close agreement.

**Table 12:** Calculated and modeled resonance frequency for various numbers of total comb fingers. For each, the shuttle is Poly 1 with 200  $\mu\text{m}$  long and 2.5  $\mu\text{m}$  wide flexures.

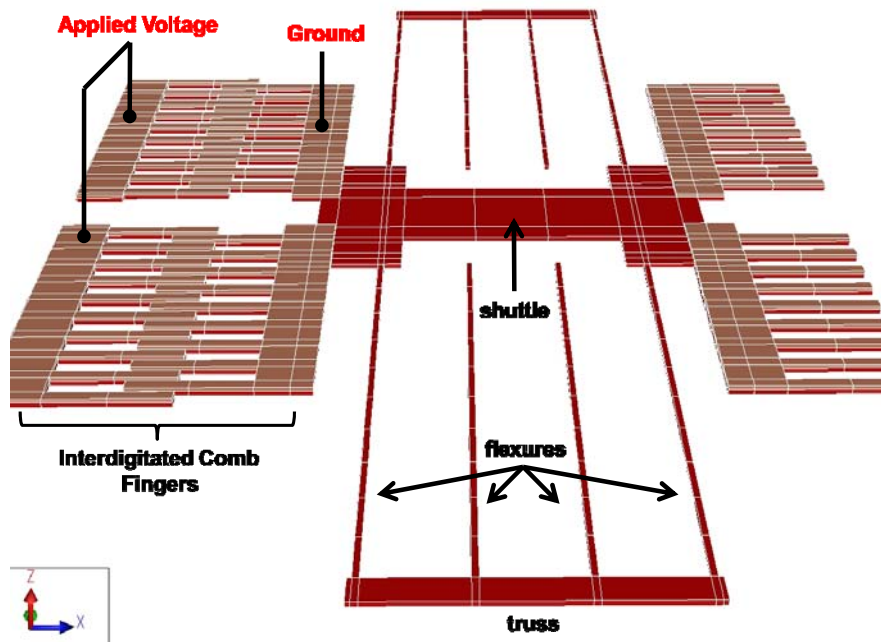
<i>No. Comb Fingers</i>	<i>Calculated Resonance Frequency (kHz)</i>	<i>Modeled Resonance Frequency (kHz)</i>	<i>% Difference</i>
36	9.249	8.648	6.49
40	8.946	8.315	7.05
44	8.643	8.017	6.99
48	8.369	7.749	6.93
52	8.120	7.507	7.55



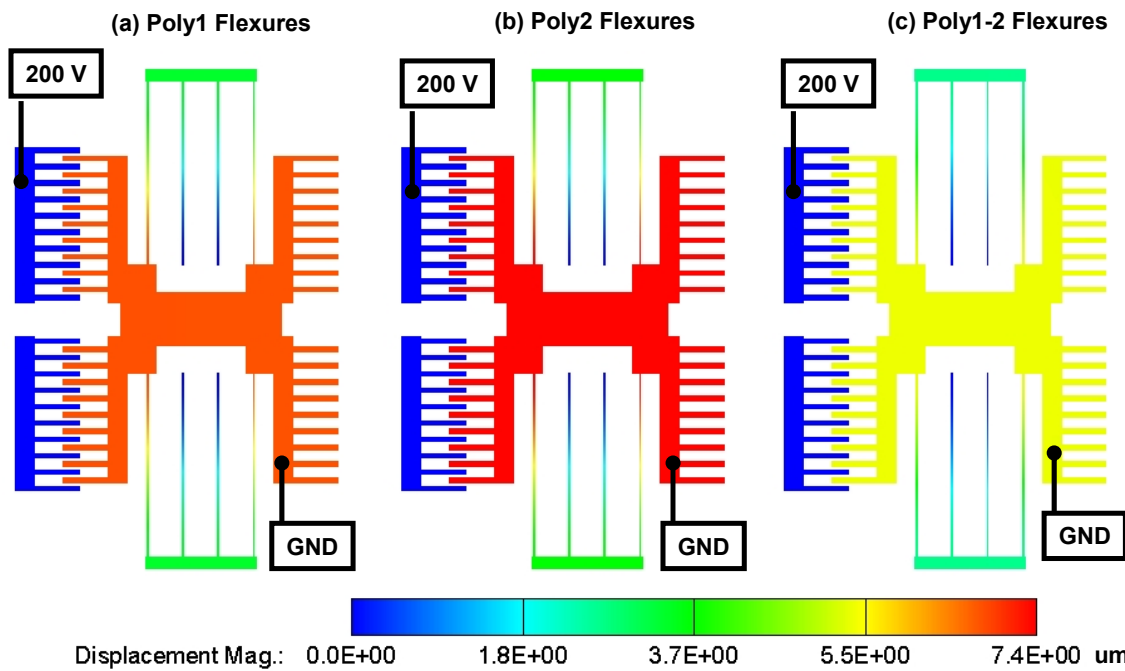
### 5.3.2 Analysis of Deflection

The rack will deflect laterally for one comb drive and in a circular motion in the orthogonal comb drive setup. Each of the two comb drives in the orthogonal pair is designed identically so their deflections are equal. The more equal their lateral displacements, the more circular the rack motion in the orthogonal scheme.

A deflection analysis was calculated using Equation 30 and compared to FEA models in CoventorWare<sup>®</sup>. The FEA stepped through voltages of 0-200 V in 50 V increments for three different models—Poly1, Poly2 and stacked polysilicon flexures. A representative FEA mesh of one comb drive actuator is shown in Figure 56. Figure 57 shows the simulated displacement results for a 200 V applied potential to the outer comb fingers. Poly2 deflects the most because it possesses a low spring constant.

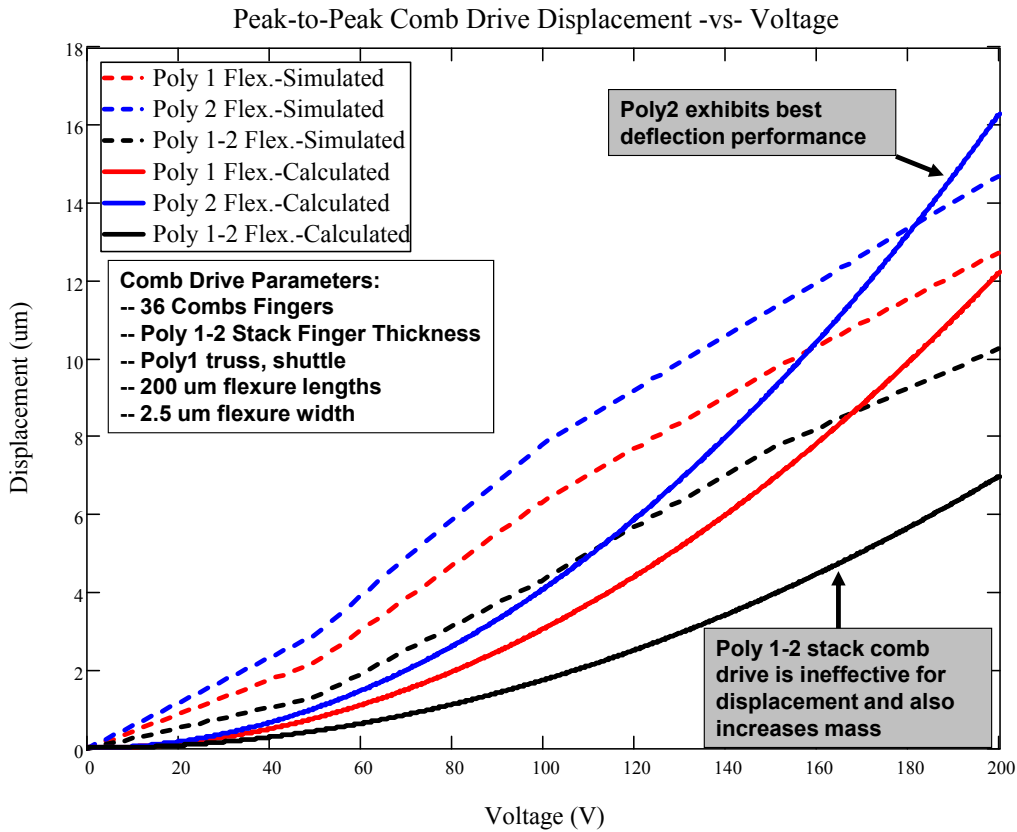


**Figure 56:** Simplified CoventorWare<sup>®</sup> FEA model of comb drive. The comb drive has a Manhattan Brick mesh of  $25 \times 25 \times 5 \mu\text{m}^3$  (x, y, z axes) partitions.



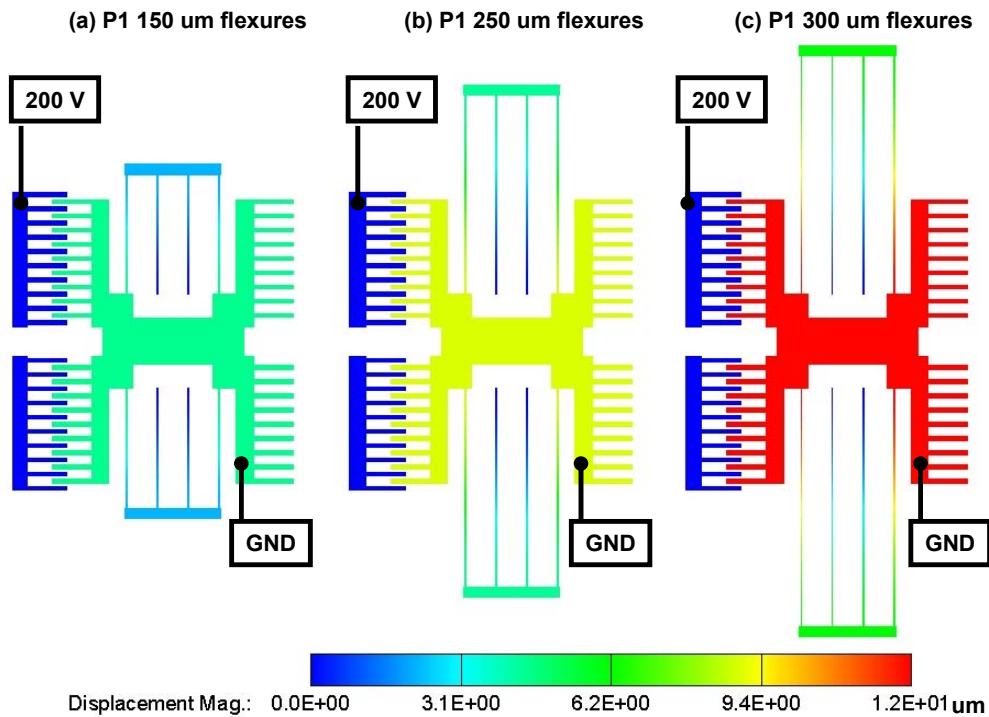
**Figure 57:** The effect of changing the flexure thickness is shown with (a) Poly1, (b) Poly2 and (c) Poly1-2 thickness. The flexures are all 200 μm long and 2.5 μm wide, and the applied voltage is 200 V.

Figure 58 compares the simulated and calculated displacement results. The Poly2 springs deflect the most which is attributed to its low spring constant resulting from a lower area moment of inertia. Figure 58 also confirms using a stacked polysilicon flexure is not effective; not only does the displacement decrease, but the added thickness increases the weight of the robot. The modeled data increased more linearly than the calculated displacement, but both were in agreement for Poly1 and Poly2 at high voltages. Differences in the calculated values are attributed to residual stress and mesh size which are unaccounted for in the stress expressions.



**Figure 58:** Simulated and calculated peak-to-peak displacement of three types of comb drive actuators as a function of voltage. The effect of changing the material and thickness of the flexures is shown.

Another FEA was conducted to observe the effect of using different length folded flexures. A CoventoreWare<sup>®</sup> analysis was designed using flexure lengths ranging from 150-300 µm in 50 µm increments using the same mesh in Figure 56. The FEA results are pictured in Figure 59 (for L=200 µm, see Figure 57a) and verify the relationship given by Equation 29—shuttle deflection increases with increasing flexure length. Poly1 was simulated because it has a higher restoring force (higher spring constant) with just slightly less deflection compared to Poly2.



**Figure 59:** The effect of changing the flexure length is shown with (a) 150  $\mu\text{m}$ , (b) 250  $\mu\text{m}$  and (c) 300  $\mu\text{m}$  long Poly1 flexures. Each comb drive is completely Poly1 with stacked comb fingers, and the applied voltage is 200V. The 200  $\mu\text{m}$  long flexures are shown in Figure 57a.

Figure 60 compares the modeled results in Figure 59 and the calculated results using Equation 29. The modeled results appear to diverge from the calculated curves for each flexure length, but the divergence is less pronounced for shorter flexure lengths. In general, the modeled results match closer to the calculated values for longer flexures. The discrepancy of the two curves is attributed to the method of calculating the area moment of inertia for the flexure spring constant; CoventorWare<sup>®</sup> uses the bending stress equation (Equation 12) and the analytical values use geometric dimensions (Equation 28). Detailed comb drive deflection calculations are shown in Appendix C.

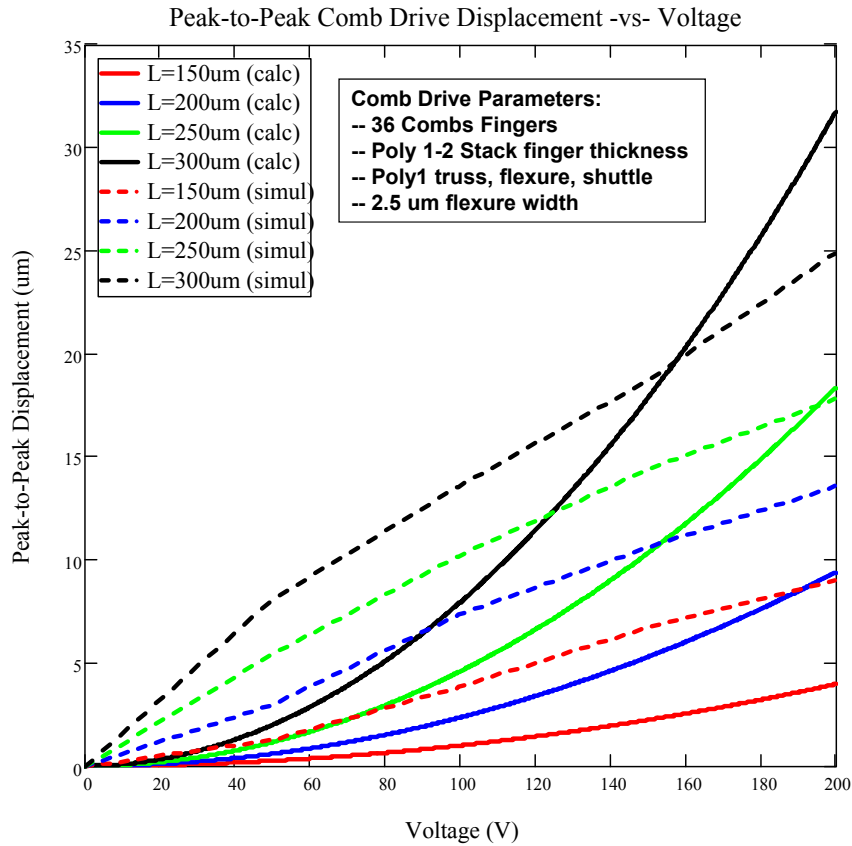


**Figure 60:** Peak-to-peak displacement of comb drive actuator as a function of voltage. The flexure length is varied from 150  $\mu\text{m}$  to 300  $\mu\text{m}$  in 50  $\mu\text{m}$  increments. Increasing the spring length is effective because the displacement is significantly increased while only slightly increasing overall mass.

### 5.3.3 Analysis of Actuator Force

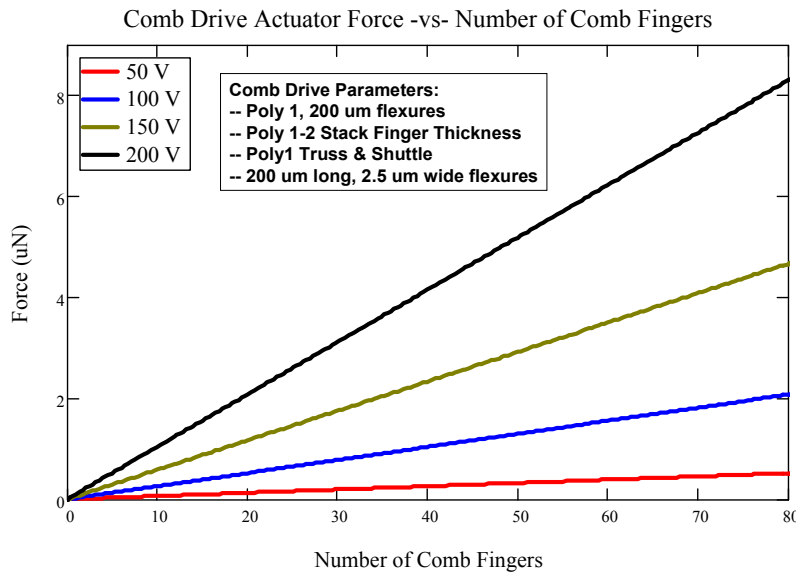
The comb drive actuators should possess enough force to rotate a large master gear at the required frequency. The major force acting against the comb drive actuation is friction. The frictional results used in Lumbantobing’s research (Equation 35) will be utilized to approximate the friction force of the master gear.

Force of the comb drive is largely dependent on the electrostatic force induced by the aggregate capacitance of the inter-digitized comb fingers. The proportion,

$$F_{comb} \propto \frac{nt_P}{h} \quad (N) \quad (44),$$

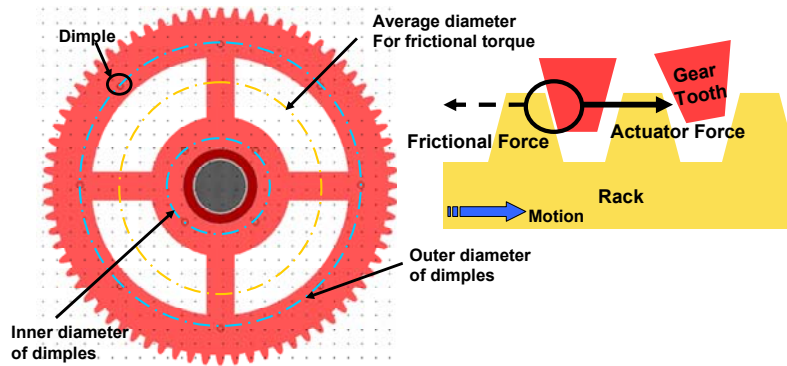
from Equation 23 shows an increase in comb finger pairs, and finger thickness, but minimal capacitive air gap are desired. The finger thickness is maximum using Poly 1-2 stacked, and the air gap is kept at a minimum of 3  $\mu\text{m}$ ; anything less could yield fabrication errors. Therefore, the number of comb finger should be analyzed.

Figure 61 shows the linear relationship of force and the number of comb fingers. Approximately 2-4  $\mu\text{N}$  is available per actuator (for a typical resonator voltage range of 125-175 V) for 36 total comb fingers—the number of comb fingers yielding good frequency performance. Comparing Figure 61 and Figure 55, the engineering trade-off is clear between increasing comb fingers for increased force vice decreasing the fingers for increased frequency.



**Figure 61:** Comb drive actuator force as a function of number of comb fingers. Approximately 4  $\mu\text{N}$  of force is available per actuator for 36 total comb fingers at 200 V.

The frictional force of the gear opposes the actuator force shown in Figure 62. The gear design is comprised of ten dimples—similar to the study conducted by Lumbantobing. The dimples of the master gear were patterned radially of two different diameters as shown in Figure 62. In a similar manner, the resonating parts of the two orthogonal combs drives will rub against the Poly0 surface on dimples.



**Figure 62:** L-Edit drawing of outer and inner diameters containing dimples on the master gear. The average diameter (shown in gold) is used for frictional torque analysis. A simple force diagram of the friction force and actuator force is shown on the right.

Equation 35 is used to calculate the total frictional force acting against the comb drive actuator. The frictional force is largely dependent on the mass of the gear and the wings. The right half of Figure 62 shows a simplified force diagram on the actuator rack. The gear pictured in Figure 62 has a weight of  $0.418 \mu\text{g}$ , and the resonating sections of the orthogonal pair of comb drives weigh  $0.701 \mu\text{g}$ . The two parts create a frictional force of  $1.763 \mu\text{N}$  together. Separating the mass of the gear, wings, and shuttle of Equation 34 and subtracting the frictional force from the actuator force in Equation 23 yields the net available actuator force,  $F_{Net}$ , expressed as

$$F_{Net}(V) = F_E(V) - K \left( \frac{(m_S + m_{gear} + m_{wings})g}{A_C} \right)^{B-1} (m_S + m_{gear} + m_{wings})g \quad (\text{N}) \quad (45)$$

and

$$F_{Net}(V) > 0 \Rightarrow 0 < V \leq 200V \quad (46).$$

The effect of increasing the mass of the wings in Equation 45 on the net available actuator force is shown in Figure 63. As voltage increases, the electrostatic force increases allowing more wing mass to be fabricated above the gear. The x-intercept of each voltage curve of Figure 63 indicates the maximum allowable wing mass; thereafter, the pushing rods of the orthogonal comb drives will stop against the gear teeth. Because the test setup is limited to 200 V, the wing mass should be kept below 12.0  $\mu\text{g}$  per orthogonal comb actuator pair. Figure 63 also shows the voltage required to turn the gear alone without any wing mass attached is roughly 90 V.

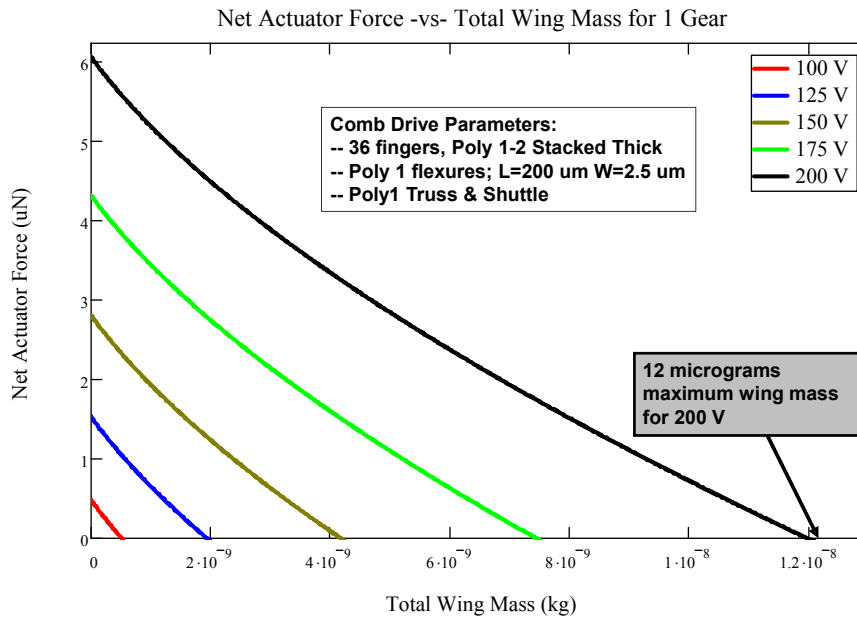


**Figure 63:** Net actuator force as a function of wing mass. The effect of increasing voltage allows for a larger wing mass. The x-intercept indicates the maximum wing mass for a particular voltage. Just less than 100 V is required to turn the master gear alone.



Wing-G and Wing-T wing designs were fabricated in the MUMPs<sup>®</sup> process for attachment to the master gear. Unfortunately, the masses of each wing are substantially more than the 12.0  $\mu\text{g}$  extracted from Figure 63. The weight of Wing-G and Wing-T is 6.1  $\mu\text{g}$  and 2.8  $\mu\text{g}$ , respectively—or 24.7  $\mu\text{g}$  and 14.3  $\mu\text{g}$  per rotor, respectively. Therefore, to increase force the solution is to link comb drive actuators together to add their pushing forces. To do so, adjacent comb drive shuttles are connected so they resonate together. The total force of a multi-linked comb drive actuator is now expressed as

$$F_{comb}(V) = J \frac{\epsilon_0 \epsilon_{air} n t_p}{h} V^2 \quad (\text{N}) \quad (47)$$

where  $J$  is the number of connected comb drive actuators on one side of the orthogonal system. For example, Figure 64 shows a 2-linked orthogonal comb drive where  $J=2$ .

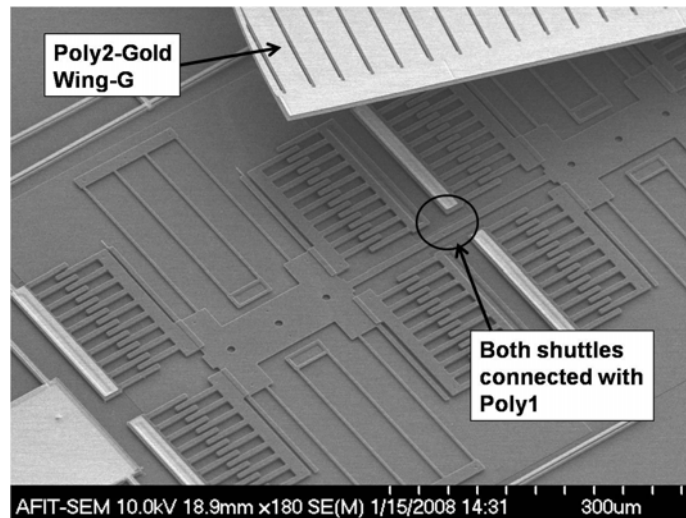


**Figure 64:** Two-linked orthogonal comb drive actuators provide more push force. The pushrods are connected so each shuttle resonates together.

The heavy mass of the rotor is required to be turned using multi-linked comb drives. The net force of the actuators change when multiple comb drives are utilized. Equation 45 is re-expressed as

$$F_{Net}(V) = JF_E(V) - K \left( \frac{(m_{gear} + m_{wings} + 2Jm_s)g}{A_C} \right)^{B-1} (m_{gear} + m_{wings} + 2Jm_s)g \quad (48).$$

Figure 65 shows the net actuator force as a function of voltage for each wing design. Each curve represents a certain number of linked comb drive actuators, and the x-intercept corresponds to the minimum force required to overcome friction of the actuator and master gear without attached wing mass. The key point is more actuating force is required as the wing mass is increased, and more actuating force is achieved by linking comb drives together. Wing-G is heavier; and, for this reason, the 6-linked comb drive begins at 154 V versus the 6-linked Wing-T curve at 137 V shown in Figure 65.

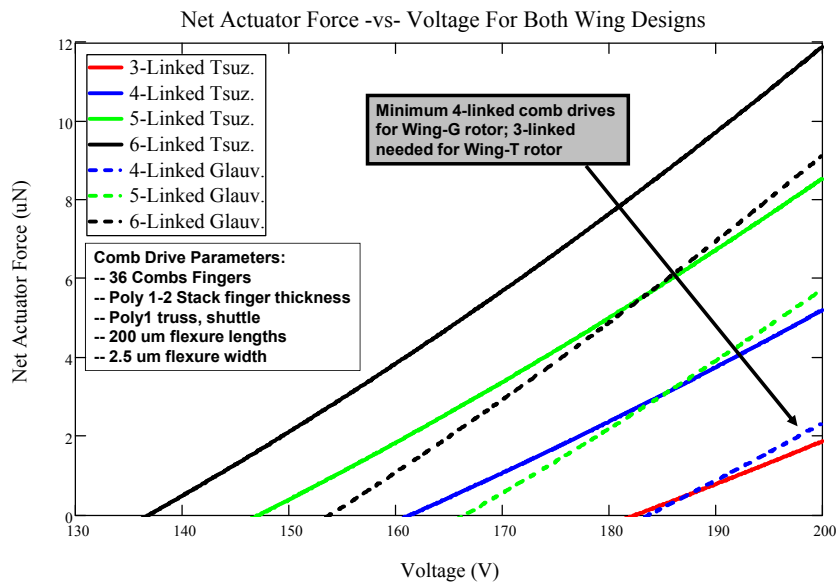


**Figure 65:** Net actuator force as a function of voltage for both Wing-G and Wing-T rotor designs. Four-link actuators are required for the Wing-G rotor while only three are necessary for the Wing-T rotor.

## 5.4 Aerodynamic Feasibility

The weight of the wings, actuators, gear, power supply, assembly parts and substrate mass must be kept minimal to attain sufficient lift. To compare both wing designs, a 5-linked orthogonal comb drive system is analyzed to maintain the required power below 170 V for either design. The wing, gear and resonating comb drive masses are known; so, the remaining mass to allocate as the onboard power supply, substrate and ancillary assembly parts can be analyzed.

The frequency to lift the robot is determined by the gear ratio from the rotational frequency of the rack. The rack is comprised of seven teeth which are spaced out every 10  $\mu\text{m}$ , and the master gear possesses 82 teeth. So, if the  $d_{pp}$  was 10  $\mu\text{m}$  the rack would displace the gear approximately one tooth per cycle. In this case, the gear ratio,  $G$ , would be 82:1. The inevitable engineering trade off is rack rotational frequency for displacement, as the two are inversely proportional.

The remaining mass to allocate to the MEMS chip was analyzed for a range of practical comb drive resonant frequencies. Substituting Miki's thrust equation (Equation 6) and the gear ratio equation (Equation 33) into the robot lift condition equation (Equation 7) and solving for the available mass to allocate to the substrate, power and assembly is expressed as

$$m_{available}(V) = \frac{2\rho_{air}R^3bL_cC_{rw}}{3h} \left( \frac{N_{rack}(V)}{N_{gear}} \pi f_{comb} \right)^2 - (m_{gear} + bm_{wing} + 2Jm_s) \quad (49)$$

where  $N_{gear}$  and  $N_{rack}$  are the number of teeth on the gear and rack, respectively.

Figure 66 shows the relationship of maximum available mass as a function of comb drive frequency. The two wing designs are plotted for various  $C_{rw}$  aerodynamic coefficients, and the difference of changing the coefficient just 0.25 boosts the available mass approximately 100  $\mu\text{g}$  and 50  $\mu\text{g}$ , respectively. The Wing-G rotor design clearly provides more lift but requires more power to rotate.

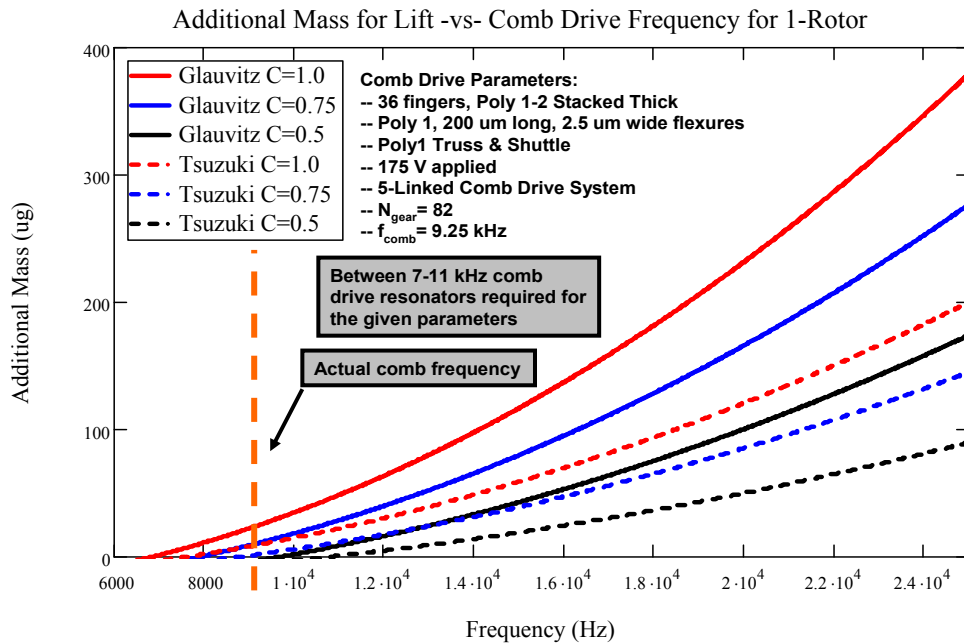


**Figure 66:** Maximum additional mass versus comb drive frequency in order to obtain suitable lift. Both the Glauvitz and Tsuzuki wings are shown at different Miki aerodynamic coefficients. For the configuration shown, between 7-11 kHz resonating frequency is necessary.

Figure 66 was generated using specific comb drive parameters; so, the comb drive frequency was known. Given the parameters, the resonance frequency was 9.25 kHz which falls very low on the curves, and will hardly turn the heavy wing mass. A solution is necessary to preserve the comb frequency while shifting the curves in Figure 66 as far left as possible. Analyzing Equation 49, it is apparent a simple design feature to increase

the robot's maximum available mass is to decrease  $N_{gear}$  which also serves to decrease overall weight.  $N_{rack}$  can be enhanced significantly by designing the comb drive for high displacement (longer, thinner flexures).

However, due to the frequency-displacement trade-off, the design parameters should be carefully weighed. The percent increase of displacement must outweigh the percent decrease of comb frequency. According to Figure 61,  $d_{pp}$  increases linearly for  $n$  comb fingers; whereas, in Figure 55, the comb frequency decreases exponentially for  $n$  comb fingers. However, the frequency decrease is less pronounced when  $n > 36$ ; so, designing the comb resonator for low frequency (LF) and high displacement is best to increase available mass for lift. Doing so, the number of comb fingers and flexure lengths are increased to 60 and 300  $\mu\text{m}$ , respectively. The flexure width is also decreased to 2  $\mu\text{m}$ , and the number of master gear teeth is decreased from 82 to 60. The effect of the low-frequency changes is shown in Figure 67.

The required comb frequency is much lower in Figure 67 (2.98 kHz), but the available mass is nearly 20 times increased compared to Figure 66. The disadvantage is the significantly increased range of displacement requiring of 160  $\mu\text{m}$ . The larger range of motion could pose a problem because the pushrods each would experience deformations of half  $d_{pp}$ —in this case 80  $\mu\text{m}$  if the pushrods are rotating with a constant radius.

A quad-rotor design is best for aerodynamic balance and efficiency as shown by Glauvitz, Chan's MFC and Stanford's Mesicopter [32, 33, 44, 50]. A quad-rotor design implements four rotors in each quadrant of a square substrate. For aerodynamic balance,

no two adjacent rotors rotate in the same direction. Further, because of the balanced design, two adjacent rotors can share the linked comb drives between them. The sharing configuration is similar to a push-pull or engage-disengage setup suggested by Glauvitz and shown in Figure 17. The sharing decreases the overall mass of the combs by a factor of two, and utilizing four rotors quadruples the thrust force. Equation 42 is modified as

$$m_{available}(V) = \frac{8\rho_{air}R^3bL_C C_{rw}}{3g} \left( \frac{N_{rack}(V)}{N_{gear}} \pi f_{comb} \right)^2 - 4(m_{gear} + bm_{wing} + Jm_S) \quad (50).$$

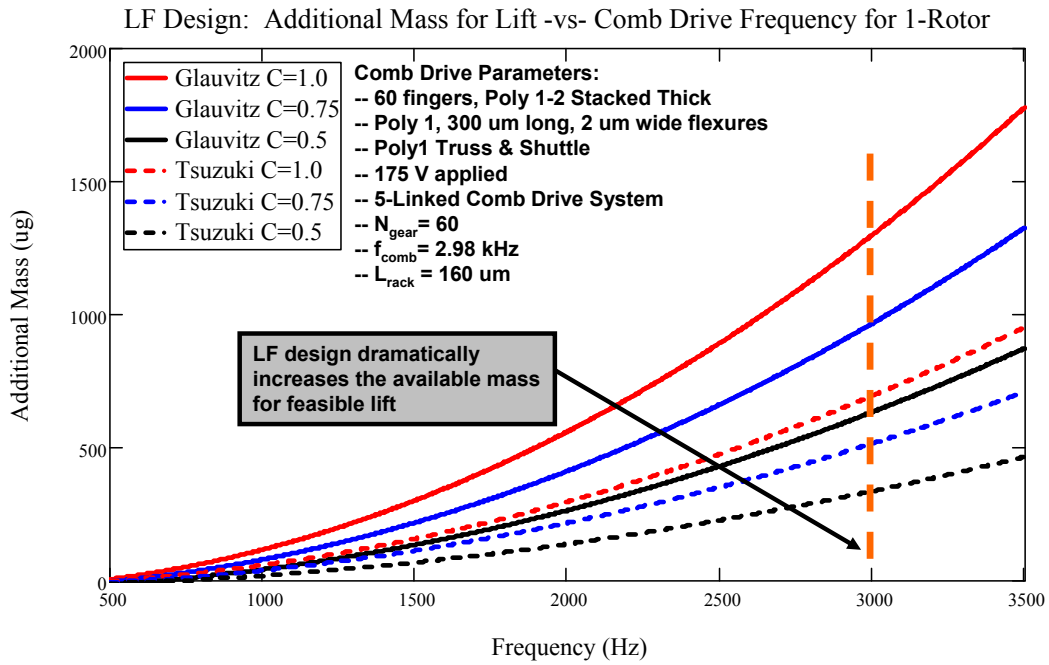


**Figure 67:** Additional mass available to produce lift versus required comb drive frequency. Decreasing the master gear size and teeth, increasing comb fingers above 36, and decreasing the spring constant is the optimum comb design.

Figure 68 shows the leftover mass to allocate for substrate, power and assembly as a function of comb drive frequency for the quad-rotor. As expected, the additional mass values are four-fold that of Figure 67 without modifying the resonating frequency.

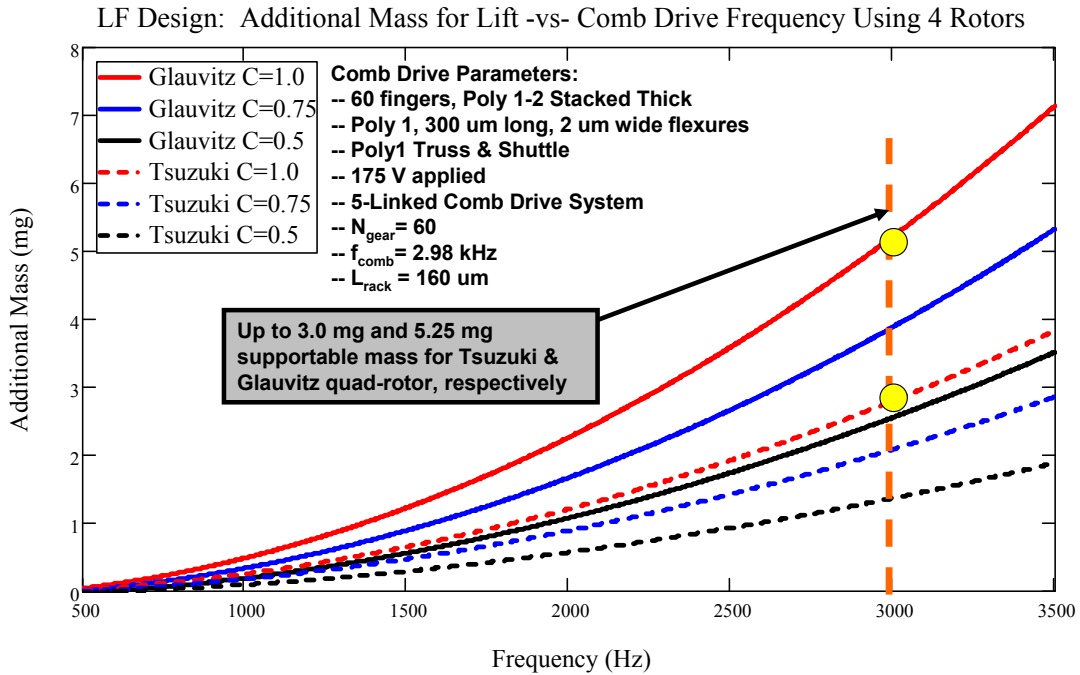


**Figure 68:** Maximum additional mass versus comb drive frequency in order to obtain suitable lift for the quad-rotor design. Both the Glauvitz and Tsuzuki wings are shown at different Miki aerodynamic coefficients. For the configuration shown, up to 3.0 mg and 5.25 mg could be supported using the Tsuzuki and Glauvitz rotors, respectively.

## 5.5 Power Requirements

A quad-rotor design is made of four multiple-link orthogonal comb drives shared between four rotors. Each corner of a square quad-rotor chip is driven by a  $Y$ -linked orthogonal comb drive pair, where  $Y$  is the number of linked comb drives resonating as one large shuttle. Therefore, the MEMS robot will possess two  $Y$ -linked orthogonal comb drive pairs (each pair is shared between two rotors).

For power analysis, each  $Y$ -linked comb drive will be treated as one large resonating shuttle with  $Y$  times the push force, spring force and mass. The resistance of each  $Y$ -linked comb drive resonator is re-expressed as

$$R_y = \frac{\sqrt{k_s m^*}}{YQ\eta_r^2} \quad (\Omega) \quad (51),$$

and each of the four sides of a  $Y$ -linked comb drive is connected in parallel. The equivalent resistance,  $R_{eq}$  is expressed as

$$R_{eq} = \frac{R_y}{4} \quad (\Omega) \quad (52),$$

and the corresponding average sinusoidal power requirement,  $P_{comb}$ , for actuating all of the comb drives is expressed as

$$P_{comb} = \frac{V^2}{2R_{eq}} \quad (W) \quad (53).$$

Figure 69 shows representative power requirements for the given comb drive parameters.

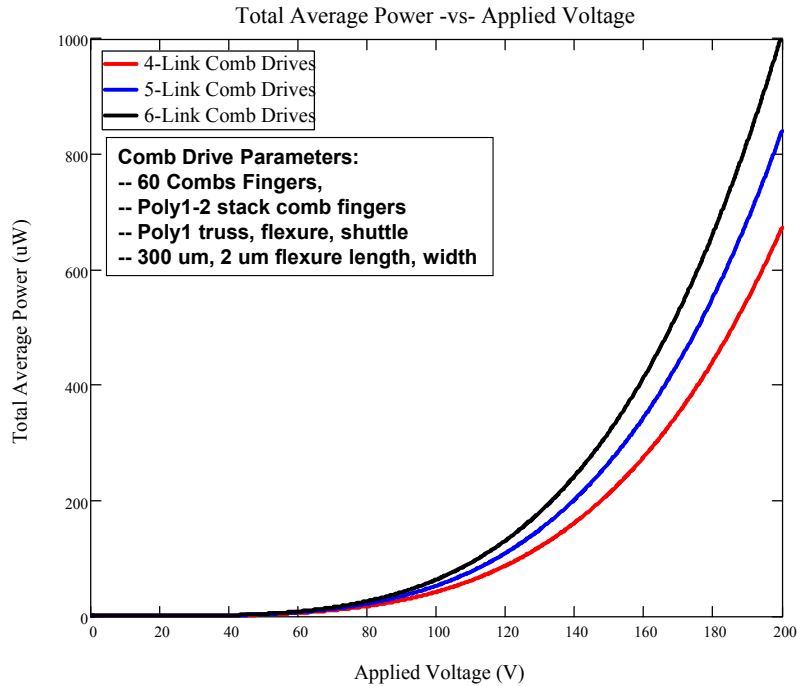


**Figure 69:** Average power versus applied voltage for quad-rotor flying robot employing 4, 5 and 6-linked orthogonal comb drive actuators.



The power requirement significantly increases for voltages greater than 120 V. In the normal operating range of 150-200 V, the flying MEMS robot will consume 0.2-1.0 mW of power.

## 5.6 Chapter Summary

This chapter presented modeling and analysis of MEMS theory toward a flying MEMS robot. The frequency and displacement of the comb drive actuator were modeled and in close agreement of analytical values. Utilizing the MEMS research of Miki and Lumbantobing, analytical expressions were formulated for available mass to allocate to the robot. A summary of a feasible rotary-wing MEMS robot design for both wing designs is presented in Table 13. The next chapter summarizes the empirical data and laboratory testing performed during this thesis.

**Table 13:** Summary of key parameters for a feasible rotary-wing MEMS robot design.

<i>Parameter</i>		<i>Wing-G</i>	<i>Wing-T</i>
Poly2-Gold wings	No. rotor wings	4	5
	Angle of attack (deg)	15-20	15-20
Poly 1 comb drive actuators	Interdigitized comb fingers	60	60
	Flexure length/width ( $\mu\text{m}$ )	300/2	300/2
	Peak displacement ( $\mu\text{m}$ )	165	165
	Resonance frequency (kHz)	2.98	2.98
	No. linked comb drives per rotor	6	5
Shaft	Minimum height ( $\mu\text{m}$ )	139.8-184.7	64.7-85.5
	No. Collars	29-39	13-18
Poly 1 gears	Rack length ( $\mu\text{m}$ )	165	165
	No. master gear teeth	60	60
Power	Power for 150-200 V operation (mW)	0.3-1.0	0.25-0.85
Mass	Quad-rotor available mass (mg)	3.0-5.25	1.0-3.0

## **VI. Experimental Tests and Results**

### **6.1 Chapter Overview**

This chapter presents the experimental results of the wings and actuators. The wings were measured for deflection and compared to simulated and analytical data. An attempt was also made to create a suitable 15-20° wing pitch angle using both photoresist and Crystalbond™. Comb drives actuators were characterized and compared to simulated and analytical data. The rotary actuation of orthogonal comb drives was characterized, and wing rotation using backup orthogonal thermal actuators is discussed.

### **6.2 Chip Release**

Each MEMS chip was released of sacrificial oxide and dried prior to testing. The sacrificial layer oxide is etched in HF, and the chips are dried either in a critical point carbon dioxide (CO<sub>2</sub>) dryer or on a hot plate. The drying process is critical because stiction, resulting from residual moisture, is one of the most common MEMS failure mechanisms. The CO<sub>2</sub> dryer automatically controls the temperature, pressure and humidity; whereas, the hot plate method is volatile and sometimes unreliable. Figure 70 shows a detailed analysis of the MEMS sacrificial oxide release process, and Table 14 summarizes the CO<sub>2</sub> dryer oxide release procedure performed at AFIT.

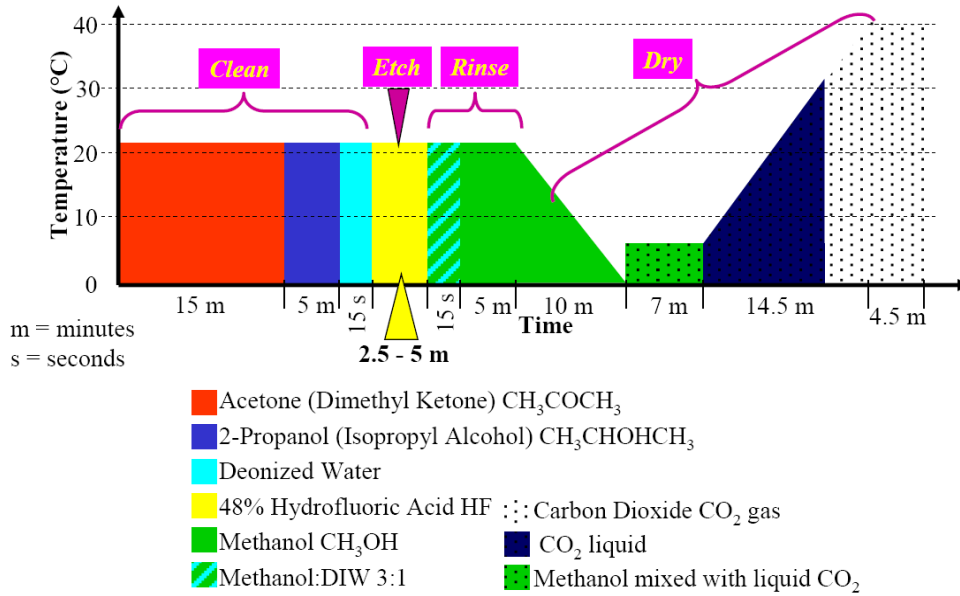


**Figure 70:** Detailed time versus temperature diagram of the MEMS oxide release process [77].

**Table 14:** Procedure for releasing and  $\text{CO}_2$  drying the MEMS chips.

<i>Step</i>	<i>Time</i>
1. Agitate chip in acetone	2-4 min
2. Submerge in second acetone	15-20 min
3. Submerge in HF	3-5 min
4. Rinse in methanol	5-10 min
5. Submerge in second methanol	10-15 min
6. Transfer chips to $\text{CO}_2$ dryer with methanol	30-40 min to dry

## 6.2 Wing Deflection

### 6.2.1 Residual Stress Deflection

The vertical wing deflection induced by residual stress is shown in Figure 71 and Figure 72. Figure 72 also shows the Wing-T rotor is fully released of oxide because the wings rotated from their respective Poly1 spacer. The vertical deflections were measured under a Zygo IFM and compared to the simulated and analytical results in Section 5.2.2.

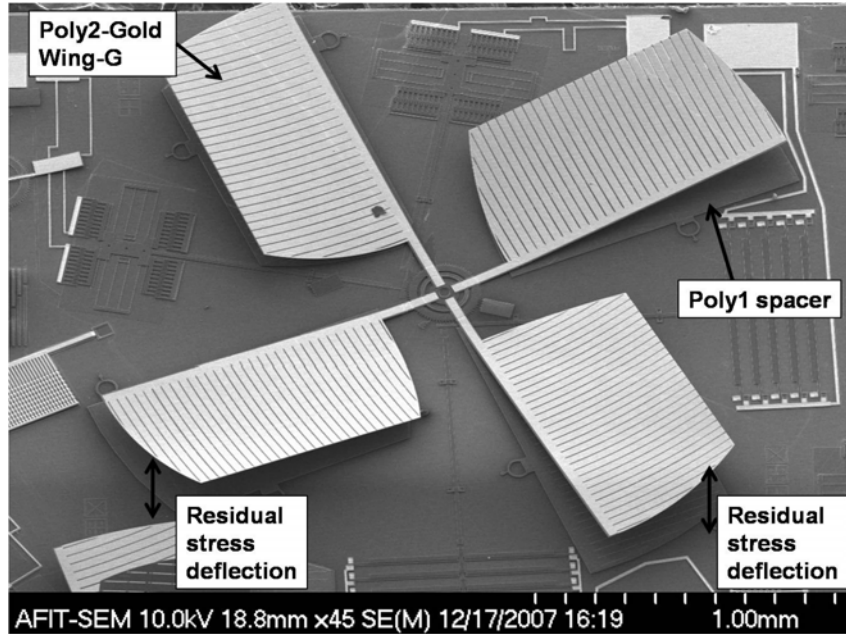


**Figure 71:** Post-release SEM picture of the Wing-G quad-rotor. The picture clearly shows the vertical wing deflection.

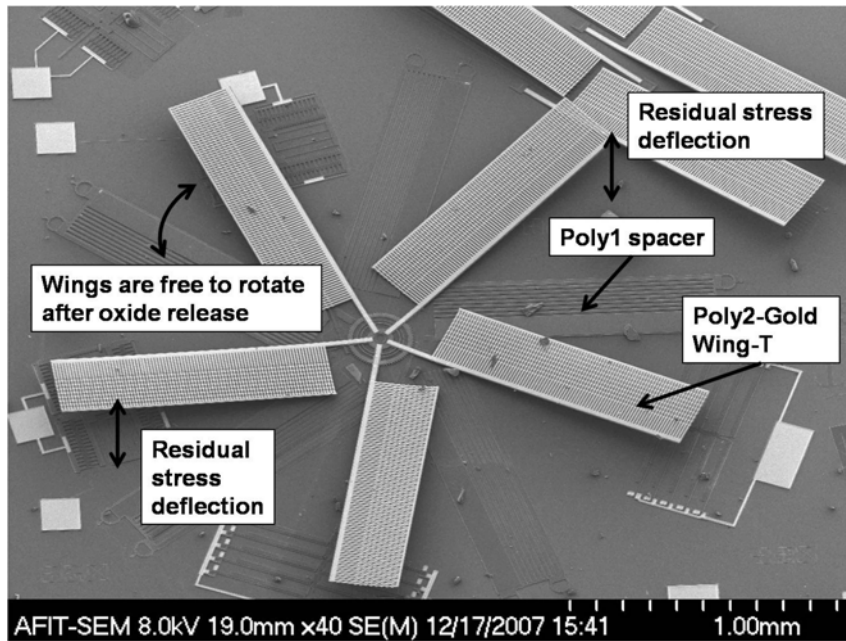


**Figure 72:** Post-release SEM picture of the Wing-T 5-wing rotor. The picture clearly shows vertical wing deflection. The capability of the gear and wings to rotate about the gear hub confirms the chip was fully released.

The Zygo IFM scans devices vertically and utilizes differences in optical diffraction to calculate deflection. Figure 73 and Figure 74 show the LE deflection of Wing-G and Wing -T, respectively. Both wings deflected linearly to approximately 100  $\mu\text{m}$ .

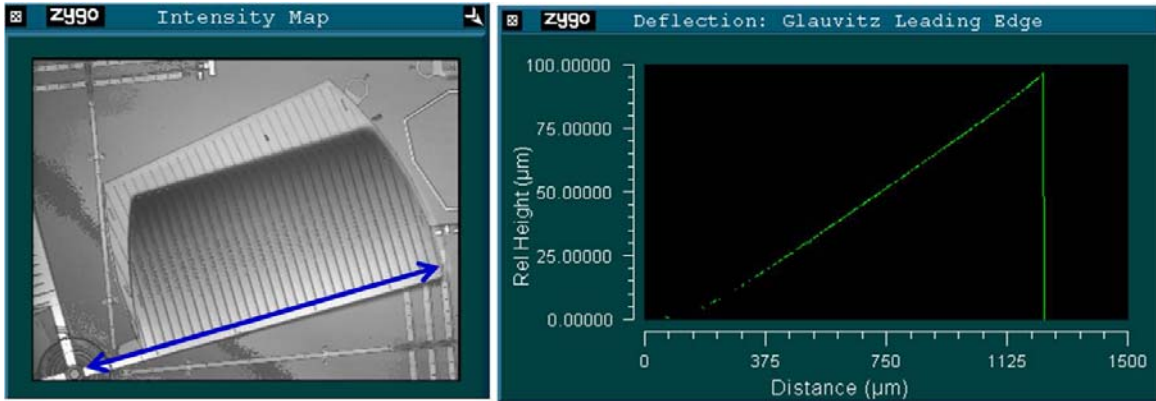


**Figure 73:** Zygo IFM scan showing vertical deflection of the Wing-G leading edge (blue line). The leading edge deflected approximately 100  $\mu\text{m}$ .

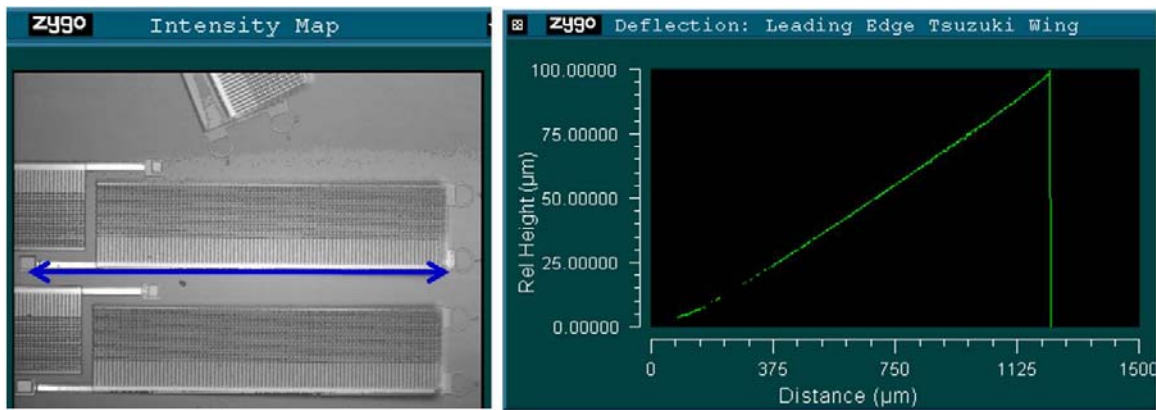


**Figure 74:** Zygo IFM scan showing vertical deflection of the Wing-T leading edge (blue line). The leading edge deflected approximately 100  $\mu\text{m}$ .

Figure 75 and Figure 76 show the empirical deflections compared to the calculated and modeled data. The measured data for Wing-G appeared linear just as the modeled data. The near-linear deflection confirms the calculated deflection does not

account for the variable moment of inertia and large wing mass. Likewise, Wing-T was predicted to follow the modeled parabolic deflection; however, the measured data was flat and near-linear.

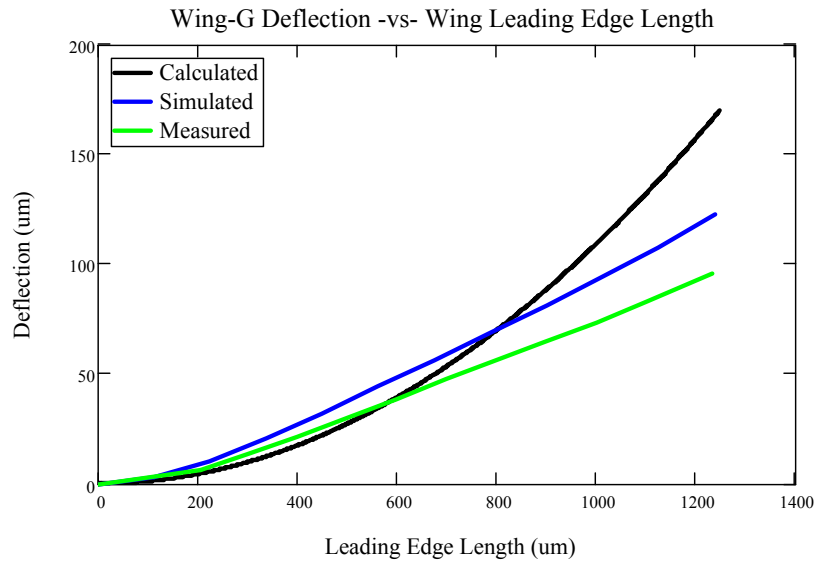


**Figure 75:** Wing-G empirical data compared to calculated and simulated deflection. The measured data closely resembles the modeled data.



**Figure 76:** Wing-T empirical data compared to calculated and simulated deflection. The measured data closely resembles calculated and modeled data up to 0.5 mm.

SEM pictures were taken to investigate the reason for the flat deflection shown in Figure 76. The corrugation appeared to affect the evaporation of gold in the MUMPs<sup>®</sup> process. Illustrated in Figure 77, the corrugation trenches created steep sidewalls leading to disconnected gold pieces. The individual pieces, as opposed to long gold strips, likely inhibited the leading edge deflection.

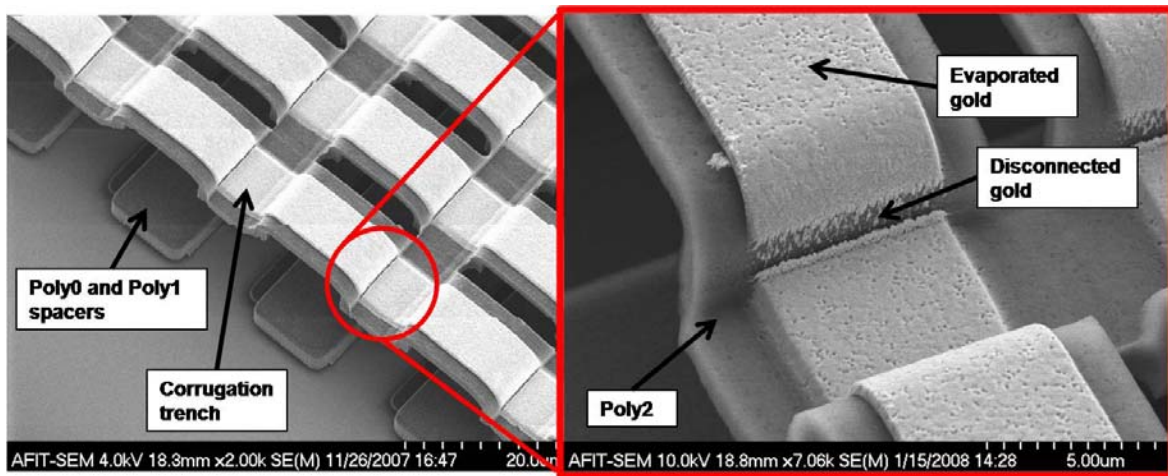


**Figure 77:** SEM picture of Wing-T corrugation. The evaporated gold was likely the cause of the lower deflections compared to calculated and simulated results.

The deflection of the chord was also measured using the IFM. The chord of Wing-T deflected despite the disconnected gold segments shown in Figure 78; the total deflection was  $11.5 \mu\text{m}$  over the  $250 \mu\text{m}$  chord—closely matching the simulated  $8 \mu\text{m}$ . The deflection of the Wing-G chord was out-of-scope for the IFM due to the steep deflection outward at the chord tip. However, since the chord closely resembles a simple cantilever, the modeled data of  $48 \mu\text{m}$  can be used as an approximation. The maximum empirical wing deflections were  $144.7 \mu\text{m}$  and  $109.7 \mu\text{m}$  for Wing-G and Wing-T, respectively. Wing-G was just 9.6% less than the modeled maximum deflection.

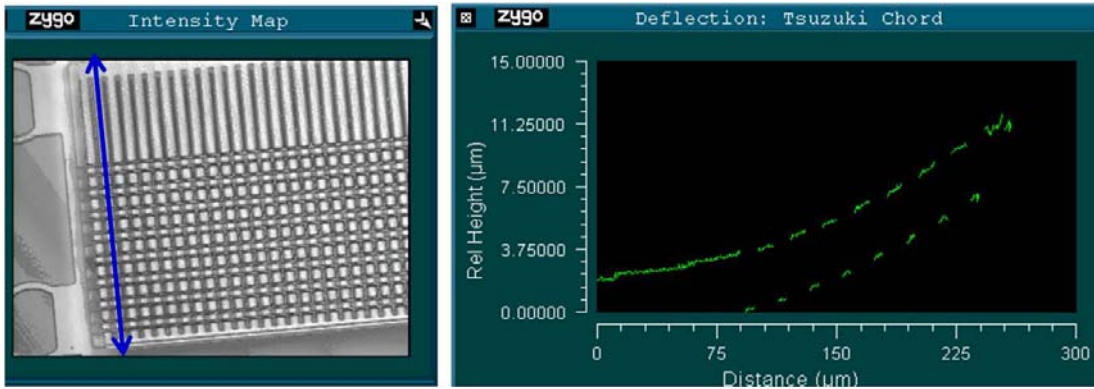


**Figure 78:** Screenshot of deflection of the Wing-T chord measured on the Zygo IFM (blue line). The corrugation is shown to the right, and the total deflection was approximately 11.5  $\mu\text{m}$ .

The use of spacers under the wings was moderately successful. The wing was kept straight as evident by Figure 73 and Figure 74, but Poly2 seeped between the gear teeth. With insufficient wing deflection, this feature will cause the comb drive rack teeth to skip or become caught under the wing where the teeth would mesh. The deflection was checked with the SEM and confirmed the Poly2 wing covered the gear teeth shown in Figure 79.

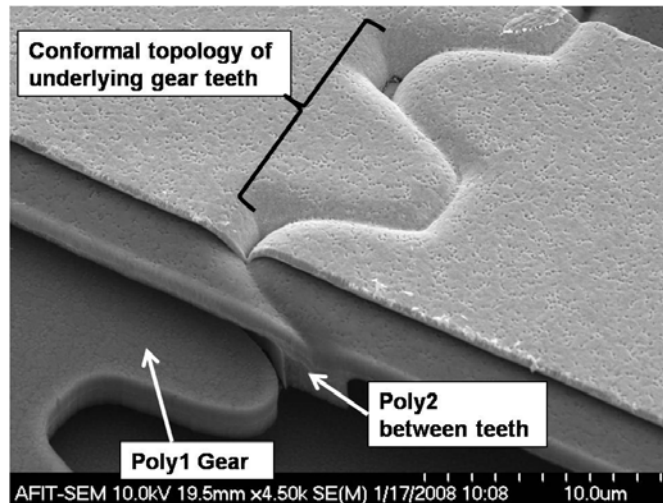


**Figure 79:** SEM picture showing the undesired Poly2 which seeped between the Poly1 gear teeth. The deflection was insufficient to lift the wing above the gear.



### **6.2.2 Wing Hinge**

The 15-20° required pitch angle of the chord is not possible using the residual stress of Poly2/Gold. Therefore the chord requires to be assembled at this angle. Glauvitz attempted using Shipley 1818 photoresist to create the pitch angle, but the overlaying oxide required etching to expose the polysilicon. This thesis work re-attempted the photoresist hinge since the sacrificial oxide of Wing-G and Wing-T was beneath the polysilicon.

A mask was designed to create the photoresist pattern and is shown in Appendix D. Shipley 1818 photoresist was applied to the wings at 4000 RPM for 30 sec for a thickness of 1.8  $\mu\text{m}$ . After baking for 75 sec, the chip was placed under an EVG620 Mask Aligner with a dose of 120  $\text{mJ}/\text{cm}^2$  using a 500 W mercury lamp. Following exposure, the chip was developed in 351 solution for 30 sec, rinsed in deionized water (DIW) for 30 sec, and baked at 110 °C for 2 min on a hot plate. Figure 80a shows the results of these steps.

To release the oxide and observe the deflection, the chip was released and dried using the hot plate method. The chip was submerged in 48 % HF and rinsed in DIW and isopropyl alcohol each for 10 min before drying on the hot plate for 15 min at 110 °C. Figure 80b shows the resist dissolved during the release. The resist did not adhere to the gold layer. Most likely, the width of the resist strip was too thin, and the mask design should have utilized 2-3 times wider patterns for better adhesion to the gold. Another reason may be due to overexposure; decreasing the exposure dose to 60-100  $\text{mJ}/\text{cm}^2$  may yield better results.

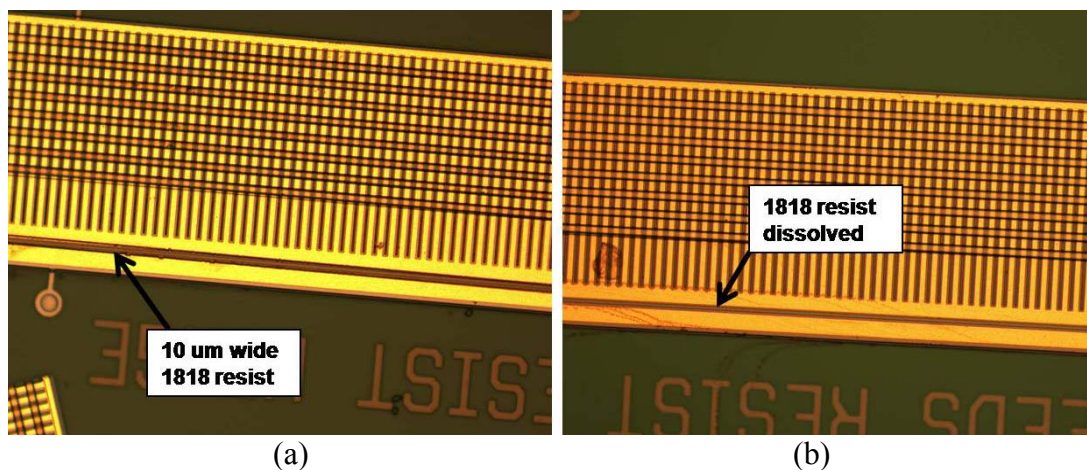


**Figure 80:** (a) Photoresist pattern after 120 mJ/cm<sup>2</sup> dose exposure, 30 sec of 351 developing, and 2 min hot plate bake. (b) The photoresist dissolved after releasing the oxide in HF for 3.5 min and dissolving in DIW and isopropyl alcohol each for 10 min.

Another attempt used Crystalbond<sup>TM</sup> multi-purpose wafer bonding adhesive. Crystalbond<sup>TM</sup> is a clear solid at room temperature, which softens to a liquid at 120 °C and is resistant to HF. Prior to applying the adhesive, the chips were agitated and soaked in acetone for 15 minutes, submerged in methanol for 5 minutes, and dried with nitrogen gas and hot plate for 2 minutes at 110 °C. The Crystalbond<sup>TM</sup> was applied manually with fine point tweezers using optics from a wire bond machine and a heated stage at 120 °C. This task required high precision but was practical. Figure 81a shows a top view of the MEMS chip with Crystalbond<sup>TM</sup> applied, and Figure 81b shows the Crystalbond<sup>TM</sup> successfully bonding the wing's chord to the spar.

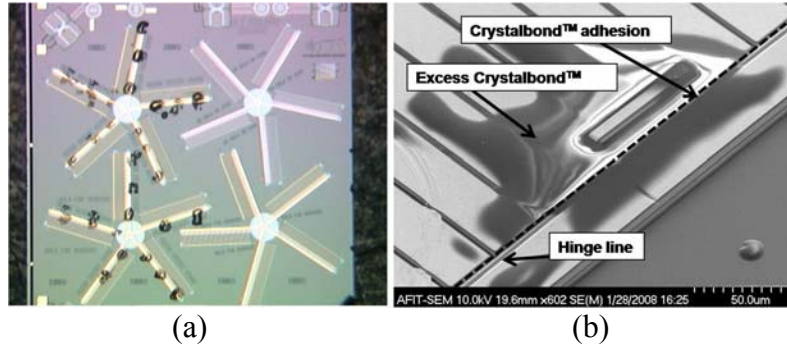


**Figure 81:** (a) Top view of MUMPs<sup>®</sup> 80 chip with Crystalbond<sup>™</sup> attachments on two Wing-T rotors, and (b) SEM picture of Crystalbond<sup>™</sup> successfully bonding the hinge.

The MEMS chips were released in HF for 3.5 min and dried using the hot plate method. The hot plate process requires chips to be submerged in DIW and isopropyl alcohol each for 10 minutes immediately after etching in HF. The chips were then set on a hot plate for 10-15 min at 110°C which fully dried the chip and reflowed the Crystalbond<sup>™</sup>.

The Crystalbond<sup>™</sup> successfully created a hinge, but the resulting deflection of the wing was not increased beyond the residual stress deflection. One possible reason for the deficient deflection was applying the Crystalbond<sup>™</sup> while it was softened; precisely placing small solid pieces and reflowing naturally could provide better adhesion properties and higher surface tension. Future work should also consider solder spheres of 25-75 μm diameter and 62Sn/36Pb/2Ag composition with low-melting point of 179°C. The weight of one solder sphere in this range is 0.07-1.86 μg. Assuming two spheres per wing, a total of 0.55-14.9 μg and 0.7-18.6 μg of additional chip mass is obtained using the Wing-G and Wing-T designs, respectively. Solder spheres were successfully reported by Linderman, *et al* in the development of a micro-rotary fan with angled fan blades [93].

### 6.3 Comb Drive Actuation

#### 6.3.1 Comb Drive Resonator

Various comb drive designs were fabricated to compare frequency and displacement to simulated and analytical data. A 100 V sine wave was applied to one side of the comb fingers, and a frequency sweep was utilized to hone in the peak resonant frequency. All the comb resonators were fabricated of 36 stacked Poly1-2 comb fingers and either Poly1 or Poly1-2 stack shuttle. Several comb drive resonators were tested, and representative analytical, simulated and empirical data is shown in Figure 82.

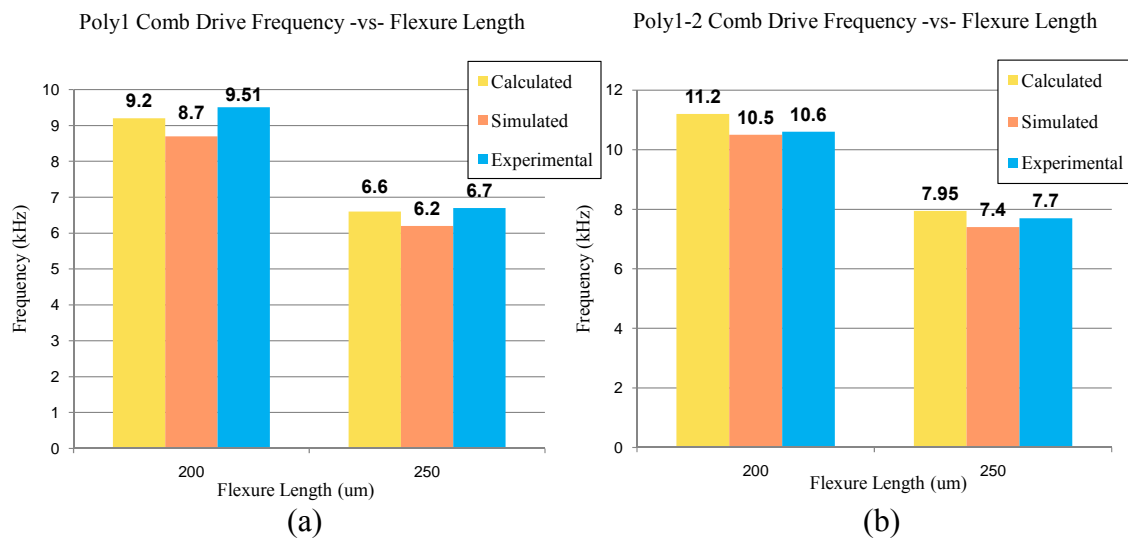


**Figure 82:** Calculated, simulated and experimental comb drive frequencies versus flexure length for (a) Poly1 and (b) Poly1-2 shuttle. The comb drives have 36 interdigitized fingers with a thickness of 3.5  $\mu\text{m}$  (stacked Poly1-2).

Figure 83 shows representative comb drive displacement at 100 V. The displacement could not be precisely measured, but using known sizes of geometric features, the displacement was estimated to be 15  $\mu\text{m}$  and 28  $\mu\text{m}$  for 200  $\mu\text{m}$  and 250  $\mu\text{m}$  flexures, respectively. The higher displacement of Figure 83 compared to Figure 60 is

attributed to the fabrication process and HF sacrificial oxide release. The sacrificial oxide release also can slowly thin the flexures at an extremely slow etch rate. The thinning is often negligible of larger devices, but a change of just  $0.1\ \mu\text{m}$  of a  $2\ \mu\text{m} \times 2\ \mu\text{m}$  flexure can drastically affect the spring constant and resulting deflection. Nevertheless, the  $50\ \mu\text{m}$  increase in length yielded roughly double the displacement which is clearly shown by Figure 60.

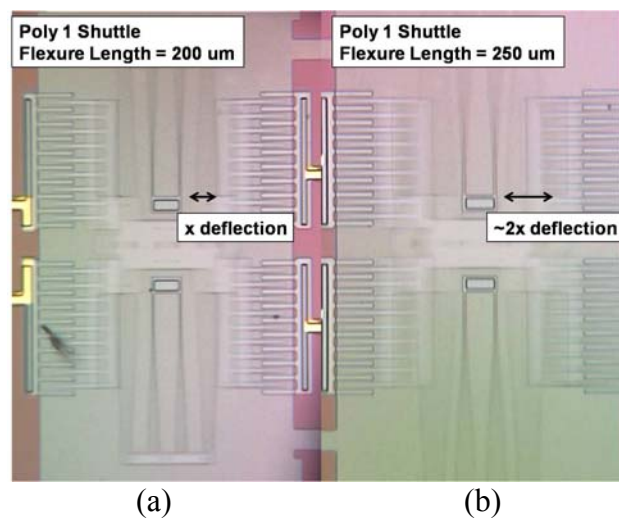


**Figure 83:** At 100 V, twice as much deflection was observed by lengthening the flexure lengths from (a)  $200\ \mu\text{m}$  to (b)  $250\ \mu\text{m}$  as predicted by simulated and analytical models.

### 6.3.2 Orthogonal Comb Drives

Rotary actuation was possible using two identical electronic signals at the system's resonance frequency which have a phase angle difference near  $90^\circ$ . The pushrod perpendicular to the rack acts as the clutch to engage and disengage the rack, and the pushrod in-plane with the rack is the pusher. Figure 84 shows how the two (2) signals interact to rotate the gear. Figure 85 shows the laboratory test setup to obtain the desired signals.

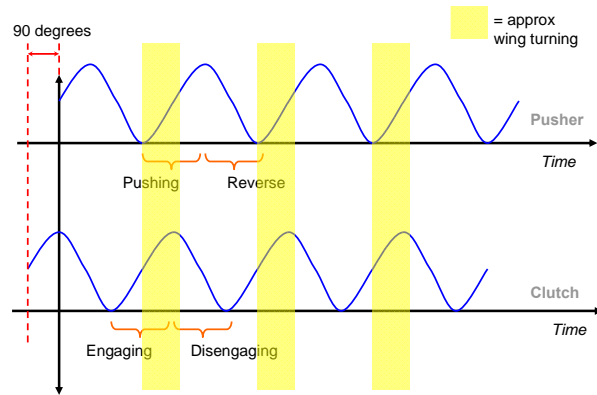


**Figure 84:** Electric signals for the orthogonal comb drive actuation scheme have a 90° phase angle difference. The shaded yellow section corresponds to the time period the teeth are engaged and turning the rotary wings.

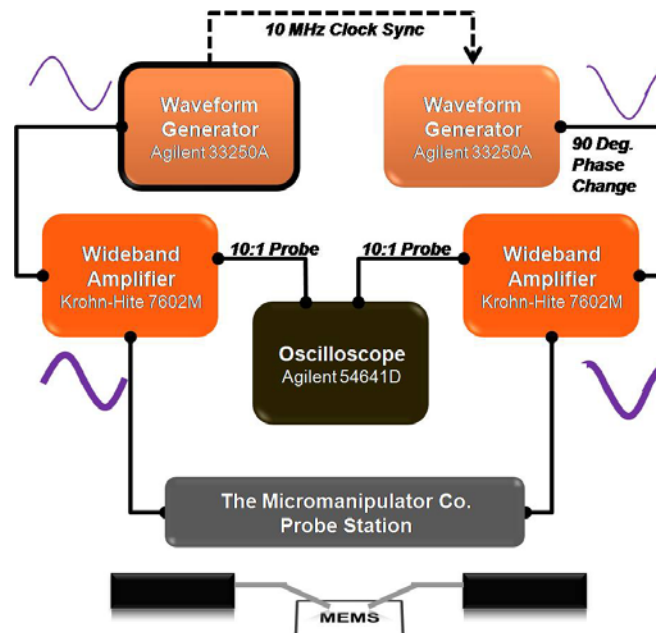


**Figure 85:** Laboratory test setup to obtain two amplified oscillating signals with a difference in phase angle.

The orthogonal comb drive was capable of rotating a gear successfully and an example is shown in Figure 86. The actuators response was sensitive to the DC offset of the wideband amplifier and the phase angle difference of the two waveform generators.

The output of both parameters was viewed by the oscilloscope. As the voltage was increased, the DC offset required constant readjustment so the minimum voltage of each sine wave coincided with 0 V (ground). The phase angle difference was observed to work for a range of 75 – 105° and did not appear consistent for identical devices.

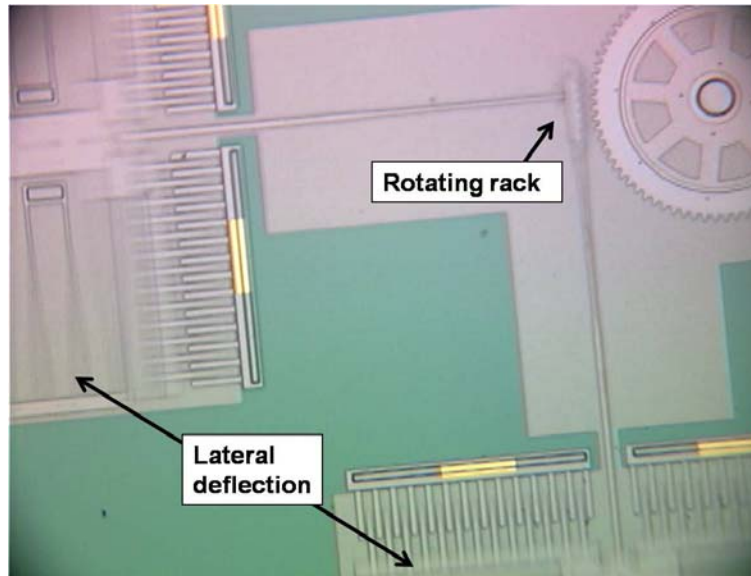


**Figure 86:** Screenshot of the lateral deflecting comb drives resulting in rotational actuation of the rack. The comb drives are comprised of a Poly1 shuttle and 52 shuttle teeth which resonated at 7.7 kHz.

The design concept was successful but allowed only intermittent rotation. Poly0 was placed under the entire actuator, but was omitted in the wire runs. Incorporating Poly0 is significant in order to avoid breaching the electrically isolating silicon nitride layer. The Poly1-2 wire runs in this design consisted of Anchor1 to connect Poly1 to the substrate and Poly1-2 Via to join Poly1 and Poly2; the two oxide etches are enough to breach the nitride according to the design rules of PolyMUMPs® [78]. At voltage ranges of 100-200 V, the comb shuttles would occasionally become completely stuck to the

underlying Poly0 ground electrode. This is evident of a nitride breach because an undesirable capacitor is formed as illustrated in Figure 87.

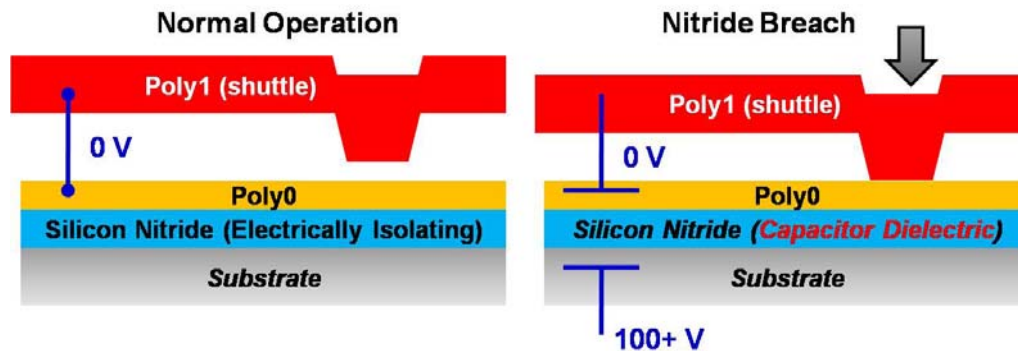


**Figure 87:** The poly1 shuttle becomes attracted to the substrate when a nitride breach occurs. In this case, the substrate is biased to the applied voltage, and the nitride serves as a dielectric between two different voltage potentials forming a capacitor.

A few other design flaws are worth mentioning. In some cases, the wires were too close to the deflecting shuttle resulting in damaging electrical shorts as shown in Figure 88a. Positioning the comb drives away from the edge of the MEMS chip would alleviate this problem. Another repeatable problem was the clutch arm attachment to the rotating rack. The clutch arm typically broke from the rack for voltages greater than 100 V and for instantaneous voltage surges below 100 V (such as turning ON/OFF with ON set to 80 V) shown in Figure 88b. The cross sectional area of the attachment is  $8 \mu\text{m}^2$  and should be increased in future designs. Fortunately, the rack remained oscillating even with the clutch disconnected.



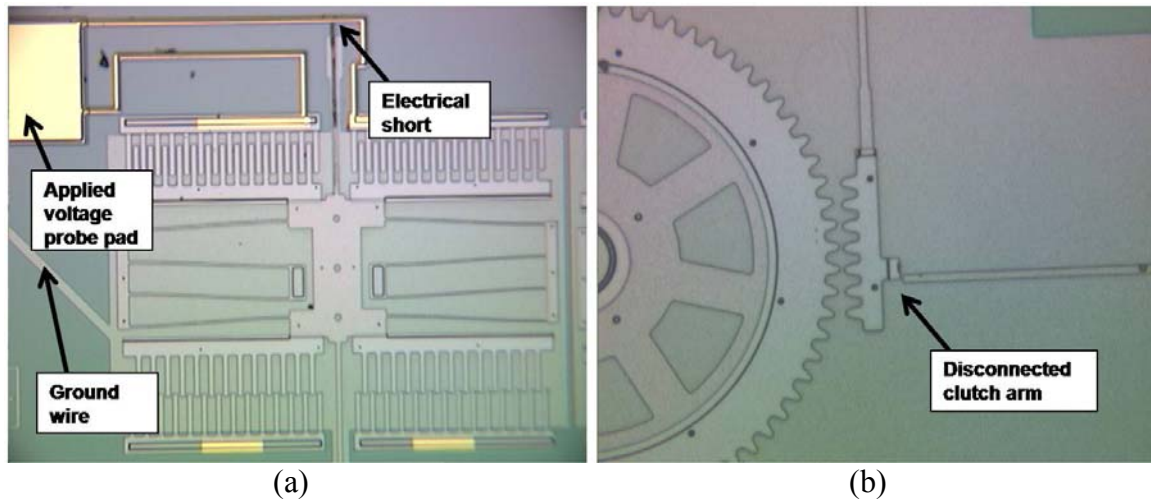


**Figure 88:** (a) An electrical short occurred because the balancing shuttle arm deflected and touched the high voltage wire, and (b) the clutch arm typically breaks from the rack at higher voltages.

### 6.3.2 *Wing Rotation*

As presented in Section 5.3, up to 6 connected comb drives are required to turn the wings designed in this research. Unfortunately, only 2-linked orthogonal comb drive actuators were fabricated due to lack of space on the chip. However, thermal actuators were fabricated to rotate the wings to demonstrate proof-of-concept rotation. According to Figure 33 and Figure 34, thermal actuators contribute high force—sufficient to overcome the weight of the gear and wings (but not to create sufficient thrust because they are not fast enough).

The thermal actuators are arranged orthogonally and are comprised of individually connected single hot-arms actuators shown in Figure 35. Half of the orthogonal thermal actuators are shown in Figure 89. The complete orthogonal actuator is viewable near the bottom right corner of Figure 71 and Figure 72. The test setup was

identical to that of Figure 85 except two square wave DC signals were used and approximately 90° out-of-phase.

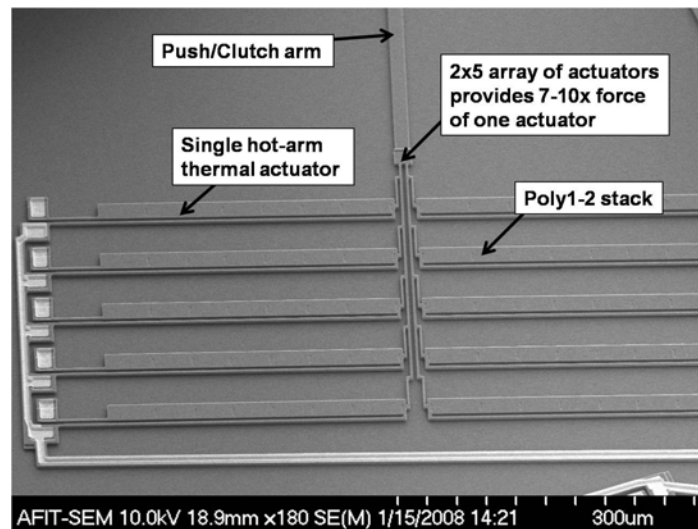
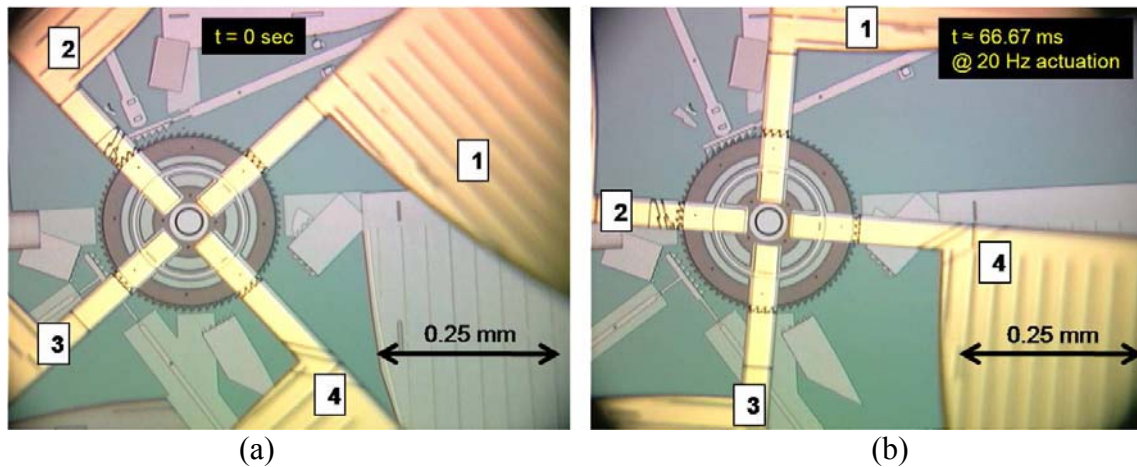


**Figure 89:** SEM of a 2x5 thermal actuator array with high force output to rotate wings. The array was created as a proof-of-concept rotary actuator because a 6-link orthogonal comb drive actuator was not fabricated.

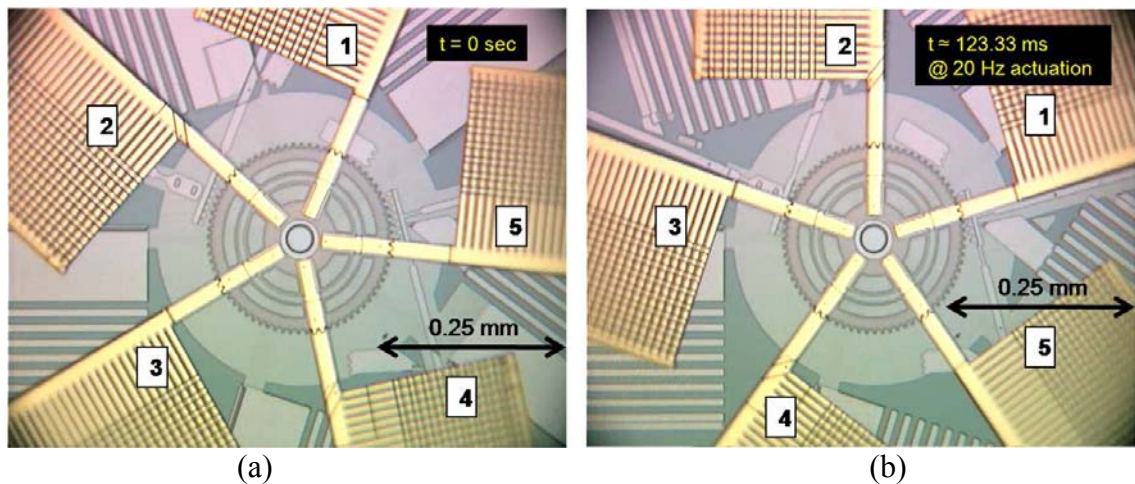
As with the orthogonal comb drive, the actuation cycle was very sensitive to the DC offset and phase angle difference. The thermal actuators were driven to a voltage range of 10-13 V. The thermal actuators would fail at approximately 16 V where the thermal effects plastically deformed and burned the hot arms.

Figure 90 shows successful rotation of the Wing-G rotor. The orthogonal thermal actuators were driven by a 12 V, 20 Hz DC square wave with an approximate 90° phase angle difference. The wings rotated approximately 40° in 66.67 ms. Similarly, the Wing-T rotor was rotated the same angle in approximately 123.33 ms shown in Figure 91. Note the time and angle approximations were made by studying the frame rates which is highly imprecise. Overall, the rotation of both rotors was erratic because it was

difficult to dial in the precise DC offset on the analog amplifier. The slightest touch of the DC offset knob was capable of completely changing the actuation cycle.



**Figure 90:** (a) At  $t=0$  sec, a 20 Hz, 12 V actuation cycle is applied to the Wing-G rotor, and (b) the rotor rotates approximately 40 deg in one frame segment 66.67 ms.



**Figure 91:** (a) At  $t=0$  sec, a 20 Hz, 12 V actuation cycle is applied to the Wing-T rotor, and (b) the rotor rotates approximately 40 deg in two frame segments of 123.33 ms.

For both rotor designs, the actuator rack typically became caught in the teeth beneath each wing. When this occurred, the rack vibrated continuously against the Poly2

which seeped between the Poly1 gear teeth addressed in Figure 79. Figure 92 shows the actuator stuck on the interfering Poly2 wing.

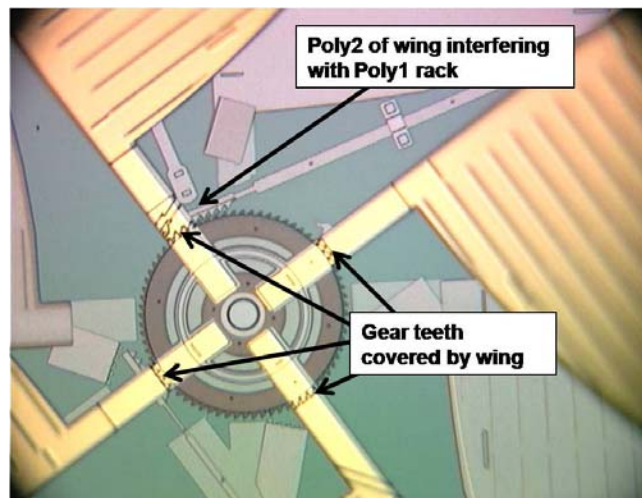


**Figure 92:** The Poly2 wing interferes with the Poly1 actuator rack. The rack intermittently gets stuck in the Poly2 covered gear teeth as shown in the picture.

#### 6.4 Robot Assembly

Parts of the MEMS flying robot were designed for flip chip assembly. The shaft section, top shaft section, and wing rotor are shown in Figure 93. The shaft section was designed to fit around the Poly2 hub which held the Poly1 master gear in place. However, if utilizing a Poly1 master gear a partial HF oxide etch is required to remove Oxide2 covering Poly1. The shaft section assembly is repeated until sufficient height is achieved to allow the wings to deflect downward. The last section of the shaft is the top shaft section designed to hold the rotor in place using four notches. The disadvantage of this design is the numerous assembly steps to build the shaft sections (see Table 9). Perhaps a better design for the shaft would incorporate a single, tall silicon shaft

fabricated aside from MUMPs<sup>®</sup>. Unfortunately, the feasibility of this design was not tested because the flip bond machine at AFIT was newly purchased and without necessary parts, resources and training.

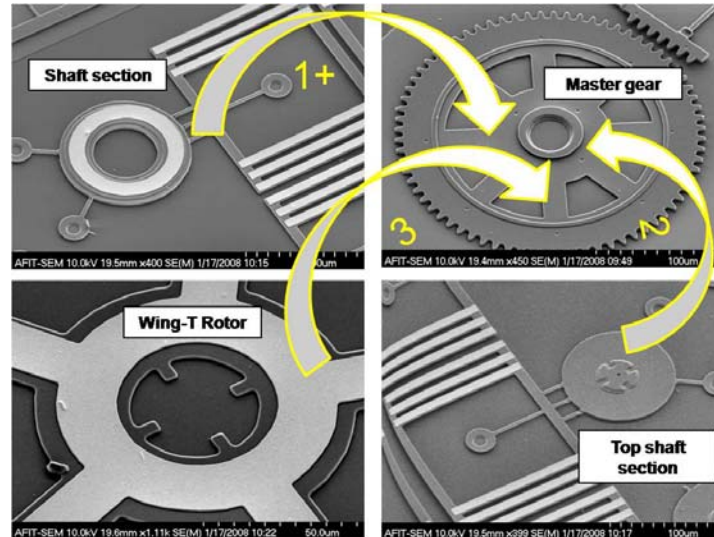


**Figure 93:** SEM pictures of the MEMS devices in order of assembly. The shaft ring (1) assembles around the hub of the master gear, and it is designed to repeat until sufficient height is achieved. The top of the shaft (2) holds the rotor (3) in place using the notch-lock design.

## 6.5 Chapter Summary

This chapter presented the experimental tests and results of creating a rotary-wing MEMS robot. The wing deflection of the leading edge and chord segment were measured with an IFM and compared to simulated and calculated data. The deflection of Wing-G was within 10% of simulated data and matched almost identically to calculated data up to 0.75 mm. The deflection of Wing-T was much lower than calculated and simulated data due to disconnected evaporated gold.

The orthogonal comb drive setup was moderately successful. The out-of-phase comb drives actually rotated the master gear without wings, but the frequency was not analyzed because the rotation was erratic. A nitride breach in the wiring created a capacitor between the shuttle and substrate on many of the designs as well. Also, the clutch arm often broke from the rack at high voltages and instantaneous changes in voltage.

The wings were capable of intermittent rotation using alternate orthogonal thermal actuators. The thermal actuators were designed as a backup drive source since 5 and 6-linked orthogonal comb drives were not fabricated. The actuators were capable of rotating the wings for small angles, but typically were stuck beneath the wings where the Poly2 covered the gear teeth. However, a 12 V, 20 Hz DC cycle demonstrated proof-of-concept rotation.

An attempt to manually create a 15-20° pitch angle with photoresist and Crystalbond™ was unsuccessful. The photoresist was deposited, but dissolved in the sacrificial oxide release due to the thin width of the hinge pattern or possible overexposure. Crystalbond™ adhered the wing parts together but did not increase deflection beyond that of residual stress. Chapter 7 summarizes the conclusions and recommendations for future rotary-wing MEMS robot research.

## **VII. Conclusions and Recommendations**

### **7.1 Chapter Overview**

This chapter presents the conclusions and recommendations culminating from this research effort. The conclusions of this research fall in four categories—wing deflection, wing hinge, orthogonal comb drive actuation and wing rotation. The significant findings and future direction of this research will also be discussed.

### **7.2 Conclusions of Research**

The deflection of the two wing designs were analyzed along the leading edge and chord segments. The wing deflection of each wing was calculated using two methods—one dependent of the radius of curvature and the other independent. The calculated data did not account for the large variable moment of inertia of both wings; so, analytical data predicted Wing-G to deflect the most due to its longer chord. However, the simulated results in CoventorWare<sup>®</sup> identified Wing-T to deflect more because its chord is smaller with less mass (less moment of inertia). The analytical and simulated data agree very closely for 0.5 mm or less. The empirical deflection of Wing-G was within 10% of the more realistic simulated data. The measured deflection of Wing-T was much less than simulated and calculated results due to the disconnected evaporated gold layer in the corrugation.

Two attempts were made to assemble the wing's chord at a 15-20° pitch angle. A single layer of 1818 photoresist was deposited and lithographically patterned for the hinge. However, the photoresist dissolved during the sacrificial oxide release. The width



of the resist hinge was too thin to adhere to the gold of the spar and chord, and the 1818 photoresist may have been overexposed. A second attempt using Crystalbond™ adhered to the gold but did not increase the deflection more than the small angle created by residual stress. Future research should consider solder spheres.

The orthogonal comb drive designs were moderately successful. The actuation scheme rotated a large gear as anticipated, but the rotation was irregular. The nitride layer of the MEMS chip was breached due to a design flaw in the wiring from the probe pad to the actuator. The nitride breach created a capacitor which attracted the comb drive shuttle to the underlying ground electrode. Also, the clutch arm attached to the rotating rack would often become broken due to high voltage and sudden spikes in voltage.

Multiple-linked orthogonal comb drives were identified as the best means for actuating the gear and wings. Theoretical expressions were derived to determine the number of comb drives required to rotate both wing designs. Calculations predicted at least four, and preferably six connected comb drives arranged orthogonally provided sufficient force to turn the wings at a rate that would generate sufficient lift. Multiple-linked comb drives were not demonstrated in this research since they would have taken up most of the chip space. However, orthogonally connected thermal actuators were fabricated as a backup to demonstrate wing rotation.

Wing rotation was demonstrated using thermal actuators. The actuators provided sufficient force when two 20 Hz, 12 V DC square waves were applied with an approximate 90° phase difference. Limited wing rotation was demonstrated with both rotor designs. A constant rotation was not successful because the Poly2 wing interfered



with the gear teeth below. The rotating rack would become caught in the Poly2 wing covering the master gear teeth. Controlling the wing rotation was difficult because the system required both a precise phase angle difference and DC offset. In particular, tuning the DC offset was challenging since the amplifier was an analog device. Perhaps a digital wideband amplifier would enhance the experimental results.

### 7.3 Significance of Research

The results of this research have identified important limitations and requirements of a rotary-wing MEMS robot. The following bullets are highlights resulting from this research effort:

- **Fabrication of a low-Reynolds number wing design.** A novel MEMS wing was designed and fabricated in this research (Wing-T) incorporating the significant findings of Tsuzuki, *et al* which is conducive for low-Reynolds number insect regime of flight. To the author's knowledge, this is the first attempt to fabricate a wing with insect features using solely MEMS technology.
- **Derived expressions for minimum actuator force and allowable robot mass.** The minimum force to turn a gear with attached rotary-wings was derived. The expression accounted for the unknown aerodynamic coefficient developed by Miki and the friction of MUMPs<sup>®</sup> dimples research by Lumbantobing. Similarly, an expression to define the maximum allowable mass available to a quad-rotor robot employing orthogonal comb drive

actuators was defined. These expressions are shown below again for reference.

$$F_{Net}(V) = JF_E(V) - K \left( \frac{(m_{gear} + m_{wings} + 2Jm_S)g}{A_C} \right)^{B-1} (m_{gear} + m_{wings} + 2Jm_S)g$$

$$m_{available}(V) = \frac{8\rho_{air}R^3bL_C C_{rw}}{3g} \left( \frac{N_{rack}(V)}{N_{gear}} \pi f_{comb} \right)^2 - 4(m_{gear} + bm_{wing} + Jm_S)$$

- **Derived expressions for average power consumption of a quad-rotor robot.**

The average sinusoidal power consumption for a rotary-wing MEMS robot was expressed in this research. The expression accounts for the electro-mechanical comb drive modeling of Yalcinkaya and the quality factor energy loss research of Schmidt. The expression is shown below for quick reference.

$$P_{robot} = \frac{V^2}{2} \left( \frac{\sqrt{k_S m^*}}{4YQ\eta_T^2} \right)^{-1}$$

- **Demonstrated proof-of-concept wing rotation.** The work of this research demonstrated limited wing rotation using orthogonal thermal actuators. In the same way, multiple-linked comb drives are capable of turning rotary wings. The concept of orthogonal comb drive actuators turning a gear without wings was demonstrated with limited success.

#### 7.4 Recommendations for Future Research

There still remains tremendous room for improvement to successfully develop a flying MEMS robot. For the MEMS robot to achieve lift is just half the battle;

configuring the robot to operate in a realistic environment full of threatening obstacles also requires precise sensors and CMOS circuitry. Figure 94 shows the vision of a future rotary-wing MEMS robot.

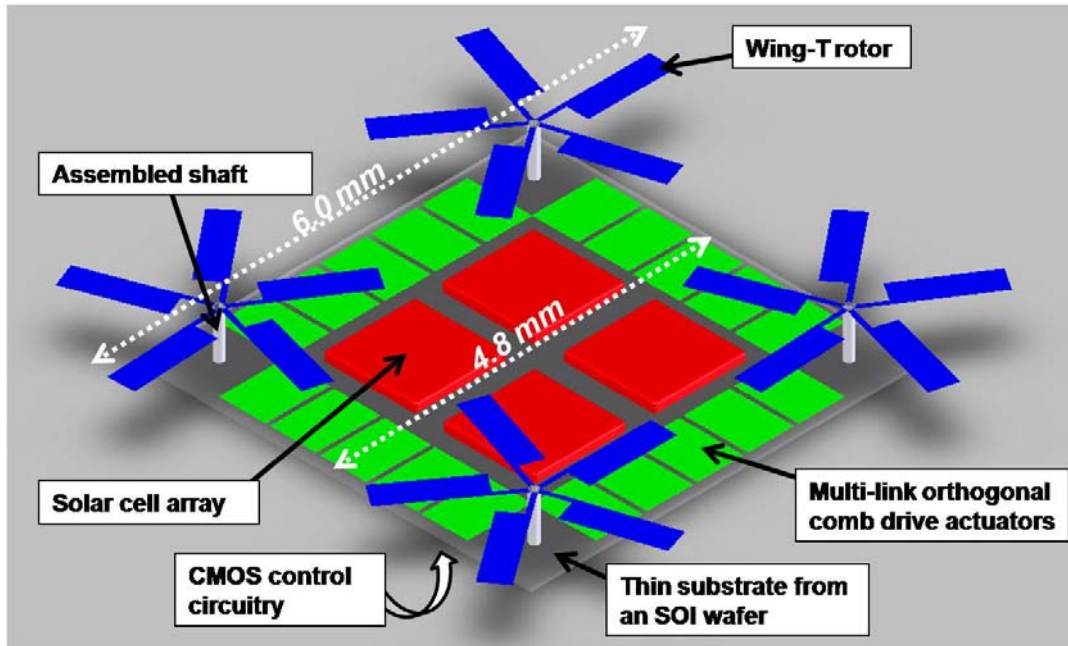


**Figure 94:** Vision of a quad-rotor robot employing multi-linked orthogonal comb drive actuators, biomimetic Wing-T rotors, power scavenging solar cells and CMOS control circuitry beneath the substrate. This model was created using SolidWorks™.

For the near future, PolyMUMPs™ is an excellent source for proof-of-concept devices; however, to fabricate the entire robot in this process is unfeasible. Other options such as Sandia's Sandia Ultra-planar Multi-level MEMS Technology V (SUMMiT V™) are capable of planar (versus conformal) deposition and include a third layer of structural polysilicon. An extra layer would increase the electrostatic force of the comb drive actuator, and the planar capabilities would fix the problem of the wings interfering with the underlying gear teeth. However, if improving upon this design in MUMPs®, it is imperative to include Poly0 for wire runs and make sure any meshing gear teeth have

enough overlap. Also, smaller corrugation in the Wing-T design could increase its deflection.

Flip bond technology is the next step in making this project a reality. The shaft could be etched in one piece of polysilicon via deep RIE (DRIE) and assembled to the gear and actuating system. Likewise, the wings could be fabricated on a separate wafer and assembled to the shaft. The easiest way to assemble separate devices is to utilize silicon-over-insulator (SOI) wafers. An SOI wafer is basically two silicon wafers combined with silicon dioxide in the middle. Releasing a SOI wafer in HF would yield two wafers, and the top wafer is as thin as 40-50  $\mu\text{m}$ . Devices can be completely etched in the top wafer via DRIE and assembled to the parent chip (also a SOI wafer)—similar to the process shown in Figure 48.

The capability of depositing polysilicon and nitride layers via LPCVD is an anticipated capability in AFIT's near future. Simple MEMS devices could have quick turnarounds rather than relying on the PolyMUMPs<sup>®</sup> schedule.

## **7.5 Summary**

This chapter summarized the results of this research effort, and future follow-on research should take the following guidance. Realize the PolyMUMPs<sup>™</sup> schedule is, unfortunately, arranged so that MEMS designs are due before the previous run is received. Therefore, any simple mistakes are likely to occur twice; have all designs peer reviewed. Also, it is in the best interest to explore other fabrication avenues such as those offered at AFRL/RVDD or Sandia Laboratory.

## Appendix A: L-Edit Mask Designs

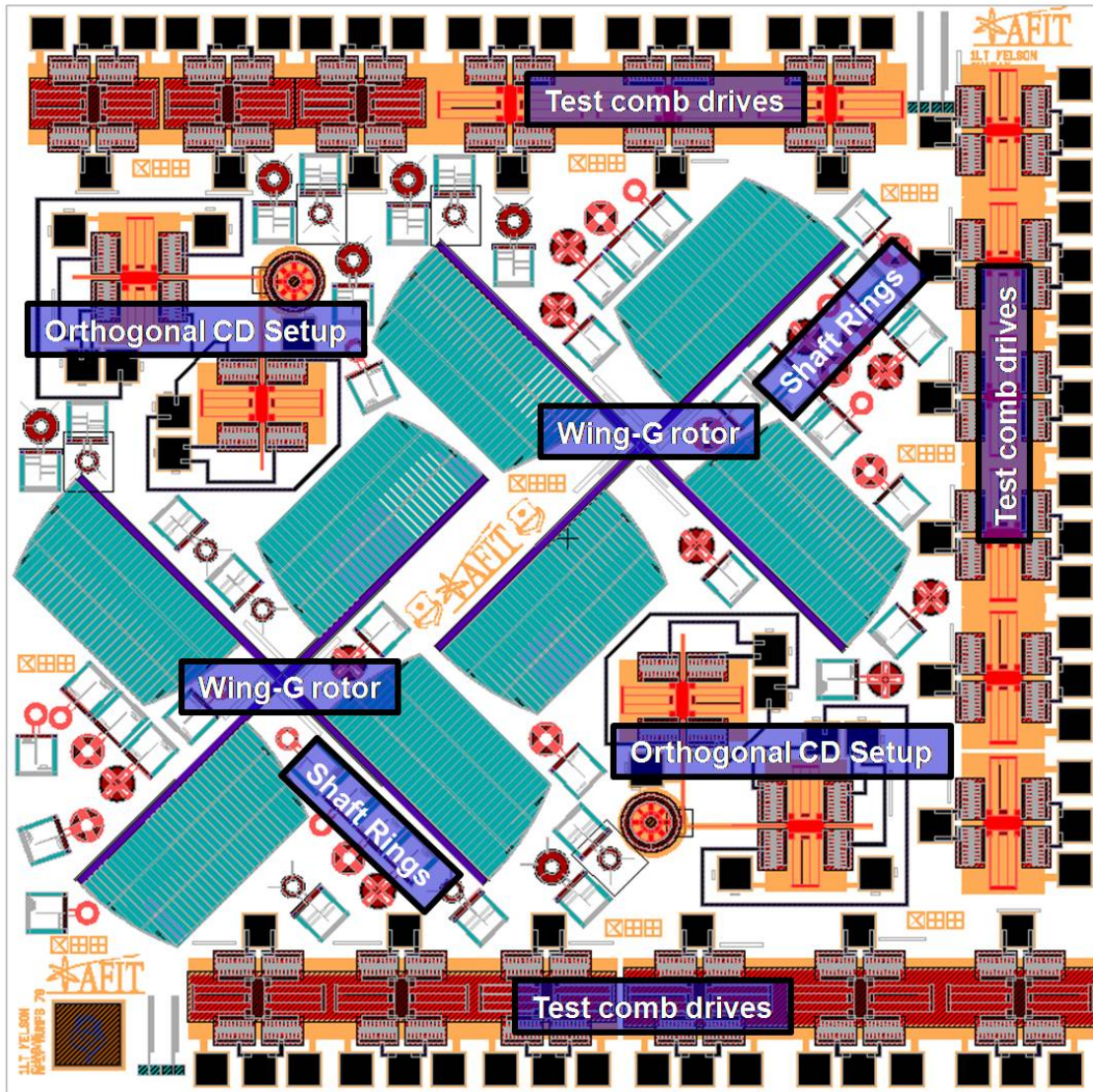


**Figure 95:** MUMPs® 78 L-Edit mask design with Wing-G rotors, shaft ring assembly parts, and individual and orthogonal comb drives for empirical data.

### Comments

<i>Wing-G Rotor</i>	The rotors consist of a Poly1 spar; later this was changed to Poly2 for ease of making a photoresist hinge.
<i>Orthogonal Comb Drive</i>	Designed to rotate a Poly1 gear with stacked polysilicon meshing teeth.
<i>Test Comb Drives</i>	Varied the flexure length and width.
<i>Shaft Rings</i>	Designed to build the shaft and hold the rotor using four notches.



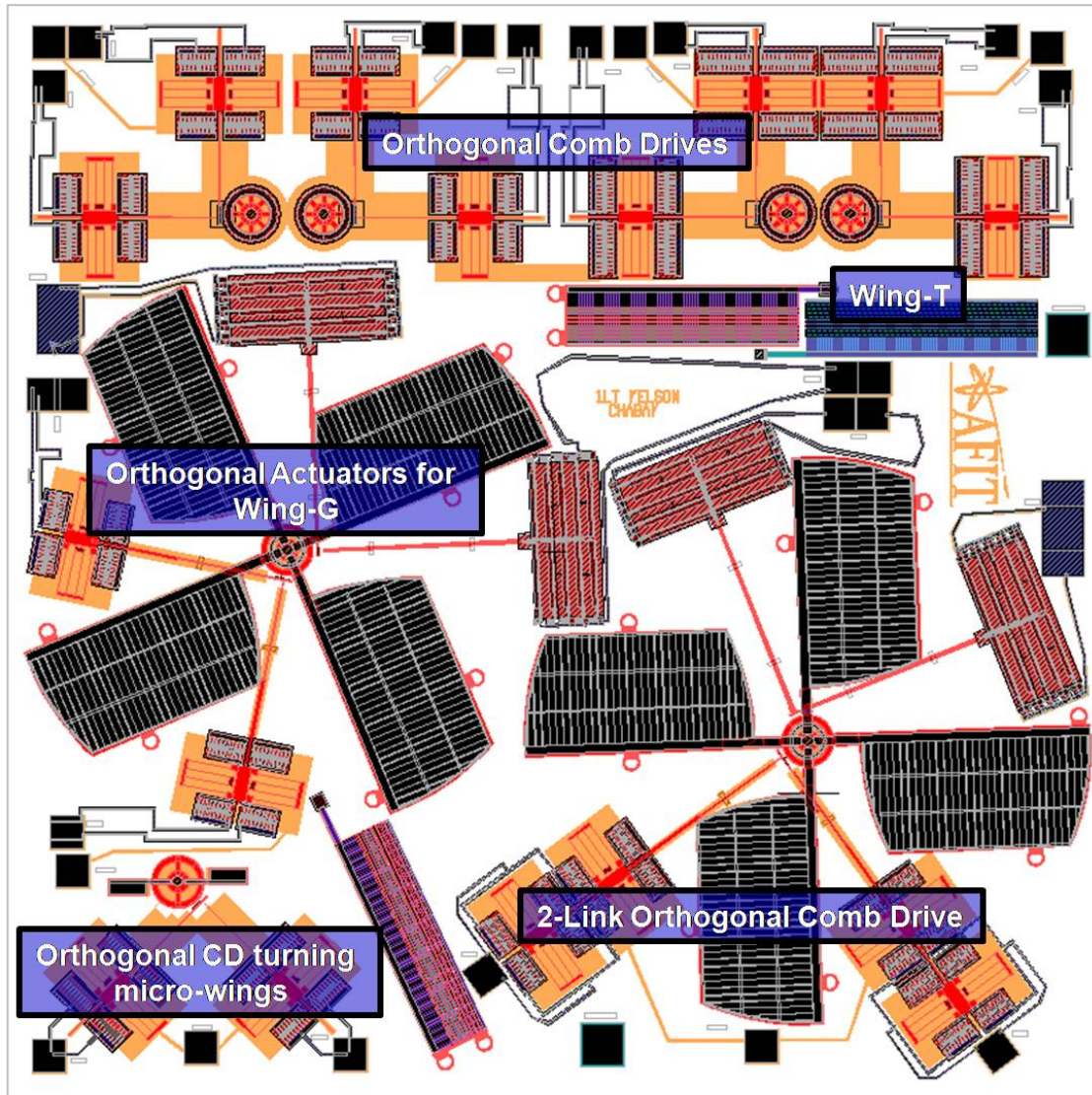


**Figure 96:** MUMPs<sup>®</sup> 79 Chip 1L-Edit mask design with orthogonal actuators, 2-Link orthogonal comb drive actuator, Wing-G rotors, and measurable Wing-T designs.

#### Comments

<i>Orthogonal Actuators for Wing-G</i>	Both orthogonal comb drive and thermal actuators were fabricated to turn the Wing-G rotor. The thermal actuators served as a “backup” to the comb drives which possessed too low of force.
<i>2-Link Orthogonal Comb Drive</i>	The design was created to observe two CDs resonating together although too little force was observed.
<i>Wing-T</i>	Designed to measure the deflection of the wing.
<i>Micro-Wings</i>	Proof-of-concept design to observe small wings turn. This design was faulty because the ground plane did not run under the rack.

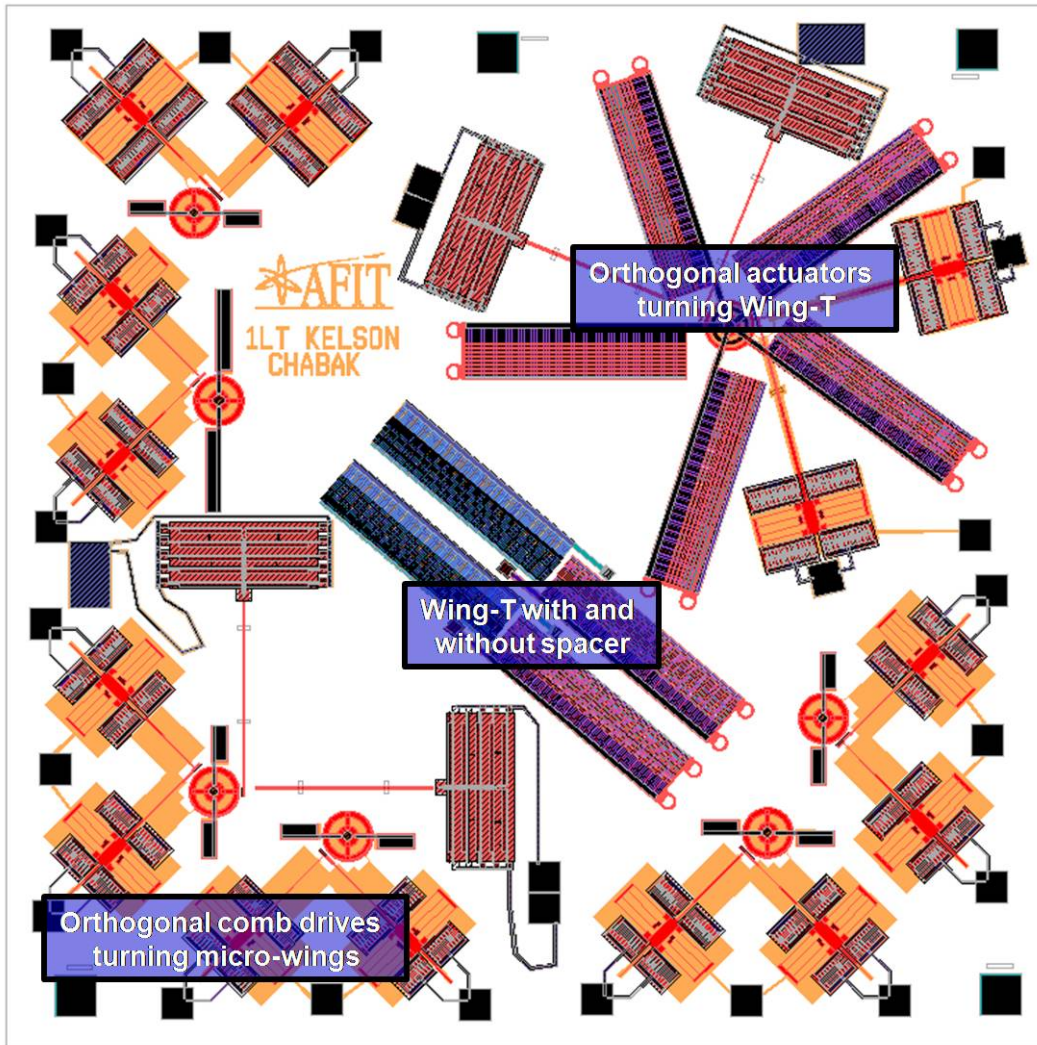


**Figure 97:** MUMPs® 79 Chip 2 L-Edit mask design with orthogonal actuators, Wing-T designs, and orthogonal comb drive micro-wings.

<b>Comments</b>	
<i>Orthogonal Comb Drives Micro-Wings</i>	These designs were created to show proof-of-concept wing rotation, but the ground plane was incorrectly designed. The ground should have run underneath the comb drive rack.
<i>Wing-T</i>	Designed to measure the deflection of the wing. The spacer had little effect except to raise the structure by the thickness of the spacer.
<i>Orthogonal Actuators for Wing-T</i>	The orthogonal comb drive did not have enough force to turn the Wing-T rotor. The orthogonal thermal actuators were designed as a backup.



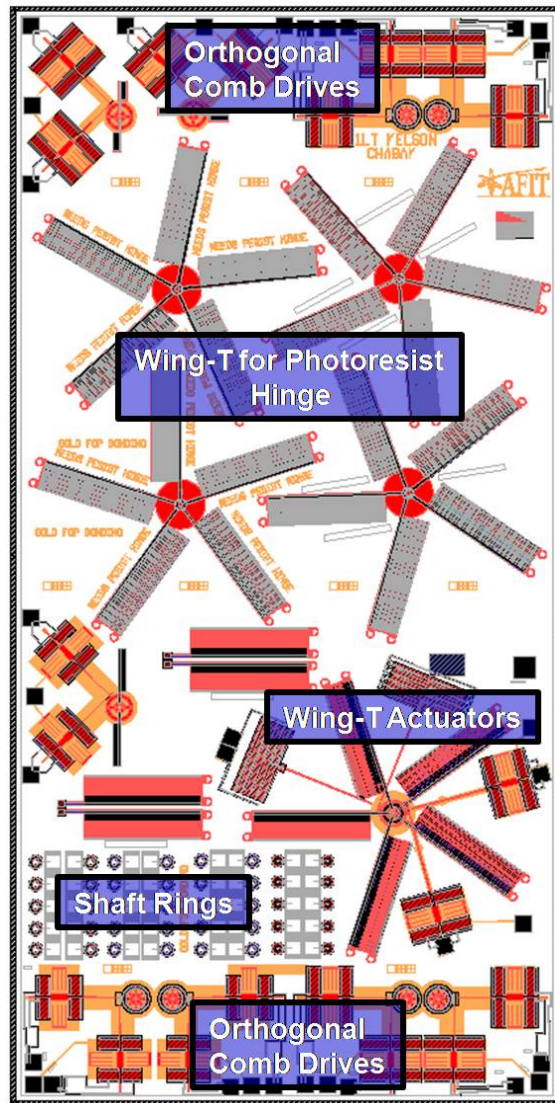


**Figure 98:** MUMPs<sup>®</sup> 80 L-Edit mask design with orthogonal actuators, Wing-T designs, and orthogonal comb drive micro-wings.

### Comments

<i>Wing-T Photoresist Hinge</i>	The photoresist hinge design simply separated the rib array from the spar in an attempt to deposit photoresist between them and create an upward deflection angle of 15-20°.
<i>Wing-T Actuators</i>	The orthogonal comb drive did not have enough force to turn the Wing-T rotor. The orthogonal thermal actuators were designed as a backup.
<i>Shaft Rings</i>	Designed to build the shaft and hold the rotor using four notches.



## Appendix B: Residual Stress Deflection Calculations

### Analytical 1 Deflection Calculations

<i>Step</i>	<i>Equation</i>	<i>Remarks</i>
<b>1</b>	$v_{bilayer} = \frac{\sigma_{bilayer} 3t_G L^2}{E_P t_P^2}$	Equation for bilayer cantilever deflection
<b>2</b>	$v_{bilayer} = \frac{\sigma_{bilayer} 3t_G L^2}{\left(\frac{E_P}{1-\nu_P}\right) t_P^2}$	Substituting in biaxial modulus of elasticity of polysilicon
<b>3</b>	$v_{bilayer} = \frac{(\sigma_{internal} + \sigma_{thermal}) 3t_G L^2}{\left(\frac{E_P}{1-\nu_P}\right) t_P^2}$	Separating bilayer residual stress into internal and thermal stress
<b>4</b>	$v_{bilayer} = \frac{(\sigma_{internal} + E'_G (\alpha_G - \alpha_P)(T - T_0)) 3t_G L^2}{\left(\frac{E_P}{1-\nu_P}\right) t_P^2}$	Substituting in equation for thermal stress
<b>5</b>	$v_{bilayer} = \frac{\left(\sigma_{internal} + \left(\frac{E_G}{1-\nu_G}\right) (\alpha_G - \alpha_P)(T - T_0)\right) 3t_G L^2}{\left(\frac{E_P}{1-\nu_P}\right) t_P^2}$	Substituting in biaxial modulus of elasticity of gold
<b>6</b>	$\sigma_{internal} = \sigma_P \frac{t_P}{t_P + t_G} + \sigma_G \frac{t_G}{t_P + t_G}$	Linear interpolation of total internal stress of Poly2 and Gold
<b>7</b>	$\begin{array}{lll} \sigma_P = -8MPa & E_P = 162GPa & T = 333K \\ \sigma_G = 13MPa & \nu_P = 0.22 & T_0 = 300K \\ t_P = 2\mu m & E_G = 78GPa & \alpha_G = 0.0000143 \frac{1}{K} \\ t_G = 0.5\mu m & \nu_G = 0.44 & \\ & L = 1.25mm & \alpha_P = 0.0000023 \frac{1}{K} \end{array}$	All the necessary variables to plug into Step 5

## Analytical 2 Deflection Calculations

Step	Equation	Remarks
1	$v_{bilayer} = \frac{\sigma_{bilayer} 3t_G L^2}{E_P t_P^2}$	Equation for bilayer cantilever deflection
2	$v_{bilayer} = \frac{\left( \frac{E_P t_P^2}{6t_G R_{bilayer}} \right) 3t_G L^2}{E_P t_P^2}$	Substituting Stoney's Equation for Bilayer Residual Stress
3	$v_{bilayer} = \frac{L^2}{2R_{bilayer}}$	Simplifying
4	$v_{bilayer} = \frac{L^2}{2 \left( \frac{E'_G (t_P + t_G)^2}{6t_P t_G \sigma_{thermal}} \right)}$	Substituting in radius of curvature for Poly2/Gold cantilever
5	$v_{bilayer} = \frac{L^2}{\frac{(t_P + t_G)^2}{3t_P t_G (\alpha_G - \alpha_P)(T - T_0)}}$	Substituting in thermal stress component and simplifying
6	$  \begin{array}{l}  t_P = 2\mu m \\  t_G = 0.5\mu m \\  T = 333K \\  T_0 = 300K \\  L = 1.25mm  \end{array}  \quad  \begin{array}{l}  \alpha_G = 0.0000143 \frac{1}{K} \\  \alpha_P = 0.0000023 \frac{1}{K}  \end{array}  $	All the necessary variables to plug into Step 5

## Appendix C: Comb Drive Actuator Calculations

### Comb Drive Force

<i>Step</i>	<i>Equation</i>	<i>Remarks</i>
<b>1</b>	$F_{comb} = \frac{dW_E}{dx}$	Equation for electrostatic force of one comb drive actuator
<b>2</b>	$F_{comb}(V) = \frac{d}{dx} n \left( x \frac{\epsilon_0 \epsilon_{air} t_P}{h} \right) V^2$	Substituting equation for electrical work
<b>3</b>	$F_{comb}(V) = n \left( \frac{\epsilon_0 \epsilon_{air} t_P}{h} \right) V^2$	Simplify
<b>4</b>	$n = 18 \quad t_F = 3.5 \mu m$ $\epsilon_0 = 8.85E(-14) \frac{F}{cm} \quad \epsilon_{air} = 1$ $h = 3 \mu m$	All the necessary variables to plug into Step 3

### Comb Drive Deflection

<i>Step</i>	<i>Equation</i>	<i>Remarks</i>
<b>1</b>	$d_{comb}(V) = \frac{F_{comb}(V)}{k_{flexure}}$	Hooke's Law
<b>2</b>	$d_{comb}(V) = \frac{n \frac{\epsilon_0 \epsilon_{air} t_P}{h} V^2}{\frac{24E_P I_Z}{L_S^3}}$	Substituting in comb drive force and spring constant of folded flexures
<b>3</b>	$d_{comb}(V) = \frac{n \frac{\epsilon_0 \epsilon_{air} t_P}{h} V^2}{\frac{24E_P \frac{w^3 t_{flex}}{12}}{L_S^3}}$	Substituting in the area moment of inertia about the z-axis perpendicular axis normal to the substrate
<b>4</b>	$n = 18 \quad t_F = 3.5 \mu m$ $\epsilon_0 = 8.85E(-14) \frac{F}{cm} \quad \epsilon_{air} = 1$ $w = 2.5 \mu m \quad h = 3 \mu m$ $t_{flex} = 2 \mu m \quad L_S = 250 \mu m$	All the necessary variables to plug into Step 3

## Appendix D: Photoresist Hinge Mask

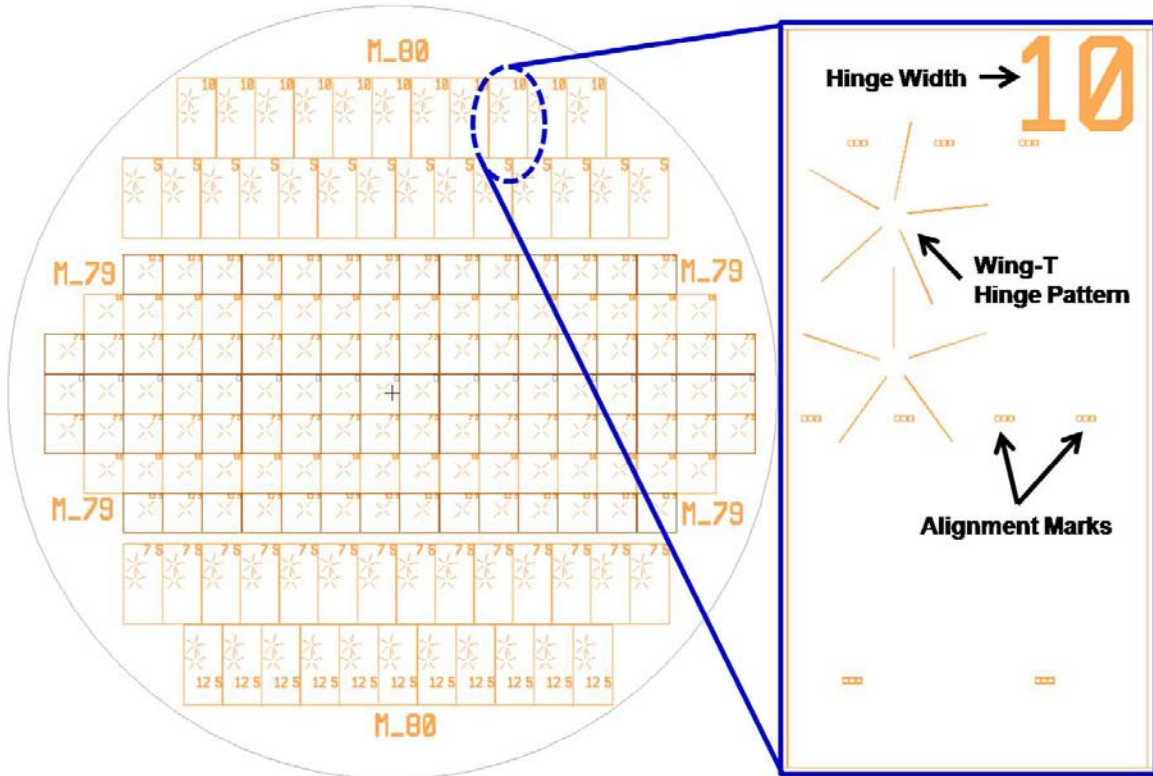


**Figure 99:** L-Edit drawing of the photoresist hinge mask. The mask consists of hinge patterns for Wing-G (MUMPs<sup>®</sup> 79) and Wing-T (MUMPs<sup>®</sup> 80). Shown to the right is a close-up of one of the Wing-T reticules. For each wing 5, 7.5, 10 and 12.5  $\mu\text{m}$  hinge width patterns were designed on the mask.

## Bibliography

- [1] T. R. Kurfess, *Robotics and automation handbook*. Boca Raton, Fla.: CRC Press, 2004.
- [2] U. Rembold and S. Fatikow, "Autonomous Microrobots," *Journal of Intelligent and Robotic Systems*, vol. 19, pp. 375-391, 1997.
- [3] R. P. Feynman, "There's plenty of room at the bottom [data storage]," *Microelectromechanical Systems, Journal of*, vol. 1, pp. 60-66, 1992.
- [4] J. S. Albus, "Robotics: Where has it been? Where is it going?," *Robotics and Autonomous Systems*, vol. 6, pp. 199-219, 1990.
- [5] S. Middelhock and S. A. Auder, *Silicon Sensors*. New York: Academic Press, 1989.
- [6] J. Fluitman, "Microsystems technology: objectives," *Sensors and Actuators A: Physical*, vol. 56, pp. 151-166, 1996.
- [7] T. Fukuda, K. Tanie, and T. Mituoka, "A New Method of Master-Slave Type of Teleoperation for a Micro-Manipulator System," in *Proceedings of Micro Robots and Teleoperators Workshop*, 1987.
- [8] K. Suzuki, I. Shimoyama, H. Miura, and Y. Ezura, "Creation of an insect-based microrobot with an external skeleton and elastic joints," 1992, pp. 190-195.
- [9] T. Fukuda, A. Kawamoto, F. Arai, and H. Matsuura, "Mechanism and swimming experiment of micro mobile robot in water," 1994, pp. 273-278.
- [10] H. Fujita, "A decade of MEMS and its future," in *Proceedings from the Tenth Annual International Workshop on Micro Electro Mechanical Systems.*, Tokyo, Japan, 1997, pp. 1-7.
- [11] I. Shimoyama, Y. Kubo, T. Kaneda, and H. Miura, "Simple microflight mechanism on silicon wafer," 1994, pp. 148-152.
- [12] I. Shimoyama, Y. K. Fujisawa, G. D. Getzan, H. Miura, M. Shimada, and Y. Matsumoto, "Fluid dynamics of microwing," in *Micro Electro Mechanical Systems, 1995, MEMS '95, Proceedings. IEEE*, 1995, p. 380.
- [13] R. O. Hundley and E. C. Gritton, "Future Technology-Driven Revolutions in Military Operations," RAND Corporation DARPA, 1994.
- [14] W. R. Davis, "Micro UAV," in *Presentation to 23rd AUVSI Symposium*, 15-19 July 1996.

- [15] M. T. Keennon and J. M. Grasmeyer, "Development of the Black Widow and Microbat MAVs and a Vision of the Future of MAV Design," in *AIAA/ICAS International Air and Space Symposium and Exposition: The Next 100 Y* Dayton, OH, 14-17 July 2003.
- [16] S. Hollar, A. Flynn, C. Bellew, and K. S. J. Pister, "Solar powered 10 mg silicon robot," 2003, pp. 706-711.
- [17] S. Hollar, A. Flynn, S. Bergbreiter, and K. S. J. Pister, "Robot Leg Motion in a Planarized-SOI, Two-Layer Poly-Si Process," *Microelectromechanical Systems, Journal of*, vol. 14, pp. 725-740, 2005.
- [18] B. Donald, C. Levey, C. McGray, I. Paprotny, and D. Rus, "An Untethered, Electrostatic, Globally Controllable MEMS Micro-Robot," *Journal of Microelectromechanical Systems*, vol. 15, pp. 1-15, 2006.
- [19] M. Brown, T. Hubbard, and M. Kujath, "Development of a long-range untethered frictional microcrawler," *Journal of Micromechanical Microengineering*, vol. 17, pp. 1025-1033, 2007.
- [20] D. Denninghoff, "Power Scavenging MEMS Robots," in *Department of Electrical and Computer Engineering Wright-Patterson AFB OH: Air Force Institute of Technology*, 2006.
- [21] T. Ebefors, J. U. Mattsson, E. Kalvesten, and G. Stemme, "A Robust Micro Conveyer Realized By Arrayed Polyimide Joint Actuators," *Journal of Micromechanical Microengineering*, vol. 10, pp. 337-349, 2000.
- [22] D. J. Pines and F. Bohorquez, "Challenges Facing Future Micro-Air-Vehicle Development," *Journal of Aircraft*, vol. 43, pp. 290-305, March-April 2006.
- [23] C. Roberts, M. Vaughan, and W. J. Bowman, "Development of a Solar Powered Micro Air Vehicle," in *40 Aerospace Sciences Meeting and Exhibit* Reno, Nevada, 14-17 January 2002.
- [24] "Micro Air Vehicle: Design to Reality," BAE Systems Informational & Electronic Warfare Systems.
- [25] J. Grasmeyer and M. Keennon, "Development of the Black Widow Micro Air Vehicle," *American Institute of Aeronautics and Astronautics*, vol. AIAA-2001-127, 2001.
- [26] W. Shyy, P. Ifju, and D. Viieru, "Membrane Wing-Based Micro Air Vehicles," *Applied Mechanics Reviews*, vol. 58, pp. 283-301, 07/00 2005.

- [27] P. G. Ifju, D. A. Jenkins, S. Ettinger, Y. Lian, and W. Shyy, "Flexible-Wing-Based Micro Air Vehicles," *American Institute of Aeronautics and Astronautics*, vol. AIAA 2002-0705, 2002.
- [28] <http://www.modelaircraft.org/Mag/PaulMcCready/DSCN231.jpg>, "Black Widow MAV."
- [29] T. N. Pornsin-Sirirak, Y.-C. Tai, C.-M. Ho, and M. Keennon, "Microbat: A Palm-Sized Electrically Powered Ornithopter," in *Proceedings of NASA/JPL Workshop on Biomimetic Robotics*, 2001.
- [30] T. N. Pornsin-Sirirak, S. W. Lee, H. Nassef, J. Grasmeyer, Y. C. Tai, C. M. Ho, and M. Keennon, "MEMS wing technology for a battery-powered ornithopter," pp. 799-804.
- [31] T. N. Pornsin-sirirak, Y. C. Tai, H. Nassef, and C. M. Ho, "Titanium-alloy MEMS wing technology for a micro aerial vehicle application," *Sensors and Actuators A: Physical*, vol. 89, pp. 95-103, 2001/3/20.
- [32] I. Kroo and F. Prinz, "The Mesicopter: A Meso-Scale Flight Vehicle," Stanford University 2000.
- [33] I. Kroo and P. Kunz, "Development of the Mesicopter: A Miniature Autonomous Rotorcraft," in *American Helicopter Society Vertical Lift Aircraft Design Conference* San Francisco, CA, 2000.
- [34] "<http://robotics.eecs.berkeley.edu/~ronf/MFI/index.html>," Micromechanical Flying Insect.
- [35] R. S. Fearing, K. H. Chiang, M. H. Dickinson, D. L. Pick, M. Sitti, and J. Yan, "Wing transmission for a micromechanical flying insect," in *Robotics and Automation, 2000. Proceedings. ICRA '00. IEEE International Conference on*, 2000, pp. 1509-1516 vol.2.
- [36] M. Sitti, D. Campolo, J. Yan, R. S. Fearing, T. Su, D. Taylor, and T. Sands, "Development of PZT and PZN-PT Based Unimorph Actuators for Micromechanical Flapping Mechanisms," in *IEEE Int. Conf. Robotics and Automation*, Seoul Korea, May 21-26, 2001, pp. 3839-3846.
- [37] R. J. Wood, S. Avadhanula, and R. S. Fearing, "Microrobotics using Composite Materials: the Micromechanical Flying Insect Thorax," in *IEEE Int. Conf. on Robotics and Automation*, Taipei, Taiwan, 2003, pp. 1842-1849.
- [38] "DelFly II Specifications," in [www.delfly.nl/index.php?site=DII&menu=info=en](http://www.delfly.nl/index.php?site=DII&menu=info=en), 2007.
- [39] "DelFly Micro," in [www.delfly.nl/index.php?site=DIII&menu=&lang=en](http://www.delfly.nl/index.php?site=DIII&menu=&lang=en), 2007.

- [40] R. J. Wood, S. Avadhanula, E. Steltz, M. Seerman, J. Entwistle, A. Bachrach, G. Barrows, S. Sanders, and R. S. Fearing, "An Autonomous Palm-Sized Gliding Micro Air Vehicle," *IEEE Robotics and Automation Magazine*, pp. 82-92, 2007.
- [41] Y. Lung-Jieh, H. Cheng Kuei, H. Jen-Yang, W. Hsin-Hsiung, and F. Gwo-Hwa, "The micro aerial vehicle (MAV) with flapping wings," pp. 811-815.
- [42] Y. Kubo, I. Shimoyama, and H. Miura, "Study of insect-based flying microrobots," 1993, pp. 386-391 vol.2.
- [43] Y. Kubo, I. Shinoyama, T. Kaneda, and H. Miura, "Study on wings of flying microrobots," in *Robotics and Automation, 1994. Proceedings., 1994 IEEE International Conference on*, 1994, pp. 834-839 vol.1.
- [44] H.-Y. Chan, J. H. M. Lam, and W. J. Li, "A Biomimetic Flying Silicon Microchip: Feasibility Study," in *Proceedings of the 2004 IEEE International Conference on Robotics and Biomimetics*, Shenyang, China, August 22-26, 2004.
- [45] N. Miki and I. Shimoyama, "Analysis of the flight performance of small magnetic rotating wings for use in microrobots," in *Robotics and Automation, 1998. Proceedings. 1998 IEEE International Conference on*, 1998, pp. 3065-3070 vol.4.
- [46] N. Miki and I. Shimoyama, "Magnetic rotational micro-wings applicable to microrobots," in *Intelligent Robots and Systems, 1999. IROS '99. Proceedings. 1999 IEEE/RSJ International Conference on*, 1999, pp. 721-726 vol.2.
- [47] N. Miki and I. Shimoyama, "A Micro-Flight Mechanism with Rotational Wings," in *The 13th Annual International Conference on Micro-Electro-Mechanical Systems (MEMS)*, 2000, pp. 158-163.
- [48] N. Miki and I. Shimoyama, "Dynamics of a microflight mechanism with magnetic rotational wings in an alternating magnetic field," *Microelectromechanical Systems, Journal of*, vol. 11, pp. 584-591, 2002.
- [49] N. Miki and I. Shimoyama, "Soft-magnetic rotational microwings in an alternating magnetic field applicable to microflight mechanisms," *Microelectromechanical Systems, Journal of*, vol. 12, pp. 221-227, 2003.
- [50] N. Glauvitz, "Towards A Flying MEMS Robot," in *Department of Electrical and Computer Engineering Wright-Patterson AFB OH: Air Force Institute of Technology*, 2007.
- [51] A. H. Epstein, S. D. Senturia, and G. Anathasuresh, in *Proceedings of the Ninth International Conference on Solid-State Sensors and Actuators*, Chicago, IL, 1997.
- [52] A. C. Fernandez-Pello, in *Proc. Combustion Institution*, 2002, pp. 883-898.



- [53] L. Sitzki, K. Borer, E. Schuster, and P. D. Ronney, in *Proceedings of the Third Asia-Pacific Conference on Combustion*, Seoul, Korea, 2001.
- [54] L. C. Chia and B. Feng, "The Development of a Micropower (Micro-thermophotovoltaic) Device," *Journal of Power Sources*, vol. 165, pp. 455-480, 2007.
- [55] J. D. Morse, "Micro-fuel Cell Power Sources," *International Journal of Energy Research*, vol. 31, pp. 576-602, 2007.
- [56] S. J. Lee, A. Chang-Chien, S. W. Cha, R. O'Hayre, Y. I. Park, Y. Saito, and F. B. Prinz, "Design and Fabrication of a Micro Fuel Cell Array with "Flip-Flop" Interconnection," *Journal of Power Sources*, vol. 112, pp. 410-418, 2002.
- [57] J. Yu, P. Cheng, Z. Ma, and B. Yi, "Fabrication of Miniature Silicon Wafer Fuel Cells With Improved Performance," *Journal of Power Sources*, vol. 124, pp. 40-46, 2003.
- [58] D. M. C. Chapin, C. S. Fuller, and G. L. Pearson, *Journal of Applied Physics*, vol. 25, p. 676, 1954.
- [59] T. Sakakibara, "High-Voltage Photovoltaic Micro-Devices Fabricated By a New Laser-Processing," *IEEE Proceedings of 1995 Conference on Micro Electro Mechanical Systems*, pp. 282-287, 1995.
- [60] R. R. King, D. C. Law, K. M. Edmondson, C. M. Fetzer, G. S. Kinsey, and H. Yoon, "40% Efficient Metamorphic GaInP/GaInAs/Ge Multijunction Solar Cells," *Applied Physics Letters*, vol. 90, 2007.
- [61] N. Miyashita, "Fabrication of GaInNAs-based Solar Cells for Application to Multi-junction Tandem Solar Cells," *IEEE Transaction Letters*, pp. 869-772, 2006.
- [62] J. F. G. *e. al*, "High-Efficiency GaInP/GaAs/InGaAs Triple-Junction Solar Cells Grown Inverted with a Metamorphic Bottom Junction," *Applied Physics Letters*, vol. 91, 2007.
- [63] W. M. Yang, S. K. Chou, C. Shu, H. Xue, and Z. W. Li, *Journal of Applied Physics*, vol. 37, pp. 1017-1020, 2004.
- [64] "Lift Force," in [http://en.wikipedia.org/wiki/Lift\\_%28force%29](http://en.wikipedia.org/wiki/Lift_%28force%29).
- [65] T. J. Mueller, "Aerodynamic Measurements at Low Reynolds Numbers for Fixed Wing Micro-Air Vehicles," Hessert Center for Aerospace Research, University of Notre Dame, 1999.

- [66] S. Ho, H. Nassef, N. Pornsinsirirak, Y.-C. Tai, and C.-M. Ho, "Unsteady aerodynamics and flow control for flapping wing flyers," *Progress in Aerospace Sciences*, vol. 39, pp. 635-681, 11 2003.
- [67] H. Liu and K. A. Kawachi, "Numerical Study of Insect Flight," *Journal of Computational Physics*, vol. 146, pp. 124-156, 1998.
- [68] S. Ho, H. Nassef, N. Pornsin-Sirirak, Y.-C. Tai, and C.-M. Ho, "Flight Dynamics of Small Vehicles," in *International Council of Aeronautical Sciences Toronto*, Canada, 2002.
- [69] N. Tsuzuki, S. Sato, and T. Abe, "Design Guidelines of Rotary Wings in Hover for Insect-Scale Micro Air Vehicle Applications," *Journal of Aircraft*, vol. 44, pp. 252-263, 2007.
- [70] K. A. Kawachi, "Flight Mechanism of Insect (From Standpoint of View of Bio-Fluid-Dynamics)," *Biophysics*, vol. 39, pp. 279-284, 1999.
- [71] A. Azuma, "The Biokinetics of Flying and Swimming," Berlin: Springer-Verlag, 1992, pp. 65-75.
- [72] K. P. Dial, "An Inside Look at How Birds Fly: Experimental Studies of the Internal and External Processes Controlling Flight " in *38th Report the Aerospace Profession Symposium Proceedings*, The Beverly Hilton, Beverly Hills, CA, 1994.
- [73] S. Sunada, A. Ohkura, and K. A. Kawachi, "Characteristics of Rotary Wings in Hovering Mode at an Ultra-Low Reynolds Number," *Transactions of the Japan Society for Aeronautical and Space Sciences*, vol. 47, pp. 59-64, 2004.
- [74] J. R. Usherwood and C. P. Ellington, "The Aerodynamics fo Revolving Wings 1: Model Hawkmoth Wings," *Journal of Experimental Biology*, vol. 205, pp. 1547-1564, 2002.
- [75] C. J. C. Reese, "Form and Function in Corrugated Insect Wings," *Nature*, vol. 256, pp. 200-203, 1975.
- [76] J. M. Wakeling and C. P. Ellington, "Dragonfly Flight 3: Lift and Power Requirements " *Journal of Experimental Biology*, vol. 200, pp. 583-600, 1997.
- [77] L. A. Starman, "MEMS Fabrication Part 1 and 2," in *Class Notes: Wright State University*, 2006.
- [78] J. Carter, A. Cowen, B. Hardy, R. Mahadevan, M. Stonefield, and S. Wilcenski, *PolyMUMPs Design Handbook: MEMSCAP Inc.*, 2005.
- [79] Gold, "<http://en.wikipedia.org/wiki/Gold>."

- [80] R. W. Johnstone and M. Parameswaran, "Modeling Surface-Micromachined Electrothermal Actuators," *Canadian Journal of Electrical & Computer Engineering*, vol. 29, 2004.
- [81] E. A. M. Siakavellas, G. Kaltsas, and A. G. Nassiopoulos, "Micro-Raman Characterization of Stress Distribution within Free Standing Mono- and Polycrystalline Silicon Membranes," *Microelectronic Engineering*, vol. 41, pp. 469-472.
- [82] C. S. Lee, J. H. Lee, C. A. Choi, K. No, and D. M. Wee, "Effects of Phosphorus on Stress of Multi-Stacked Polysilicon Film and Single Crystalline Silicon," *Journal of Micromechanical Microengineering*, vol. 9, pp. 252-263, 1999.
- [83] D. Maier-Schneider, A. Köprülü, S. B. Holm, and E. Obermeier, "Elastic Properties and Microstructure of LPCVD Polysilicon Films," *Journal of Micromechanical Microengineering*, vol. 6, pp. 436-446, 1996.
- [84] L. A. Starman, "Characterization of Residual Stress in MEMS Devices Using Raman Spectroscopy," in *Department of Electrical and Computer Engineering WPAFB: Air Force Institute of Technology*, 2002, p. 269.
- [85] D. J. Bell, T. J. Lu, N. A. Fleck, and S. M. Spearing, "MEMS Actuators and Sensors: Observations On Their Performance and Selection For Purpose," *Journal of Micromechanics and Microengineering*, vol. 15, pp. 153-164, 2005.
- [86] R. Hickey, D. Sameoto, T. Hubbard, and M. Kujath, "Time and Frequency Response of Two-Arm Micromachined Thermal Actuators," *Journal of Micromechanics and Microengineering*, vol. 13, pp. 40-46, 2003.
- [87] S. M. Spearing, "Materials Issues in MEMS," *Acta Mater*, vol. 48, pp. 179-196, 2000.
- [88] W. C. Tang, T. C. H. Nguyen, and R. T. Howe, "Laterally driven polysilicon resonant microstructures," in *Micro Electro Mechanical Systems, 1989, Proceedings, 'An Investigation of Micro Structures, Sensors, Actuators, Machines and Robots'. IEEE*, 1989, pp. 53-59.
- [89] A. Lumbantobing and K. Komvopoulos, "Static Friction in Polysilicon Surface Micromachines," *Microelectromechanical Systems, Journal of*, vol. 14, pp. 651-663, 2005.
- [90] A. D. Yalcinkaya, "Micromechanical Resonators for Low-Power, Low-Voltage Systems," in *Microelectronics Center Lyngby: Technical University of Denmark*, 2003, p. 130.

- [91] M. A. Schmidt, R. T. Howe, S. D. Senturia, and J. H. Haritondis, "Design and Calibration of a Microfabricated Floating-Element Shear-Stress Sensor," *IEEE Transactions on Electron Devices*, vol. 35, pp. 750-757, 1988.
- [92] "PolyMUMPs Run Data," in [http://www.memscap.com/en\\_mumps.html](http://www.memscap.com/en_mumps.html).
- [93] R. J. Linderman, P. E. Kladitis, and V. M. Bright, "Development of the micro rotary fan," *Sensors and Actuators A: Physical*, vol. 95, pp. 135-142, 2002/1/1.

## Vita

Kelson D. Chabak was born in Dubuque, IA. After his father left the United States Coast Guard, he and his family were relocated to Decatur, IL where he was raised with his brother. Kelson attended Dwight D. Eisenhower of Decatur, IL, and graduated with honors in the class of 1999. Shortly thereafter, he enrolled as a freshman at the University of Southern Illinois-Edwardsville (SIUE) on an Illinois State AFROTC Scholarship. After completing one year at SIUE, he applied and was awarded a 4-year AFROTC Federal Scholarship.

The scholarship allowed him to transfer to Saint Louis University (SLU) in 2000 as a mechanical engineering student. While at SLU, he was active in Arnold Air Society, Beta Theta Pi fraternity and AFROTC Detachment 207. The fall semester of 2002 Kelson served as the Cadet Vice Wing Commander of the detachment. In 2004, he graduated magna cum laude with a Bachelor of Science Degree in Mechanical Engineering and as an AFROTC distinguished graduate.

Following graduation Kelson moved to Edwards AFB, California to work as a flight test engineer for the 412th Flight Test Squadron, Speckled Trout. His wife joined him after their marriage in 2005. He and his wife relocated to Dayton, OH after Kelson accepted an assignment to the Air Force Institute of Technology as a Master's student in Electrical Engineering in 2006. Kelson concentrated his studies in Micro-Electro-Mechanical Systems and Microelectronics. He will be assigned to the Air Force Research Laboratory-Sensors Directorate as a research engineer following graduation.

<b>REPORT DOCUMENTATION PAGE</b>				<i>Form Approved OMB No. 074-0188</i>	
<p>The public reporting burden for this collection of information is estimated to average 1 hour per response, including the time for reviewing instructions, searching existing data sources, gathering and maintaining the data needed, and completing and reviewing the collection of information. Send comments regarding this burden estimate or any other aspect of the collection of information, including suggestions for reducing this burden to Department of Defense, Washington Headquarters Services, Directorate for Information Operations and Reports (0704-0188), 1215 Jefferson Davis Highway, Suite 1204, Arlington, VA 22202-4302. Respondents should be aware that notwithstanding any other provision of law, no person shall be subject to a penalty for failing to comply with a collection of information if it does not display a currently valid OMB control number.</p> <p><b>PLEASE DO NOT RETURN YOUR FORM TO THE ABOVE ADDRESS.</b></p>					
<b>1. REPORT DATE (DD-MM-YYYY)</b> 27-03-2008		<b>2. REPORT TYPE</b> Master's Thesis		<b>3. DATES COVERED (From - To)</b> Jun 2006 - March 2008	
<b>4. TITLE AND SUBTITLE</b>  CONCEPTUAL STUDY OF ROTARY-WING MICROROBOTICS				<b>5a. CONTRACT NUMBER</b>	
				<b>5b. GRANT NUMBER</b>	
				<b>5c. PROGRAM ELEMENT NUMBER</b>	
<b>6. AUTHOR(S)</b>  Chabak, Kelson, D., First Lieutenant, USAF				<b>5d. PROJECT NUMBER</b> ENG 07-141	
				<b>5e. TASK NUMBER</b>	
				<b>5f. WORK UNIT NUMBER</b>	
<b>7. PERFORMING ORGANIZATION NAMES(S) AND ADDRESS(S)</b> Air Force Institute of Technology Graduate School of Engineering and Management (AFIT/EN) 2950 Hobson Way, Building 640 WPAFB OH 45433-8865				<b>8. PERFORMING ORGANIZATION REPORT NUMBER</b>  AFIT/GE/ENG/08-03	
<b>9. SPONSORING/MONITORING AGENCY NAME(S) AND ADDRESS(ES)</b> AFRL/RWAV AFMC Attn: Mr. Roger M. Smith, Chief of Micro-Munitions Team 101 West Eglin Blvd Eglin AFB, FL 32536 DSN: 872-4651 (roger.smith@eglin.af.mil)				<b>10. SPONSOR/MONITOR'S ACRONYM(S)</b>	
				<b>11. SPONSOR/MONITOR'S REPORT NUMBER(S)</b>	
<b>12. DISTRIBUTION/AVAILABILITY STATEMENT</b>  APPROVED FOR PUBLIC RELEASE; DISTRIBUTION UNLIMITED.					
<b>13. SUPPLEMENTARY NOTES</b>					
<b>14. ABSTRACT</b> This thesis presents a novel rotary-wing micro-electro-mechanical systems (MEMS) robot design. Two MEMS wing designs were designed, fabricated and tested including one that possesses features conducive to insect level aerodynamics. Two methods for fabricating an angled wing were also attempted with photoresist and CrystalBond™ to create an angle of attack. One particular design consisted of the wing designs mounted on a gear which are driven by MEMS actuators. MEMS comb drive actuators were analyzed, simulated and tested as a feasible drive system. The comb drive resonators were also designed orthogonally which successfully rotated a gear without wings. With wings attached to the gear, orthogonal MEMS thermal actuators demonstrated wing rotation with limited success. Multi-disciplinary theoretical expressions were formulated to account for necessary mechanical force, allowable mass for lift, and electrical power requirements. The robot design did not achieve flight, but the small pieces presented in this research with minor modifications are promising for a potential complete robot design under 1 cm <sup>2</sup> wingspan. The complete robot design would work best in a symmetrical quad-rotor configuration for simpler maneuverability and control. The military's method to gather surveillance, reconnaissance and intelligence could be transformed given a MEMS rotary-wing robot's diminutive size and multi-role capabilities.					
<b>15. SUBJECT TERMS</b> Micro-electro-mechanical systems, MEMS, low-Reynolds number, comb drive actuator, thermal actuator, microrobot, rotary-wing robot, MEMS wings					
<b>16. SECURITY CLASSIFICATION OF:</b>			<b>17. LIMITATION OF ABSTRACT</b>  UU	<b>18. NUMBER OF PAGES</b>  169	<b>19a. NAME OF RESPONSIBLE PERSON</b> LaVern Starman, Maj, USAF (ENG)
<b>a. REPO RT</b>  U	<b>b. ABSTRA CT</b>  U	<b>c. THIS PAGE</b>  U			<b>19b. TELEPHONE NUMBER (Include area code)</b> (937) 255-3636, ext 4618 (LaVern.Starman@afit.edu)

